

Vom Fachbereich VI Raum- und Umweltwissenschaften der Universität Trier zur Verleihung
des akademischen Grades 'Doktor der Naturwissenschaften' (Dr. rer. nat.) genehmigte
Dissertation:

Regional climate simulations in the Weddell Sea region (Antarctic): Model verification and evaluation of low-level jets

Autor: **Rolf Zentek**

Betreuer: Univ.-Prof. Dr. Günther Heinemann
Berichterstattende: Univ.-Prof. Dr. Günther Heinemann
Univ.-Prof. Dr. Thomas Udelhoven
Dr. Tido Semmler

Datum der wissenschaftlichen Aussprache: 13.07.2023

Trier, 2023

Contents

Abstract	3
List of Abbreviations	4
Preface	5
1 Introduction	6
1.1 Weddell Sea region	8
1.2 Antarctic observations	10
1.3 Regional climate simulations of Antarctica	11
1.4 Regional climate model CCLM	12
1.5 General outline of the thesis	13
2 Publications	16
2.1 Publication 1	16
2.1.1 Doppler wind lidar	16
2.1.2 Adaptations for ship-born measurements	17
2.2 Publication 2	20
2.2.1 Adaptations of CCLM for polar regions	20
2.2.2 Performed verification	21
2.3 Publication 3	22
2.3.1 Low level jet	23
2.3.2 Low level jet climatology	24
3 Outlook	26
4 Appended publications	28
4.1 Authors contributions	28
4.2 Publication 1	28
4.3 Publication 2	44
4.4 Publication 3	62
Acknowledgements	83
Bibliography	94
Curriculum Vitae	95

Abstract

This cumulative thesis encompasses three studies focusing on the Weddell Sea region in the Antarctic. The first study produces and evaluates a high quality data set of wind measurements for this region. The second study produces and evaluates a 15 year regional climate simulation for the Weddell Sea region. And the third study produces and evaluates a climatology of low level jets (LLJs) from the simulation data set. The evaluations were done in the attached three publications and the produced data sets are published online.

In 2015/2016, the RV Polarstern undertook an Antarctic expedition in the Weddell Sea. We operated a Doppler wind lidar on board during that time running different scan patterns. The resulting data was evaluated, corrected, processed and we derived horizontal wind speed and directions for vertical profiles with up to 2 km height. The measurements cover 38 days with a temporal resolution of 10-15 minutes. A comparison with other radio sounding data showed only minor differences.

The resulting data set was used alongside other measurements to evaluate temperature and wind of simulation data. The simulation data was produced with the regional climate model CCLM for the period of 2002 to 2016 for the Weddell Sea region. Only smaller biases were found except for a strong warm bias during winter near the surface of the Antarctic Plateau. Thus we adapted the model setup and were able to remove the bias in a second simulation.

This new simulation data was then used to derive a climatology of low level jets (LLJs). Statistics of occurrence frequency, height and wind speed of LLJs for the Weddell Sea region are presented along other parameters. Another evaluation with measurements was also performed in the last study.

List of Abbreviations

ABL	Atmospheric Boundary Layer
ACC	Antarctic Circumpolar Current
AMSR-E	Advanced Microwave Scanning Radiometer – for Earth observing system
AMSR2	Advanced Microwave Scanning Radiometer 2
AWS	Automatic Weather Station
CCLM	COSMO-CLM
CORDEX	COordinated Regional Climate Downscaling EXperiment
COSMO	COnsortium for Small-Scale MOdeling
COSMO-CLM	COSMO model in CLimate Mode (CLM)
DKRZ	Deutsches KlimaRechenZentrum
DWD	Deutscher WetterDienst
ECMWF	European Centre for Medium-range Weather Forecasts
ERA5	ECMWF ReAnalysis 5th generation
GCM	Global Climate Model
ICON	ICOsahedral Non-hydrostatic
LBC	Lateral Boundary Conditions
LIDAR	Llght Detection And Ranging
LLJ	Low Level Jet
MAR	Modèle Atmosphérique Régional
MOSAiC	Multidisciplinary drifting Observatory for the Study of Arctic Climate
MetUM	Met Office Unified Model
Polar-WRF	Polar Weather Research and Forecasting Model
PPP	Polar Prediction Project
RACMO	Regional Atmospheric Climate MOdel
RADAR	RAdio Detection And Ranging
RCM	Regional Climate Model
SAM	Southern Annular Mode
SBL	Stable Boundary Layer
SMB	Surface Mass Balance
SNR	Signal to Noise Ratio
SOP	Special Observing Period
SSMIS	Special Sensor Microwave Imager/Sounder
VAD	Velocity-Azimuth Display
WMO	World Meteorological Organisation
YOPP	Year Of Polar Prediction

Preface

Antarctic research has relatively short history. The seclusion of the Antarctic continent combined with extreme cold temperatures always presented a danger to expeditions, and the sea ice surrounding Antarctica is an obstacle for ships even to this day. With the beginning of the 20th century, several expeditions marked the start of exploration of the "unknown" continent. In 1911, Roald Amundsen and Robert Falcon Scott both started separate expeditions to the South Pole. This was the first time humans reached the South Pole, but Scott and his team did not make it back and died on the ice. In 1914, Ernest Shackleton started on an expedition to be the first to cross the Antarctic continent, but their ship got stuck and frozen in sea ice. After several month, the ship was eventually crushed by the sea ice and sank, but Shackleton and his team survived and in 1916, the last of them were rescued. [Alexander, 2007]

Today, the Amundsen-Scott station at the South Pole accommodates 50 to 150 scientists and support personnel all year long and modern icebreaker ships have much easier time getting through sea ice. Together with the use of air plains, satellites and computers, now at the beginning of the 21th century, Antarctic research looks a lot different.

1 Introduction

In the following, a short summary of key aspects about Antarctica is given. Almost the whole continent is south of the Antarctic Circle ($66^{\circ}34'S$). That means at least one day per year, the sun is never above the horizon. Another aspect is the sea ice surrounding Antarctica. It is about up to 1-2 m thick [Worby et al., 2008, Kurtz and Markus, 2012] and has a seasonal cycle with lowest area ($2 \times 10^6 \text{ km}^2$) in February and highest area ($15 \times 10^6 \text{ km}^2$) in September [Parkinson and Cavalieri, 2012] which equals approximately the inland area ($14 \times 10^6 \text{ km}^2$). An overview is shown in Fig. 1.1a.

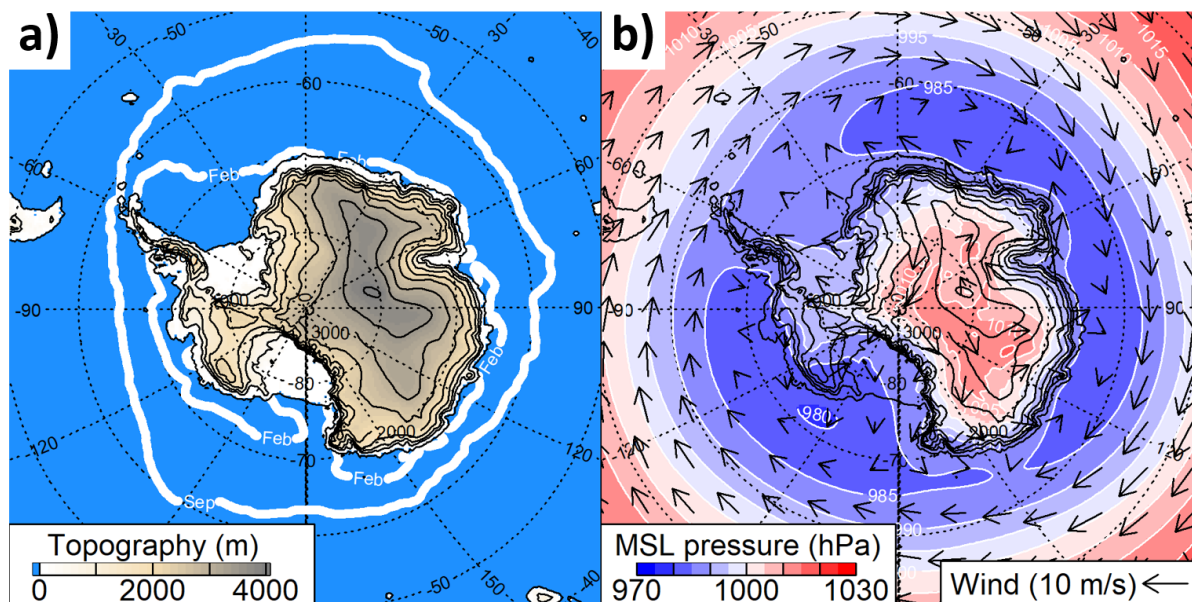


Figure 1.1: a) ERA5 topography (isolines every 500 m) shown as colour. White lines indicate the mean (2000-2020) value of ERA5 sea ice edge (at 15% concentration) in February and September. b) ERA5 mean (2000-2020) 10 m wind and mean sea level (MSL) pressure. ERA5 Dataset: Hersbach et al. [2019]

The sea ice has a strong impact on temperatures as it isolates the cold atmosphere from the (relatively) warm water and the increased albedo further reflects much more sunlight. This causes an inter annual variability with colder temperatures in the winter months (Apr-Sept) and warmer temperatures in the summer months (Nov-Feb). The 2000-2020 mean near surface temperature for February and September shows this alignment with the sea ice cover (Fig.1.2).

Most of continent is covered by an up to 4 km thick ice shield. This means surface temperatures are 20 to 30 K colder than at sea level just because of the altitudes alone (Fig.

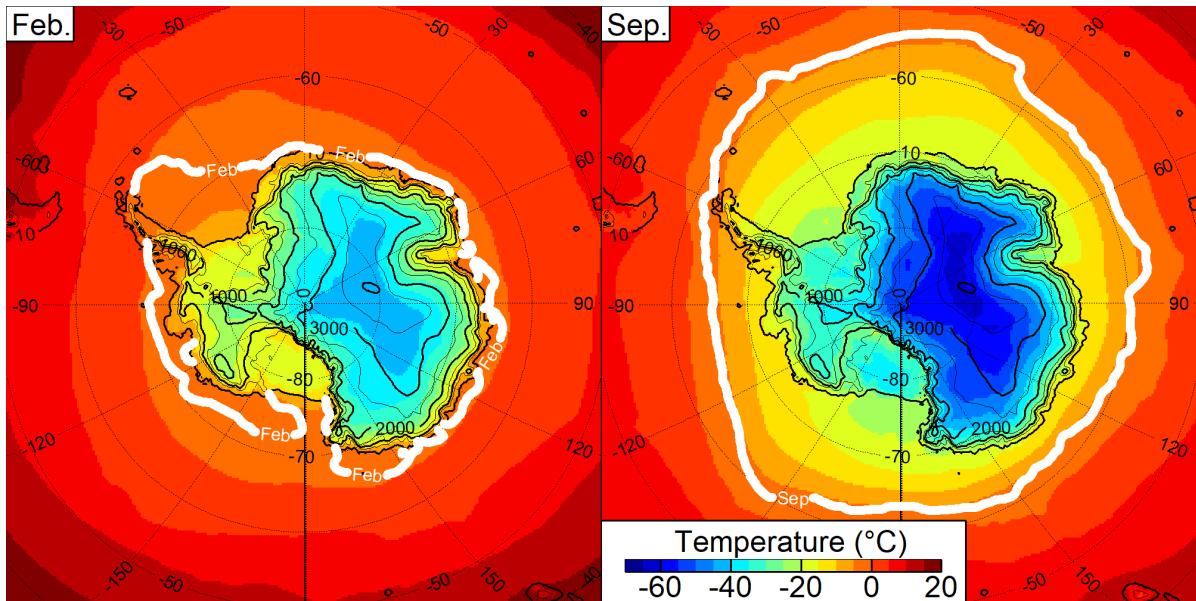


Figure 1.2: ERA5 2 m temperature for February (left) and September (right). Topography is shown as isolines every 500 m and the white line indicates the ERA sea ice edge (at 15% concentration). All values are means over the years 2000-2020. ERA5 Dataset: Hersbach et al. [2019]

1.2). The world's lowest measured temperature of -89.2°C was recorded in 1983 at Vostok station with an elevation of 3420 m.

The wind field around Antarctica is dominated by a circumpolar zone of westerly winds at mid-latitudes that is itself forced by a low pressure belt surrounding Antarctica (Fig. 1.1b). The strength of pressure difference towards lower latitudes is variable and this variability is known as the Southern Annular Mode (SAM) or Antarctic Oscillation [Marshall, 2003]. If the SAM is positive(/negative) the pressure difference is more pronounced and westerlies are stronger(/weaker). The westerlies help drive the Antarctic Circumpolar Current (ACC) which is the ocean current that similarly flows from west to east [Rintoul et al., 2001]. The ACC is of great importance for global ocean circulation as it connects the Atlantic, Indian and Pacific Ocean, thus allowing the exchange of water masses between them. The wind field over the Antarctic continent is largely dominated by katabatic winds that follow downslope directions but are deflected to the left due to the Coriolis force. Higher (mean sea level) pressure over the continent further increases these wind patterns.

Precipitation averages to around an equivalent amount of 10-20 cm water per year with the least precipitation on the Antarctic Plateau (elevation >3000 m) and the most precipitation near the coast [Favier et al., 2013]. Most of the snow falling on top puts pressure on the snow underneath creating firn ice that eventually turns into glacial ice. But part of the snow can be transported by the wind or sublimation can take place. Melted snow or ice, or direct liquid precipitation can evaporate or runoff. The sum of all these factors is referred to as Surface Mass Balance (SMB). The SMB amounts to about 90% of the precipitation and sets the source of ice mass contribution to around 2000-2500 Gt per year [Mottram et al.,

2021]. The sink of glacial ice masses is the ice calving along the coast. Here the ice shelf (the part of glacial ice that floats on the water) destabilizes until icebergs break off and are transported away with ocean currents. The loss of ice mass is similar to the SMB gain but overall a total loss of maybe 100-200 Gt per year can be assumed [Mottram et al., 2021]. The question of total mass loss is very relevant as it contributes to sea level rise.

Overall, Antarctica plays a key role in the global climate system. As solar radiation is strongest at low latitudes, a temperature gradient towards the poles develops and heat is transferred to the south by ocean currents and atmosphere circulations.

1.1 Weddell Sea region

The Weddell Sea lies on the east side of the Antarctic Peninsula (Fig. 1.3). While surface water currents flow from west to east around Antarctica, there is a circular current turning clockwise in the Weddell Sea known as Weddell Gyre [Vernet et al., 2019] that extends to approx. 30°E. Sea ice originating in the east can (partially) follow this movement until in the west near the Antarctic Peninsula and then moving north where it melts (compare sea ice edge for February in Fig. 1.2).

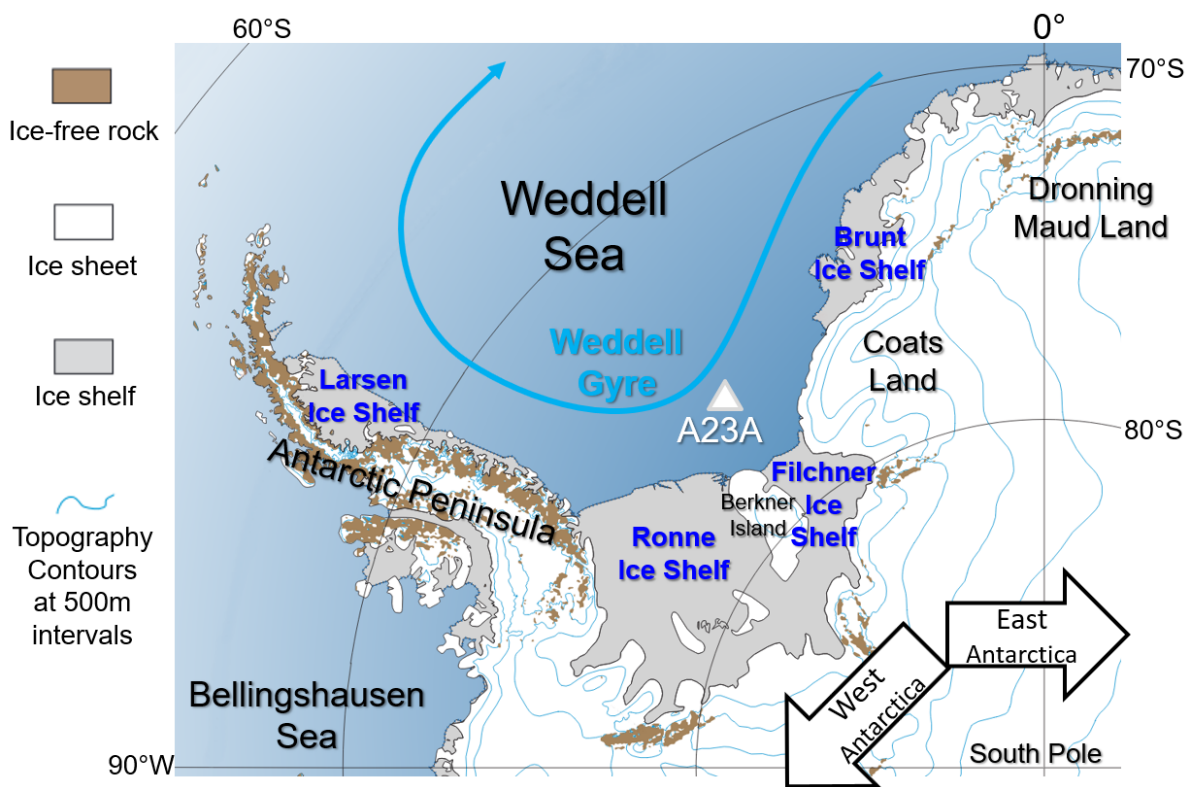


Figure 1.3: Overview of the Weddell Sea region with labels. Location of iceberg A23A for the three decades it was grounded. (Figure adapted from https://lima.usgs.gov/documents/LIMA_overview_map.pdf, last access: 28.02.2023)

Another point of interest in the Weddell Sea is the Iceberg A23A that originated from the Filchner-Ronne Ice Shelf in 1986 and grounded in 1991 [Wesche and Dierking, 2012]. It was grounded for three decades (Fig. 1.3) before starting to move again and finally in 2022 followed the Weddell Gyre current. With its enormous size of approximately 4000 km² it influenced sea ice movement in the region. A fast ice bridge developed for several years between A23A and Berkner Island in the south effectively blocking sea ice movement [Štulić et al., 2023]. This fast ice bridge as well as A23A were additional sources of polynya development. Polynyas develop as wind or surface water movements push sea ice off the ice shelf, iceberg, fast ice or coast and the most pronounced polynyas in the Weddell sea are those that develop in front of the Ronne and Brunt Ice Shelf [Paul et al., 2015]. Polynyas stay open for hours or days and are hotspots for sea ice production during this time as they produce 10% of Antarctic sea ice while making up only 1% of the area [Tamura et al., 2008]. Another form of sea ice opening are elongated cracks in sea ice called leads. They develop due to wind shear or ocean movement shear and have a higher than average occurrence in the Weddell Sea region [Reiser et al., 2019].

Over land, several different wind phenomena can be found. The westerlies coming from the Bellingshausen Sea are forced over the Antarctic Peninsula with an elevation around 1000-1500 m. This can cause foehn winds when the adiabatic lifting of humid air masses causes condensation (clouds) and precipitation on the west side of the Antarctic Peninsula and leaves warm(er) air flowing out on the east side. This effect decreases the stability of the remaining Larsen Ice Shelf [Laffin et al., 2022]. Wind coming from the east (for example driven by a synoptic low pressure system) can be forced against the Antarctic Peninsula and this can cause a barrier wind to develop, as lower air masses are not lifted over the mountain, they channel north along side the mountain range with increased wind speed [Schwerdtfeger, 1975].

Looking at the other side of the Weddell Sea region (Fig. 1.3), the wind field shows katabatic winds coming from the Antarctic Plateau of East Antarctica. The phenomenon of a katabatic jump can be observed when katabatic winds coming from the Antarctic Plateau flow down steep topographic slopes such as Coats Land [Yu and Cai, 2006]. The very fast wind approaches a region with low wind speeds and as it tries to adapt, a hydraulic jump occurs, marked by a decrease of flow speed and an increase in flow height associated with strong turbulence [Ball, 1957, Loewe, 1972]

Over sea ice, nocturnal low level jets can occur as the sea ice isolates the air from the warmer water and thus allows for a stable boundary layer to develop [Andreas et al., 2000]. Note that depending on latitude and time of the year, the night may last up to 24 hours.

The objects of interest in Publication 3 are primarily these different phenomena (barrier wind, katabatic wind and other low level jets).

Concerning precipitation, the phenomenon of atmospheric rivers should be mentioned. These large bands of humidity in the troposphere can transport moisture from lower latitudes to Antarctica. Although atmospheric rivers are estimated to only yield around 13% of total Antarctic precipitation [Maclennan et al., 2022] for Dronning Maud Land, the contribution may be as much as 80% of total precipitation [Gorodetskaya et al., 2014].

1.2 Antarctic observations

Meteorological Antarctic long-term in-situ observations are mainly automatic weather stations (AWSs) [Lazzara et al., 2012] and manned stations. Some of the latter also provide radiosonde data (see Fig. 1.4). The number of radiosonde stations is very comparable to the network maintained in Germany by the German meteorological service (Deutscher Wetterdienst, DWD), although the area of Germany is roughly 40 times smaller. This is to say Antarctic observations are (relatively) scarce.

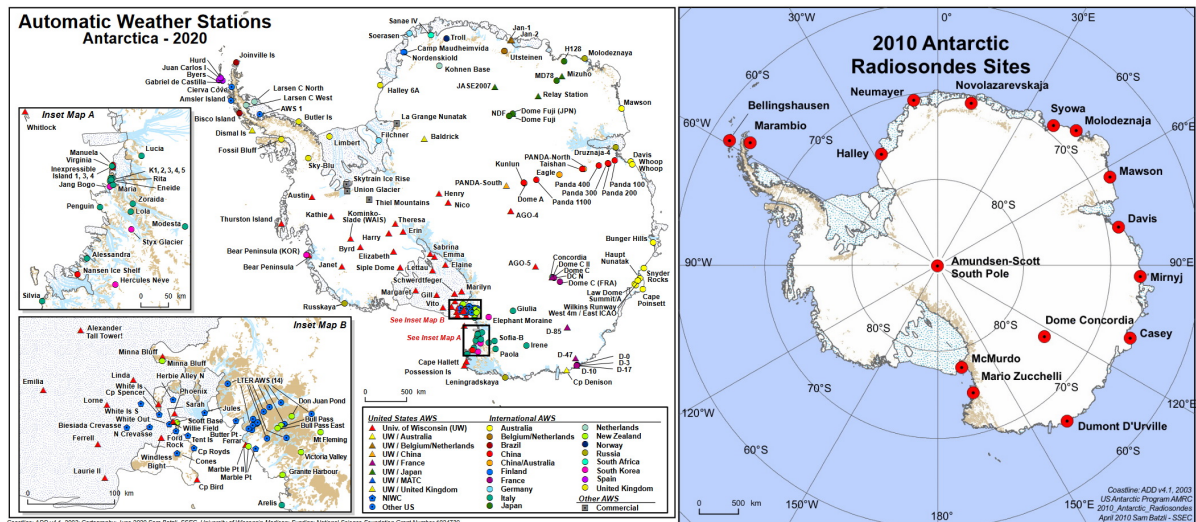


Figure 1.4: Maps showing the location of Automatic Weather Stations in 2020 (left) and Radiosonde Sites in 2010 (right) on Antarctica. (Figures taken from the Space Science and Engineering Center, University of Wisconsin-Madison, <http://amrc.ssec.wisc.edu>, last access: 17.02.2022)

Additional short-term in-situ data (as for Publication 1) can come from experiments and expeditions, but these have a strong bias towards the summer season of the southern hemisphere (October-March). During winter, increased darkness, colder temperatures and more sea ice make everything not-automated much more challenging. Maintenance poses another problem. Even during summer, logistics must be managed and spare parts must be in stock, otherwise, repairs may delay for a season or year.

From 2017 to 2019, the core phase of the Year of Polar Prediction (YOPP) took place as an activity of the Polar Prediction Project (PPP) from the World Meteorological Organisation (WMO) [Jung et al., 2016]. During this time, a Special Observing Period (SOP) for the Antarctic was conducted from November 2018 to February 2019, in which over 2000 additional radiosondes were launched [Bromwich et al., 2020]. These efforts were welcomed by the community and caused the addition of a second SOP for the Antarctic, but this time for the winter period from April to August 2022 [Bromwich et al., 2022].

Apart from these in-situ observations, satellite data also plays a big role because of their spacial coverage. But cloud interference can be a problem and the parameters provided are limited. Cloud cover and height, sea ice concentration, surface temperature and near-surface

wind speed over ocean [Hu et al., 2008] all help, but vertical profiles of e.g. wind speed are not yet established broadly [Witschas et al., 2020].

1.3 Regional climate simulations of Antarctica

Regional climate models (RCM) are numerical models that aim to downscale atmospheric processes from a global climate model (GCM) or from reanalyses. RCMs have a higher resolution that allows for the simulation of processes beneath the GCM scale like complex topographic channeling. If a RCM performs well, the data will be more precise and detailed, thus allowing for a better determination of relevant impacts (see Fig. 1.5a). [Giorgi, 2019]

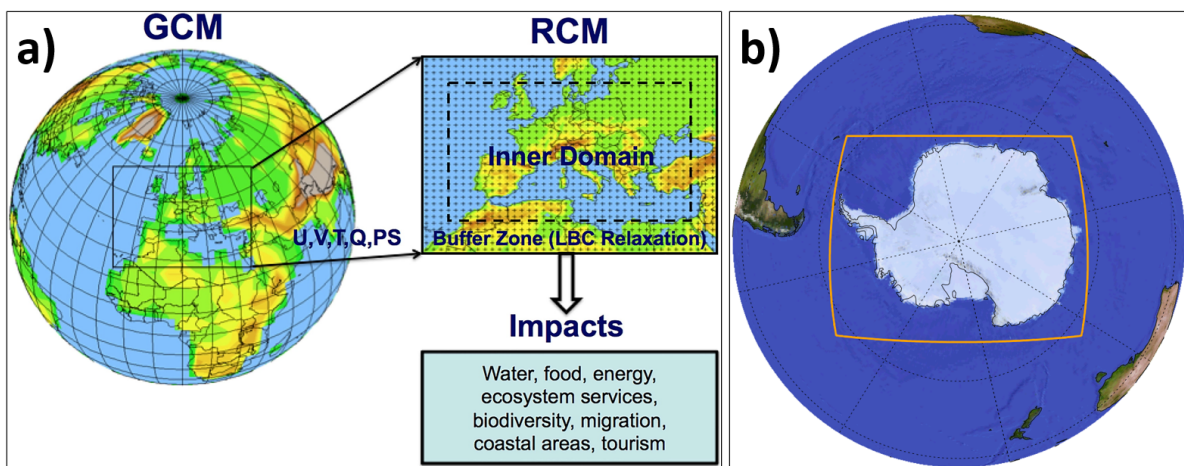


Figure 1.5: a) Schematic depiction of a Global Climate Model (GCM) with a nested Regional Climate Models (RCM). Atmospheric variables like wind (U,V), temperature (T), humidity (Q) and pressure (PS) are transferred to the boundary of the RCM and usually also further inside the Buffer Zone by the use of Lateral Boundary Conditions (LBC) Relaxation. (Figure taken from Giorgi [2019]). b) CORDEX Domain for Antarctica (Figure taken from "Description of the CORDEX domains (23/10/2015 version)", <https://cordex.org/domains>, last access: 22.02.2023))

To allow the RCM a more precise and (hopefully) correct simulation it needs necessarily to deviate from the data of the GCM that is provided as lateral boundary condition (LBC). For this reason, techniques like relaxation [Davies and Turner, 1977] are used that have the effect of gradually changing variables from the low resolution GCM on the edge to the high resolution RCM in the inner domain (see buffer zone in Fig. 1.5a). Different RCMs have been used for Antarctic Regions.

The Polar Weather Research and Forecasting model (Polar-WRF) is an adapted version of the WRF [Bromwich et al., 2013]. Bozkurt et al. [2020] used Polar-WRF to investigate temperature trends on the east and west side of the Antarctic Peninsula and Deb et al. [2018] used it to understand the thinning of ice shelves in the Amundsen Sea.

The Modèle Atmosphérique Régional (MAR) was used by Gallée et al. [2015] to investigate the boundary layer over the Antarctic Plateau in summer and Datta et al. [2019] evaluated ice melt over the Antarctic Peninsula caused by foehn winds. Agosta et al. [2019] used MAR to estimate SMB and Kittel et al. [2021] projected the SMB of Antarctica for the current century.

The Met Office Unified Model (MetUM) [Walters et al., 2017] was used by Elvidge et al. [2014] and Orr et al. [2021] to look at foehn events over the Larsen Ice Shelf and Gilbert et al. [2020] evaluated cloud representation in the model to improve melting estimates of the Larsen Ice Shelf.

The Regional Atmospheric Climate MOdel (RACMO) was used by van Lipzig et al. [2004] near-surface wind field over Antarctica and van Wessem et al. [2018] modeled the SMB with RACMO.

The COnsortium for Small-Scale MOdeling model in CLimate Mode (COSMO-CLM/CCLM) was used for Publication 2 and 3 and thus some more details about the model are given in the next section. Souverijns et al. [2019] also used CCLM in combination with a different surface model to run simulations of Antarctica and Pelletier et al. [2022] coupled even more models together including models for ocean, sea ice and ice sheet, yielding a specialized coupled model for application in polar regions.

Concerning inter-comparisons between RCMs or comparisons to reanalysis and observations data, note that Publication 2 features the latter for CCLM. Carter et al. [2022] compares the surface climatology for RCMs MAR, MetUM and RACMO as well as ERA reanalysis. In Mottram et al. [2021] the SMB estimates from RCMs CCLM, HIRHAM5, MAR, MetUM and RACMO are compared to ERA reanalysis and observations. RCM simulations contribute to the COordinated Regional Climate Downscaling EXperiment (CORDEX, <https://cordex.org>, last access: 10.02.2022) within the subsection Polar CORDEX. The domain for Antarctic CORDEX is shown in Fig. 1.5b. This common ground allows for better inter-comparisons that are needed to estimate uncertainties for climate predictions.

1.4 Regional climate model CCLM

The COnsortium for Small-Scale MOdeling (COSMO) model is developed internationally by several national meteorological services and other participants (www.cosmo-model.org, last access: 10.02.2022). The variant COSMO model in CLimate Mode (CLM) (COSMO-CLM or CCLM) was developed by the Climate Limited-area Modelling (CLM) Community (www.clm-community.eu, last access: 10.02.2022).

CCLM is a regional nonhydrostatic climate model [Rockel et al., 2008, Steger and Buchignani, 2020]. It uses a rotated coordinate system to avoid singularity at the poles and a terrain-following vertical coordinate system. Physics parameterizations include subgrid-scale turbulence, surface layer, grid-scale clouds and precipitation, subgrid-scale clouds, moist convection, shallow convection, radiation, sea-ice scheme and a soil model [Doms et al., 2021].

The CCLM model is used to perform simulations in very different regions, ranging from high [Platonov and Varentsov, 2021] and mid [Buchignani and Mercogliano, 2020] to low latitudes [Fotso-Kamga et al., 2020]. In the last decade, simulations with CCLM contributed

to downscaling global climate projections as CORDEX [Sørland et al., 2021].

The original COSMO model has reached its final version at the end of 2021 (www.cosmo-model.org, last access: 13.03.2023) and a transition is made to the new ICOsahedral Non-hydrostatic (ICON) model which originated in part from CCLM and was developed by the German Weather Service and Max Planck Institute for Meteorology [Zängl et al., 2014]. Although the climate version CCLM is still used, an adapted ICON version for climate modelling is currently being tested [Pham et al., 2021] and may gradually replace CCLM in the future.

Adaptions of CCLM for polar regions as used in this thesis are described in section 2.

1.5 General outline of the thesis

This thesis might be best understood by taking on three different perspectives.

The first perspective is from observation. The idea is that we make and refine measurements to the point where we think they give us the best available representation of nature.

The second perspective is from modelling. The idea here is also that we make and refine simulations to the point where we think they give us the best available representation of nature.

The third perspective is from analysis. The idea here is to use data from observation and/or modelling and to derive new parameters to the point where we think they give us the best available representation of nature. Knowing the uncertainties of measurements or simulations plays a key role in the analyses.

The relation between the publications is best understood by viewing the third publication as the goal. In this third publication, regional climate model simulations are analyzed with respect to a boundary layer climatology and low-level jets. As it uses model data, this data should first be verified (second publication). To further extend possible verifications, own measurements were performed (first publication). An overview scheme is given in Fig. 1.6.

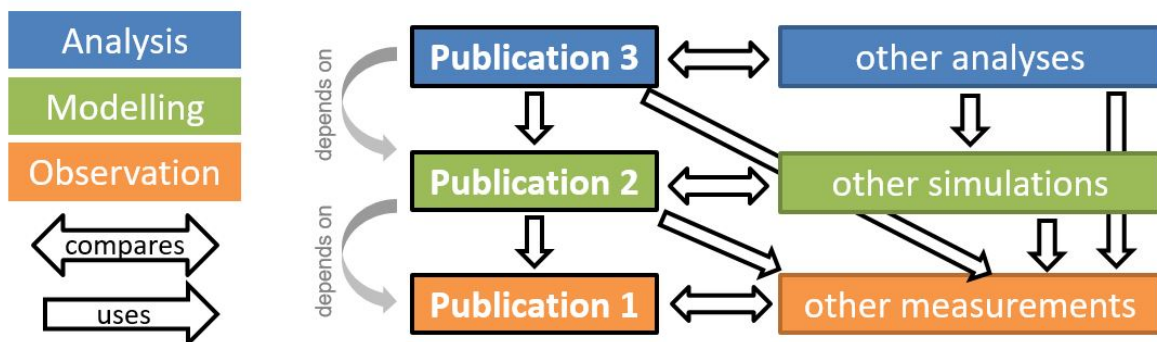


Figure 1.6: Scheme of how the Publications fit-together

In the following, a short overview of the three publications is given. More details on each publication is found in the next section.

Publication 1: Analysis of the performance of a ship-borne scanning wind lidar in the Arctic and Antarctic

A Doppler wind lidar was used on board of the RV Polarstern during an Arctic expedition in 2014 and an Antarctic expedition in 2015/2016. It collected data of horizontal wind speed and direction in vertical profiles up to 2 km height and with a temporal resolution of 10-15 mins. Compared to the 2 or 3 daily radio soundings done by RV Polarstern, these lidar measurements show a high temporal resolution that allows for the verification of simulations on hourly scales (such as in Publication 2).

As it was the first time using a ship-borne wind lidar in the Antarctic (and second time in the Arctic) the general methodology for deriving and correcting had to be adapted to the specific circumstances. These included ship movements due to waves, ice breaking or loading and unloading of cargo.

For the publication, we compared our measurements to radio soundings and direct measurements on RV Polarstern. Our analysis showed results very close to the other measurements and a continued transition from one measurement to the next, giving us a high confidence in the produced data set.

Publication 2: Verification of the regional atmospheric model CCLM v5.0 with conventional data and lidar measurements in Antarctica

A regional climate simulation for the Weddell Sea area spanning the period of 2002 to 2016 was performed. Preliminary verification showed a strong warm bias near the surface in winter over the Antarctic Plateau. We tuned the model and performed a second simulation which yielded better results. In the publication, we presented an extensive verification of the model's temperature and wind data.

Starting with a comparison with data from another model and from reanalyses, we detected no problematic deviation, except for the above mentioned warm bias. Although smaller, this bias is also present in some of the other reanalyses data as well.

In the next step, we used all available long term radio sounding and surface station data to check how the model is performing in the whole atmosphere and near the surface.

To further enhance the verification, new weather buoy data from 2016 and the lidar dataset from Publication 1 were included.

The model verification showed a good agreement with measurements and especially the comparison to the lidar measurements gave a good confidence that the research planned for Publication 3 was feasible.

Publication 3: A Model-Based Climatology of Low-Level Jets in the Weddell Sea Region of the Antarctic

A climatology of Low-Level Jets was done based on the simulated data that was verified in Publication 2. In a first step a search algorithm for LLJ was implemented and refined

repeatedly, until it performed overall very well. Processing the simulation data yielded a new derived data set of LLJ heights and speeds, as well as other parameters.

A comparison with radio soundings and a similar climatology for the arctic was done, which increased confidence in this new data set. Based on this new data set, statistics such as the occurring frequency of LLJ, distribution of heights and speeds were evaluated and some case studies concerning the length of LLJ events were done.

Although such a climatology would have been possible without Publication 1 or 2 by using for example ERA5 data. Publication 2 increased the confidence in the underlying data set and by extension in the climatology. The comparison of the data from Publication 1 (lidar) to the data in Publication 2 (simulation) and removal of the warm bias hints at the better quality of our data compared to ERA5 for such an evaluation.

2 Publications

2.1 Publication 1

As mentioned in the introduction (section 1.2), measurements in Antarctic region are scarce compared to other regions of the world where even non-scientific ships and airplanes can contribute atmospheric measurements. Concerning upper air measurements, almost all regular radio soundings are located along the coast (Fig. 1.4) and are done at most once a day. This means that processes on a sub-daily time scale will not be captured. For this reason, the acquired lidar data set with a temporal resolution of minutes is a valuable asset - that is, after corrections and quality checks as described in Publication 1.

2.1.1 Doppler wind lidar

The Doppler wind lidar¹ is a lidar system that measures wind speed by usage of the Doppler effect. The lidar emits a laser beam with a wavelength in the infrared spectrum that is reflected by aerosols in the atmosphere. The Doppler shift measured by the lidar allows for calculation of the speed relative to the lidar (along the direction of the laser beam).

To derive the wind speeds, linear independent measurements are needed. Generally, at least three, but assuming no vertical velocity at least two measurements with different angles are needed. The use of multiple lidars to achieve this has the advantage of scanning at the same time and the same location (where the beams cross). The downside of this practice is the requirement of more than one lidar and the effort ensuring synchronization between them [Calhoun et al., 2006, Damian et al., 2014, van Dooren et al., 2016]. The more prominent solution is to accept a broader error margin and scanning in short succession in different direction with the same lidar. This entails that the measurements are always representative for the average area over the average time. A common approach is the velocity-azimuth display (VAD) scan [Weitkamp, 2006]. By scanning at a constant elevation with different azimuth angles (see Fig. 2.1a) data is accumulated. The radius of the circle increases with height and thus, the area over which the wind speed will be calculated also increases. For a given height, all radial speeds can be approximated by a sinusoidal function from which the horizontal wind speed and direction can be derived (see Fig. 2.1b).

In practice, the choice of a signal to noise ratio (SNR) threshold is the first step to select usable data. A clear sky with low aerosol concentration may yield not enough reflection, or a cloud might block the beam and so no reflection behind is possible. Either way, this causes

¹The term lidar (**l**ight **d**etection and **r**anging) technically refers to the method but is often also used to refer to the system that uses the lidar method. Note the similarity to the term radar (**r**adio **d**etection and **r**anging).

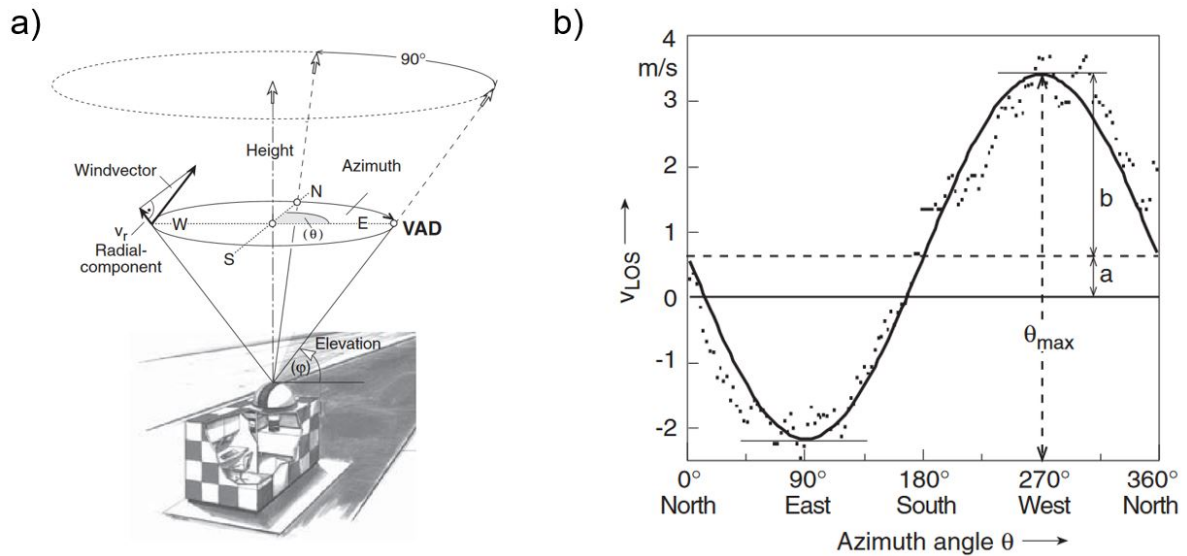


Figure 2.1: (a) Schematic of the scan technique velocity-azimuth display (VAD) of a Doppler lidar. (b) Example of sine fitting of the radial wind velocity by the use of a VAD technique. (Figures adapted from Weitkamp [2006], page339f)

a worse SNR. Based on a check by Päsche et al. [2015], we developed a simple method to choose the SNR threshold. Our idea was to decrease the SNR threshold as far as possible by estimating the noise contamination and capping it at 1%, thus increasing our usable data size. It turned out that different scanning settings (mostly concerning the averaging time per beam) allowed for different SNR thresholds.

2.1.2 Adaptations for ship-born measurements

In opposition to a stationary set up, when a Doppler wind lidar is setup on a moving vehicle such as an airplane [Witschas et al., 2017], satellite [Witschas et al., 2020], buoy [Salcedo-Bosch et al., 2021] or ship [Hill et al., 2008, Achtert et al., 2015] corrections have to be applied. The directional velocity of the vehicle is often easily subtracted, but angular velocities as well as changing orientations and thus changing angles of scanning directions are a bit more of a challenge. For ships, motion-stabilizing platforms have been developed that counteract the problems of angular velocity and orientation changes along the roll and pitch axis [Hill et al., 2008, Achtert et al., 2015].

In our case, this was not as important because of the special circumstance that the ship was surrounded by sea ice most of the time, which hindered the development of waves. On the other hand ice breaking movements, where the ship rams or propels onto ice floes, are additional perturbations in this setting. Luckily, ice breaking was seldom performed in our cruise, but even when done, it often was a procedure of a couple of minutes in preparations followed by a short pitch of the ship. Thus, even during during ice breaking, approximately 90% of the time no additional perturbations were caused.

Our correcting procedure in Publication 1 showed that for our cruise and lidar setup,

angular velocity and orientation changes during a scan pattern like VAD (up to 2min) were negligible. Still, the corrections of roll and pitch turned out to be important for slow changes of orientation, such as unloading cargo or pumping water/fuel from one side of the ship to another.

Key results

The main results of the first Publication are:

- The use of a Doppler wind lidar on a ship without motion stabilizing platform under sea ice conditions still produces a high quality data set. Comparison to radio soundings showed a bias of 0.1 m/s for wind speed and 1° for wind direction. The root mean square deviation was 1 m/s and 10°.
- This data set captures atmospheric conditions that are missed by standard observations. Fig. 2.2a,b show the wind speed and direction for the case study in Publication 1. It can be seen that wind speed direction above 100 m are vastly different to the near surface measurements of RV Polarstern. Furthermore, one radio sounding per day can not capture the development of the three low level jets that each only lasted a couple of hours.
- Moderate quality control of the data is challenging. Although conservative thresholds can easily be taken to yield high quality data, this also causes the loss of often still very good and usable data. While the case study for Antarctica shows that increasing the SNR threshold (Fig. 2.2c) would lead to more data that can still be quality controlled by applying a threshold on the relative fit deviation (Fig. 2.2d), this is not always the case. The other case study for the Arctic presented in Publication 1 shows a case where seemingly good data would be removed by either a strict SNR threshold or relative fit deviation threshold.
- The data set for the Weddell Sea was published under Zentek and Heinemann [2019].

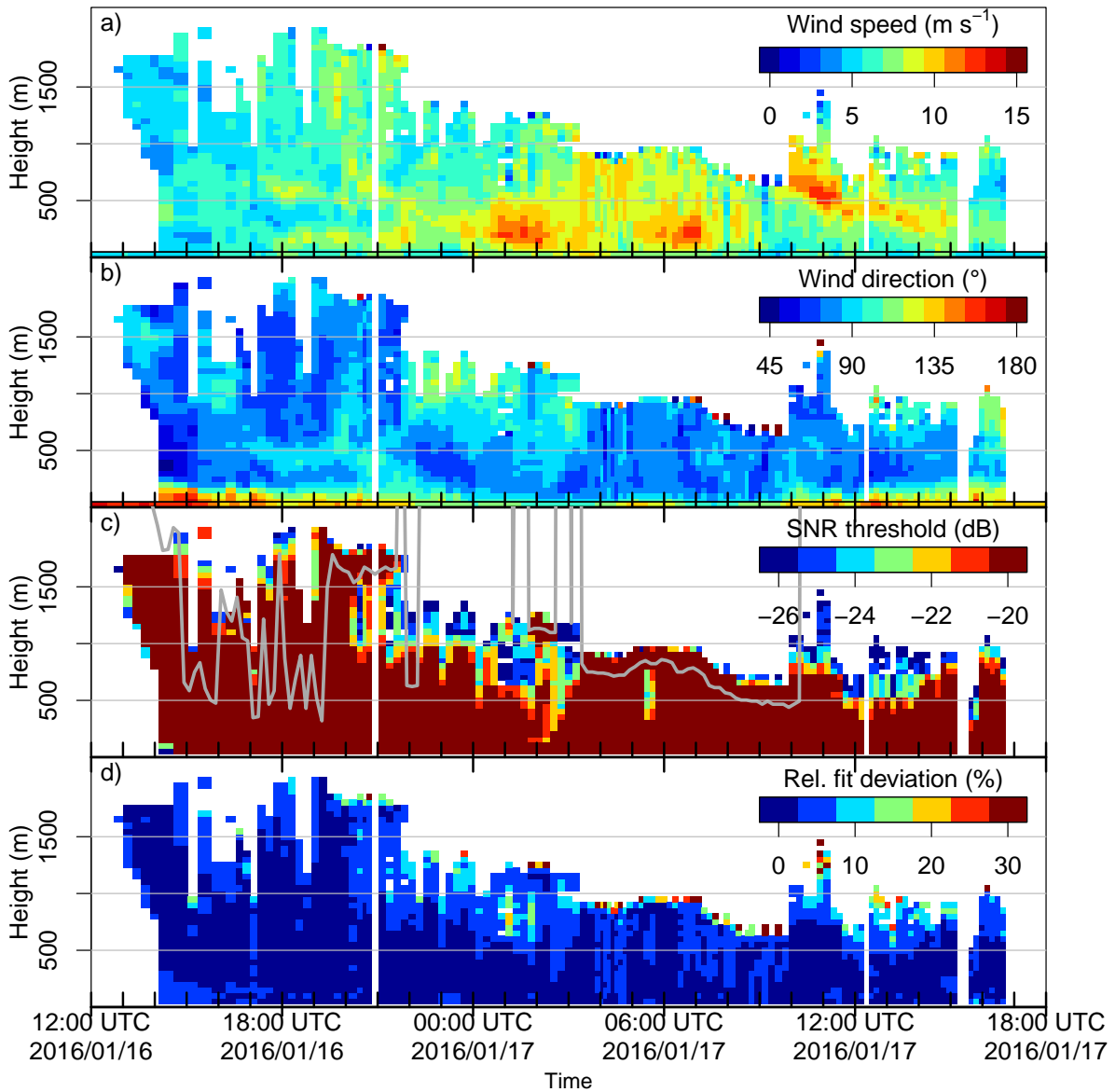


Figure 2.2: Lidar wind speed (a) and direction (b) for the -25 dB SNR threshold for the 16 and 17 January 2016. Colours below the black line (40 m) show the wind measurements of RV Polarstern (anemometer). The plot (c) presents the SNR thresholds that would allow for a wind calculation. The grey line is the cloud base from ceilometer measurements of RV Polarstern. The relative fit deviation (fit deviation divided by wind speed) is shown in (d). Values exceeding the upper limit in (a) and (d) are included in the highest colour bar bin. (Figure taken from Publication 1)

2.2 Publication 2

As mentioned in the introduction (section 1.3), RCMs are a tool to study processes (and thus impacts) that are not resolved by GCMs. One example from the introduction is that of foehn winds over the Antarctic Peninsula which contribute to the melting of the Larsen Ice Shelf. Another example is that of open water polynyas which contribute to the sea ice production and thus influence ocean processes due to the production of high-salinity water.

More generally, modelling data fills the gaps between measurements. Simulations allow educated guesses about regions and times where no (or less) data is collected. Obviously, all climate future predictions fall into that category.

No matter the application of such a modelling data set, a verification as in Publication 2 is needed first to give estimates which data to trust, which systematic errors can be expected, and which data should be used with caution (or not at all).

2.2.1 Adaptations of CCLM for polar regions

Over the last decade, several improvements to CCLM have been made to enhance performance for polar regions. The first changes included the addition of a thermodynamic sea ice module [Schröder et al., 2011] and change of heat capacity and heat conductivity coefficients in the soil model to better simulate the snow and firn. Later, the sea ice module was further improved by adding temperature-dependent albedo of sea ice (accounting for melt ponds) as well as the addition of a tile approach [Gutjahr et al., 2016].

For Publication 2, the diffusion coefficients for heat and momentum are able to become even lower and a parametrization for turbulence caused by subscale inhomogeneity was deactivated. In combination, this allows an even more stable stratification of the atmospheric boundary layer (ABL). A very stable ABL is realistic during wintertime over the Antarctic Plateau, as shown in Publication 2. Furthermore, topography data was taken from Schaffer et al. [2016], as the default topography was missing the ice shelves.

After Publication 2, the sea ice module was further improved [Heinemann et al., 2021]. Changes include a variable snow layer height, penetration of solar radiation through snow and ice and a better averaging of transfer coefficients.

Other working groups focused on different aspects and adapted CCLM to polar regions in different ways, but the important changes are similar [Souverijns et al., 2019].

Table 2.1: Overview of improvements to CCLM.

Improvement	Publications
thermodynamic sea ice module and better representation of firn	Schröder et al. [2011]
temperature depended albedo and tile approach for the sea ice module	Gutjahr et al. [2016]
better parametrization of turbulence in the ABL	Publication 2
updates to sea ice module and tile approach	Heinemann et al. [2021]

As forcing, the reanalysis data ERA-Interim [Dee et al., 2011] from the European Centre for Medium-range Weather Forecasts (ECMWF) was used. This data has a horizontal resolution of 80 km and is available every 6 hours. However, data for sea ice concentration was substituted by daily high resolution satellite data from: AMSR-E (Advanced Microwave Scanning Radiometer – for Earth observing system), AMSR2 (Advanced Microwave Scanning Radiometer 2) and SSMIS (Special Sensor Microwave Imager/Sounder) [Ezraty et al., 2007, Spreen et al., 2008].

2.2.2 Performed verification

For the verification, we concentrated on temperature, wind speed and direction. The initial CCLM setup (C15) had a large warm bias over the Antarctic plateau for winter. With the above mentioned changes to the model (T15), the warm bias was removed in the right way as not only the surface temperature was too warm, but the temperature profile in the lowest 1km had a wrong shape (Fig. 2.3a). As the whole temperature profile in the winter ABL was corrected, this allowed for a more stable boundary layer to develop, which entails a stronger decoupling of different wind layers and thus allows for stronger changes in wind direction with height. Therefore, this changed setup also caused a decrease of the wind direction bias (Fig. 2.3b).

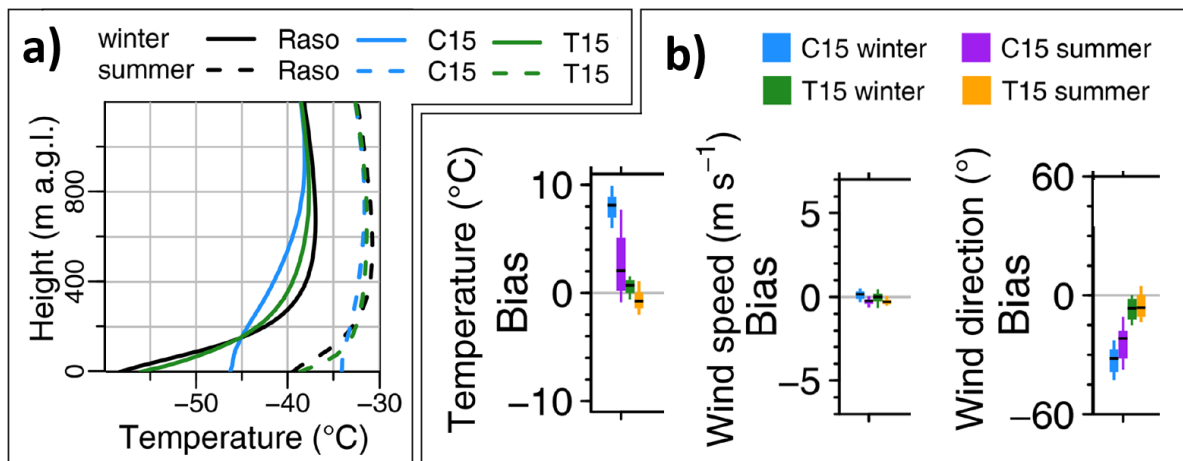


Figure 2.3: a) Mean temperature of radio sounding (Raso; black), C15 (blue), and T15 (green) during winter (solid line) and during summer (dashed line) for Amundsen–Scott station at the South Pole. The abbreviation a.g.l. is short for “above ground level”, meaning above the surface. b) CCLM 2m temperature bias for C15 winter (blue) / summer (purple) and T15 winter (green) / summer (orange) for Amundsen–Scott station at the South Pole. Boxes indicate the 25%/75% quantiles, and whiskers indicate the 10%/90% quantiles; the median is indicated by a black line inside the box. Bias is calculated for every month. (Figure adapted from Publication 2)

These model improvements lay an important ground base for Publication 3 as the winds

in the ABL are analysed and the domain covers part of the Antarctic Plateau. Improved simulations of katabatic winds can be expected and therefore better insights into the behaviour of Antarctic wind systems.

Measurements over sea ice are not as available as those over land (Table 2.2). Still, a comparison of almost one year of automatic weather buoys data showed a temperature bias (RMSE) around $\pm 1^\circ\text{C}$ ($3\text{-}4^\circ\text{C}$) and as wind speed bias (RMSE) of up to 1 m/s (2 m/s). And the comparison with the lidar data set from Publication 1 showed no wind speed bias and RMSE around 2-2.5 m/s while the bias (RMSE) of wind direction was around -5° (30°). All in all, this also increases the confidence in the simulated wind data over sea ice areas. Furthermore, in case studies for times where lidar measurements were available, it was shown that CCLM was able to simulate low level jet (LLJ) events over sea ice. However, we found differences in height, strength and timing of those LLJs.

Table 2.2: Overview of comparisons.

Comparison	Variable	Time range	Dimension
other model and reanalyses	temperature, wind	hourly data over years	2d and time
surface measurements (land)	temperature, wind	hourly data over years	time
surface measurements (sea ice)	temperature, wind	hourly data over months	time
radio sounding (land/coast)	temperature, wind	daily data over years	1d and time
lidar measurement (sea ice)	wind	hourly data over days	1d and time

Key results

The main results of the second Publication are:

- The determination of a large temperature bias over the Antarctic Plateau in winter for the default CCLM setup together with new setup to remove the bias.
- Overall good performance of simulated temperature and winds compared to other models and observations with temperature biases (RMSE) usually less than $\pm 2^\circ\text{C}$ (5°C) and Wind speed biases (RMSE) usually less than ± 2 m/s (5 m/s).
- Due to the immense data size, only part of the data was published under Zentek and Heinemann [2022a,b,c,d].

2.3 Publication 3

Compared to the convective boundary layer where the lowest part of the troposphere is well mixed, the neutral or stable boundary layer (SBL) inhibits vertical exchange and transport. But as the stable layering decouples the wind, this allows for an increase in wind speed, that causes wind shear which in turn enables vertical transport. This SBL is very common for

Antarctica due to the polar night and an extensive sea ice cover that isolates the boundary layer from the ocean. Additionally katabatic winds form over the whole continent. All this makes the study of low level jets a relevant research goal in order to better understand these regions.

2.3.1 Low level jet

A low level jet (LLJ) is a maximum of horizontal wind speed in a vertical profile of the lower troposphere. But what exactly constitutes "low" or a "maximum" is subjective. Fig. 2.4 shows examples of wind profiles that should be considered, when defining a LLJ in a more precise way.

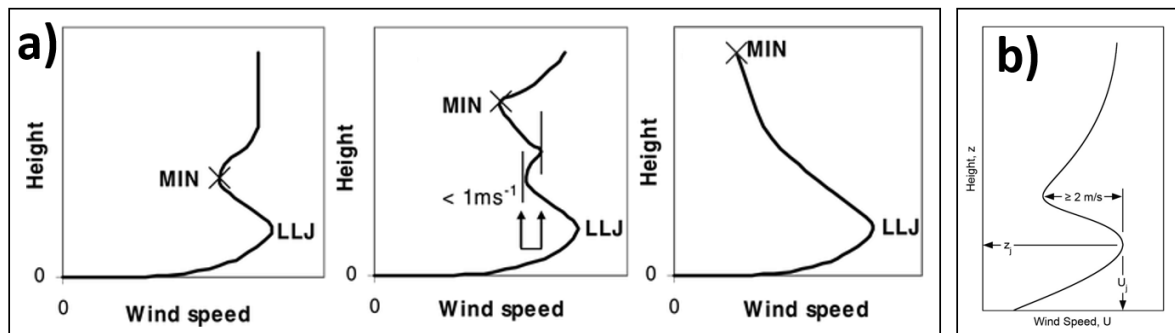


Figure 2.4: Schemata of vertical wind profiles and how a LLJ may be defined. a) Different profiles and how the minimum (MIN) above the LLJ is selected (Figure adapted from Baas et al. [2009]). b) Depiction of the absolute criterion, where the LLJ is 2 m/s faster than the next minimum above (Figure adapted from Tastula et al. [2012])

Once a maximum and a minimum candidate are determined in some way, there are two common criteria found in the literature [Baas et al., 2009, López-García et al., 2022, Tastula et al., 2012, Tuononen et al., 2015]. The first is an absolute criterion, where the maximum speed exceeds the minimum speed by an absolute value (commonly 2 m/s), the second is a relative criterion, where the maximum speed exceeds the minimum speed by a certain percentage (commonly 25%). Often, a combination of both criteria is used.

Concerning the maximal allowed height of a LLJ so that it may still be considered low, different values are found in the literature depending on the data and goals. Examples are values of 500 m [Baas et al., 2009], 1000 m (Publication 2) and 1500 m [Tuononen et al., 2015].

Depending on the data set that is used, other criteria may be added. For example, the potential minimum candidate can be neglected if the minimum is less than 1 m/s compared to the next maximum (see Fig. 2.4a). Usually, a cap is placed on the maximal height for the search of the next minimum above the LLJ if it is not already limited by the data set. Table 2.4 shows an overview of the above mentioned differences.

Table 2.3: Overview of LLJ definitions: Absolute criterion (abs. crit.), relative criterion (rel. crit.), maximal height of LLJ (max LLJ), maximal height of the minimum (max heighth). If the data set used had a natural low maximum height (e.g. tether sondes) this is indicated by a "M" for measurement.

Study	abs. crit.	rel. crit.	max LLJ	max heighth
Andreas et al. [2000]	2 m/s	-	-	(M)
Baas et al. [2009]	2 m/s	25%	500m	(M)
Banta et al. [2002]	0.5-1.5 m/s	-	-	(M)
Jakobson et al. [2013]	2 m/s	-	-	(M)
López-García et al. [2022]	2 m/s	25%	1500 m	4000 m
Tastula et al. [2012]	2 m/s	-	-	-
Tuononen et al. [2015]	2 m/s	25%	1500 m	1500 m
Publication 3	2 m/s	0-25%*	1000 m	1500* m

(*) note that in Publication 3 the rel. crit. was defined as reciproc, so 20% decrease would be equal to the 25% increase from other studies. Also, a search radius around the LLJ was applied limiting the height even further.

The choice of definition has a major impact on the results. In Publication 3, we found that applying the relative criterion can reduce the number of found LLJ to approximately half. López-García et al. [2022] showed that the increase of the upper bound of possible minima from 1500 m to 4000 m had almost no impact on the detection of LLJs for profiles from radio sounding, but increased the amount of LLJs found for the ERA5 data set by approximately 50%. However, it can be debated if these cases should still be considered as LLJ.

2.3.2 Low level jet climatology

In Publication 3, a climatology of LLJs for the Weddell Sea was based upon the 15 year long simulations from Publication 2. For every hourly model output and every grid point, the vertical profile was searched for a LLJ and, if found, the following five parameters were determined: LLJ wind speed, LLJ height, relative wind speed decrease to the found minimum and the difference of potential temperature and wind direction between the height of the LLJ and near the surface. For further analysis we also searched those vertical profiles for inversions and determined their height and strength.

A comparison with Tuononen et al. [2015], whose LLJ definition we expanded, showed similar results for comparable regions in the Arctic (Greenland, sea ice and ocean). Furthermore, we compared the distribution of the LLJ parameters to four stations with radio sounding data at the Weddell Sea coast and one station in the inland. The distributions for the coastal region were similar but big differences for the inland station were found. We argued that in that case, the radio sounding data is unreliable as the height of LLJs in the simulation was mostly below 100 or 200 m, where radiosonde still shows pendulum motion from the initial acceleration and data is filtered to remove this noise. For LLJs over sea ice,

the comparison of the simulation in Publication 2 to lidar data from Publication 1 gives a rough estimate of the reliability of the determined LLJ parameters.

The mean winter values of the LLJ occurrence frequency, wind speed and height are shown for the 15 year simulation in Fig. 2.5. At a first glance, we can see the LLJ occur $\sim 80\%$ of the winter time over the slopes of the Antarctic Plateau while less than 30% of the time over sea ice. Over the whole slopes of the Antarctic Plateau, the mean height of LLJ is below 200 m but the mean speed increases from below 15 m/s to 20 m/s as the katabatic wind flows downward. The signature of sea ice extent can also be seen in the mean height with values around 300 m over sea ice and above 400 m over open ocean.

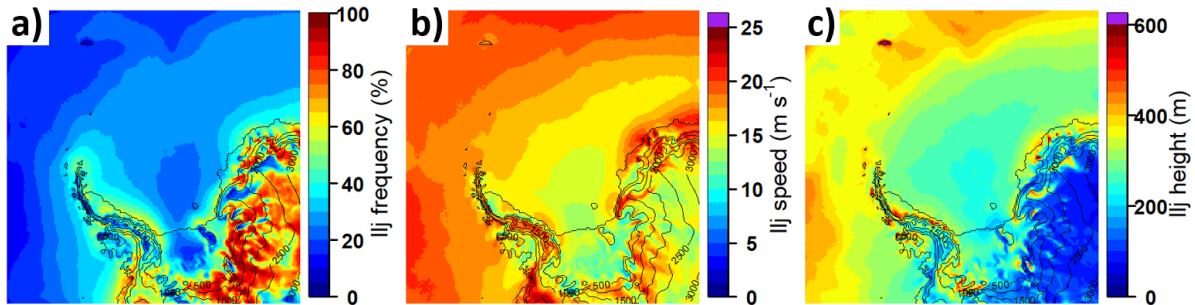


Figure 2.5: LLJ frequency (a) speed (b) and height (c) for winter 2002–2016 (Figure adapted from Publication 3)

Key results

The main results of the third Publication are:

- An evaluation of the relative criterion for LLJ, as we performed a sensitivity study for 0% (that is no relative criterion) up to 25%. With 25%, only strongly pronounced LLJs are found that make up about half of the LLJs otherwise found with no relative criterion. The reduction of classified LLJ is continual and homogeneously spread across all heights and speeds, except for the weaker LLJ, as a 10 m/s LLJ with an absolute criterion of 2 m/s always fulfills even the 20% criterion.
- Distribution comparison of all LLJ parameters with observations showed good agreement for the 4 coastal stations. For the radio soundings at the South Pole, LLJs were seldom found, which is most likely due to the unreliability of the data in the first couple of 100 m. Occurrences of LLJ found in the model are thus higher and fit the expected height and speeds better.
- A study of LLJ event length showed different distributions, with many regions where LLJs last only hours up to a day, and regions like the southern end of the Filchner-Ronne ice shelf where LLJs last up to 10 days during winter.
- The LLJ data was published under Zentek and Heinemann [2022], Zentek and Heinemann [2022e].

3 Outlook

Future of model developments

Regular grids with the same horizontal spacing or spectral models are the default for GCMs. Another option is to use an unstructured grid that can be refined for certain regions but stays fixed for the whole simulation. This approach is used by ICON (the successor of COSMO) and is an alternative to the nesting of a RCM into a GCM as both the coarse global and fine regional simulations can be done at the same time.

In the past, there has also been some research on adaptive grids for GCMs that allow for a refinement during the runtime, but application was restricted to certain components [Jablonowski et al., 2004, Abiodun et al., 2008, Chen et al., 2021]. For simulations below the scale of RCMs, so called large eddy simulation, this approach has also been tested [van Hooft et al., 2018].

Another aspect of climate modelling is the online coupling of different models, especially combining an atmospheric and ocean model. When done in combination with an unstructured grid as in Jungclaus et al. [2022], these system may be the way regional climate forecasts are made in the future. Giorgi [2019] describes the transition toward convection permitting models as the key aspect for the future of regional climate modelling. For this, the model resolution needs to approach the kilometer scale, but this can also lead to new challenges: if datasets with different reference systems are used, the conversion should not be overlooked [Monaghan et al., 2013]

Follow-up research

Subsequent to Publication 1 we processed Doppler wind lidar data for 4 expeditions in the Arctic [Zentek et al., 2019a,b,c,d] and 2 in the Antarctic [Zentek and Heinemann, 2019, Zentek et al., 2019e]. A multi-month data set of lidar data for the Multidisciplinary drifting Observatory for the Study of Arctic Climate (MOSAiC) campaign [Shupe et al., 2022] was also published [Heinemann et al., 2023].

Although our previous processing of the lidar data focused on vertical profiles of horizontal wind, the lidar often also included other scanning patterns that allow for processing of horizontal profiles of horizontal wind speed or different turbulence analysis.

Follow-up research of Publication 2 includes the already mentioned updates to sea ice module and tile approach [Heinemann et al., 2021]. This new model version has been applied for Arctic regions [Heinemann et al., 2021, 2022] and further evaluations with observational data from MOSAiC (including lidar data) will be conducted in the future.

For the Antarctic, we used the new model version to run climate simulation covering the CORDEX domain (Fig. 1.5b). We simulated the beginning (2000-2014), mid (2036-2050) and end (2086-2100) of the century. As forcing, we used the SSP3-7.0 scenario from AWI-CM CMIP6 data [Semmler et al., 2020].

Following Publication 3, this new Antarctic wide simulation was used to determine a possible change in the LLJ climatology in the near future. First evaluations are shown in Fig. 3.1. The new simulation reveals that on the top of the Antarctic Plateau, the katabatic wind has not yet developed and almost no LLJ are found. For the end of the century, the simulation predicts less LLJ occurrence as the frequency drops from around 30% by 5% to 25% for most sea ice areas (3.1b). We assume this is caused mostly by the sea ice reduction at the end of the century in the forcing data set.

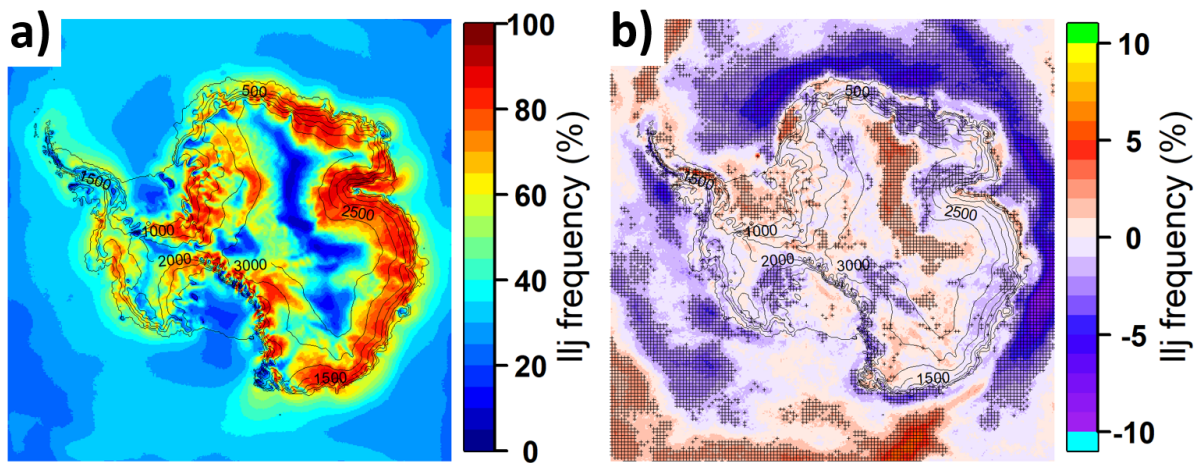


Figure 3.1: LLJ frequency for 2000-2014 (a) and change (subtracted) of LLJ frequency by 2086-2100 (b) for the downscaled SSP3-7.0 scenario. The cross-shaded areas mark significant ($p < 0.1$) differences.

4 Appended publications

4.1 Authors contributions

(copied from each publication)

Publication 1:

Authors: Rolf Zentek (RZ), Svenja H. E. Kohnemann (SK), and Günther Heinemann (GH)
RZ carried out the investigation (measurements on PS96), data curation, methodology, formal analysis, verification, software, visualization and writing of the original draft. SK carried out the investigation (measurements on PS85), verification, a review of the writing and editing. GH carried out the investigation (measurements on PS96), conceptualization, methodology, a review of the writing, editing, supervision, project administration and funding acquisition.

Publication 2:

Authors: Rolf Zentek (RZ) and Günther Heinemann (GH)
RZ carried out the setup of the model, simulation, data curation, methodology, validation, visualization, and writing of the original draft. GH carried out the conceptualization, methodology, review of the writing, editing, supervision, project administration, and funding acquisition.

Publication 3:

Authors: Günther Heinemann (G.H.) and Rolf Zentek (R.Z.)
Conceptualization, G.H. and R.Z.; methodology, G.H.; software, R.Z.; formal analysis, R.Z.; data curation, R.Z.; writing—original draft preparation, G.H.; writing—review and editing, G.H. and R.Z.; visualization, R.Z.; supervision, G.H.; project administration, G.H.; funding acquisition, G.H. All authors have read and agreed to the published version of the manuscript.

4.2 Publication 1

distributed under the Creative Commons Attribution 4.0 License
<https://creativecommons.org/licenses/by/4.0/>



Analysis of the performance of a ship-borne scanning wind lidar in the Arctic and Antarctic

Rolf Zentek, Svenja H. E. Kohnemann, and Günther Heinemann

Department of Environmental Meteorology, University of Trier, Trier, Germany

Correspondence: Rolf Zentek (zentek@uni-trier.de)

Received: 8 May 2018 – Discussion started: 25 May 2018

Revised: 28 August 2018 – Accepted: 23 September 2018 – Published: 19 October 2018

Abstract. In the present study a non-motion-stabilized scanning Doppler lidar was operated on board of RV *Polarstern* in the Arctic (June 2014) and Antarctic (December 2015–January 2016). This is the first time that such a system measured on an icebreaker in the Antarctic. A method for a motion correction of the data in the post-processing is presented. The wind calculation is based on vertical azimuth display (VAD) scans with eight directions that pass a quality control. Additionally a method for an empirical signal-to-noise ratio (SNR) threshold is presented, which can be calculated for individual measurement set-ups. Lidar wind profiles are compared to total of about 120 radiosonde profiles and also to wind measurements of the ship.

The performance of the lidar measurements in comparison with radio soundings generally shows small root mean square deviation (bias) for wind speed of around 1 m s^{-1} (0.1 m s^{-1}) and for wind direction of around 10° (1°). The post-processing of the non-motion-stabilized data shows a comparably high quality to studies with motion-stabilized systems.

Two case studies show that a flexible change in SNR threshold can be beneficial for special situations. Further the studies reveal that short-lived low-level jets in the atmospheric boundary layer can be captured by lidar measurements with a high temporal resolution in contrast to routine radio soundings. The present study shows that a non-motion-stabilized Doppler lidar can be operated successfully on an icebreaker. It presents a processing chain including quality control tests and error quantification, which is useful for further measurement campaigns.

1 Introduction

Changes in the Arctic and Antarctic climate system are strongly related to atmosphere–ocean–ice interactions and feedbacks between the atmospheric boundary layer and the free atmosphere. Hence, the knowledge about the state of the atmospheric boundary layer (ABL) is crucial for the understanding of atmosphere–ocean–ice processes, atmospheric transport, air pollution processes and the verification and improvement of numerical weather forecast and climate models for polar regions. Profiles of wind speed and direction at high spatial and temporal resolutions are fundamental meteorological quantities for ABL studies. While at midlatitudes the ABL is studied using tall towers and ground-based remote-sensing instruments such as lidar, radar or sodar at several observatories, these measurements are rare or absent in the Arctic and Antarctic. Thus radiosondes are generally the main source for measuring quantities of the ABL in the polar regions. Since the radiosonde stations are primarily located over land, there are huge data gaps over the ocean. Furthermore, the temporal resolution of radio soundings is generally of the order of a couple of hours. Over the polar oceans, only a few research vessels provide radio soundings, which are very valuable for improving the initial conditions for numerical weather forecasts and for reanalyses (e.g. Dee et al., 2011), but are insufficient for detailed studies of boundary layer processes.

Ship-based Doppler lidar measurements are able to fill the gap in radio soundings over oceans, since they provide wind profiles with high spatial and temporal resolutions (Tucker et al., 2009; Achtert et al., 2015). In addition, Doppler wind lidar measurements allow for the determination of the turbulence structure of the ABL (Banta et al., 2006; Pichugina et al., 2012; Kumer et al., 2016). If two Doppler lidars are

available, techniques like the “virtual tower” can be applied (Calhoun et al., 2006; Damian et al., 2014). In synergy with additional remote-sensing instruments measuring the temperature profile, the turbulent mixing conditions in the ABL can be described at high temporal and vertical resolutions of 10 min and 10 m (Brooks et al., 2017). Note that our literature research was focused on lidars similar to our own; thus it is likely biased towards lidars from the same manufacturer.

In this study we analyse data from a scanning Doppler lidar on board of RV *Polarstern* in the Arctic (June 2014) and Antarctic (December 2015–January 2016). There are two important aspects of measuring with a Doppler lidar on board of a moving ship in polar regions: (a) the ship’s movement requiring data corrections regarding its orientation and (b) the adaptation of lidar measurement settings and analysis configuration for conditions with low backscatter due to the low aerosol concentration. Some studies present measurement campaigns dealing with challenge (a) (e.g. Pichugina et al., 2012; Tucker et al., 2009; Achtert et al., 2015). All of them use a motion-stabilization platform to remove the effects of the ship’s motion. We present a different option to deal with the varying orientation of the ship. The adaptation of measurement settings for the polar environment (challenge b) is less documented. The goal of these adaptations is the improvement of the signal-to-noise ratio (SNR). Hirsikko et al. (2014) recommend the use of an optimized telescope focal length of the lidar and an increase in the integration time for measurements in Finland. The main goal of the present paper is the assessment of the wind lidar performance in comparison with radiosondes on the German icebreaker *Polarstern*. A similar study was made by Achtert et al. (2015), who used a motion-stabilized scanning wind lidar during a cruise of the Swedish icebreaker ODEN in the Arctic in 2014 (Tjernström et al., 2014). Their 3-month campaign started immediately after our Arctic campaign in 2014. No ship-based measurement campaign of a Doppler wind lidar is known for the Antarctic. The combination of the measurement framework and the presented comprehensive analysis of the settings serve as a basis for improvements in further data collections. The outline of the paper is as follows: in Sect. 2 an overview of the measurement campaigns and the data processing is given. Section 3 presents the results for intercomparisons of lidar data with radiosondes and the ship’s wind measurements. Two case studies are shown in Sect. 4. A summary and conclusions are given in Sect. 5.

2 Measurements and data processing

The measurements were performed during the two *Polarstern* cruises PS85 and PS96 of the Alfred Wegener Institute Bremerhaven (Germany). The cruises are shown in Fig. 1 with approximate sea ice conditions during the measuring periods. PS85 took place in the Arctic from the 6 June to 3 July 2014 and PS96 in the Antarctic from the 6 December 2015 to 14 February 2016. Lidar measurements were

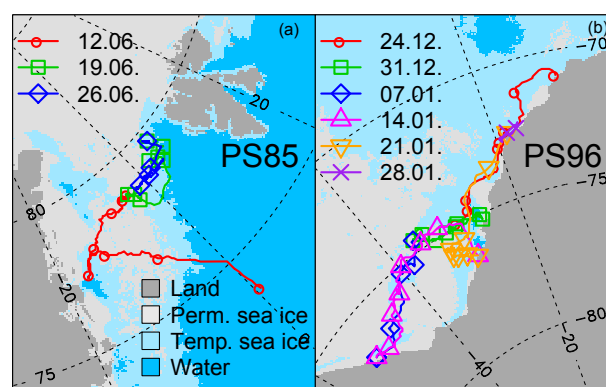


Figure 1. Cruise track of *Polarstern* during PS85 (a) and PS96 (b) with different colours for every week (symbol mark every day 00:00 UTC). Beside land (dark grey) and water (dark blue), sea ice concentration (> 15 %) during the measuring period is shown to be present every day (light grey) and present at least 1 day (light blue). Sea ice concentration is taken from AMSR2 (Spren et al., 2008).

Table 1. Characteristics of the lidar measurements.

Wavelength	1.5 μm (eye-safe, class 1 m)
Gate length	18 m
Points per gate	6 (overlapping for PS96)
Band width	$\pm 19.4 \text{ m s}^{-1}$
Resolution	0.038 m s^{-1}
Measurement error	ca. 0.1 m s^{-1} (depending on SNR)
Pulse rate	10 kHz
Beam range	30–3600 m
Beam focus	variable (300–1800 m)
Averaging time	variable (1–30 s)
Scanning horizontal	$0\text{--}360^\circ$
Scanning vertical	$-15\text{--}90^\circ$

taken for a period of 18 days (12 to 29 July) during PS85 and for 38 days (24 December to 30 January) during PS96. *Polarstern* is the German research icebreaker and has a length of 118 m and a weight of 17 300 tons (Fig. 2). The typical cruise speed is 12 knots.

2.1 Doppler wind lidar

The instrument is a Halo Photonics Stream Line Doppler wind lidar, which is a scanner and can operate with a maximum range of 10 km, but was used only for a range up to 3600 m due to the low aerosol concentration (Table 1). The lidar was installed on the port (starboard) side of the ship during PS85 (PS96) approximately 20 m above the waterline (see Fig. 2). Besides the lidar, an external attitude and heading reference system (AHRS; XSENS MTi-G-700-GPS/INS) was installed for higher-frequency (sampled with up to 400 Hz) recordings of the ship’s pitch and roll, in addition to lower-frequency (1 Hz) navigation data from the ship’s internal systems.



Figure 2. Position of the lidar on the RV *Polarstern*.

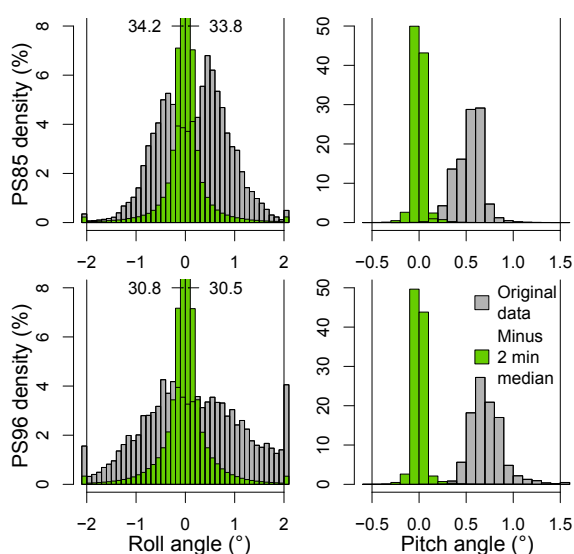


Figure 3. Frequency distribution of the ship angle (grey) and ship angle minus a 2 min running median (green) during the measurement time.

A variety of different scanning programs were used: vertical azimuth display (VAD), horizontal stare in two or three directions, range-height indicator (RHI) and vertical stare. In the present paper we will focus on the VAD measurements that allow the computation of vertical profiles of horizontal wind speed. One VAD scan is composed of eight rays with fixed elevation and different azimuth (0, 45, 90, 135, 180, 225, 270, 315°). During PS96 we changed the elevation from 85 to 75° after 3 days. The averaging time for each ray was usually 12–15 s. During PS85 the averaging time for each ray was only 1.5 s but azimuth circles were done at 25, 50 and 75° elevation. For the analysis we will either use only the 75° or all 25, 50 and 75° elevations. To make them comparable when using all three elevations, we will count the $3 \times 8 = 24$ rays as one VAD. One ray is divided into sections of 3 m length and one measured Doppler velocity is representative for gate length of six sections (18 m). During PS85 those six sections were non-overlapping; thus measurements were available every 18 m. During PS96 the six sections were

overlapping; thus measurements were available every 3 m. But the measurements with overlapping sections are not independent as they are computed based partially on same data. VAD wind profiles are typically available every 15 min and a whole VAD scan required about 2 min for PS96. Photos of the weather condition were taken manually for special situations during PS85 and automatically with a GoPro (with constant power connection) every minute during PS96.

2.2 Radiosondes

Radiosondes at *Polarstern* (König-Langlo, 2014a, 2016a) were usually launched twice a day at 05:00 and 11:00 UTC during PS85 (39 radiosondes over the 18 days) and 07:00 and 11:00 UTC during PS96 (70 radiosondes over the 38 days). Radiosondes of the type Vaisala RS92 (Vaisala, 2013) were used. The measurement uncertainty for wind is specified as 0.15 m s^{-1} for speed and 2° for direction. For the intercomparison of lidar wind profiles with the radiosonde profiles additional aspects to instrumental errors have to be considered. As shown below, the vertical range of the lidar is generally limited to the height of the ABL of a few hundred metres. When the ship is cruising, the radiosondes are launched close to the ship's superstructure and are affected by the turbulent wake of the ship. The radiosonde also needs time to accelerate to the ambient wind speed after launch, and exhibits strong pendulum motions during this phase. This results in a strong noise in the raw wind data, and a low-pass filter is applied, resulting in a reduced vertical resolution (estimated as about 200 m by Päsche et al., 2015). As documented by Achert et al. (2015) for the RV *Oden*, the ship's superstructure modifies the mean flow depending on flow direction. The largest effect occurs for relative wind along the ship's axis. For these conditions, the disturbance decreases with height and is estimated as smaller than 2 % for horizontal wind speeds at altitudes above 75 m. For a flow that is perpendicular to the ship, this effect also reduces to 2 % below 75 m. A study of Berry et al. (2001) for RV *Polarstern* shows that the largest flow distortion for the ship orientated into the wind occurs as wind decreases up to 30 % in the lee of the main superstructure in the lowest 50 m (where the radiosonde is launched).

2.3 Analysis of the lidar data

The wind analysis consists of different steps. First we look at the influence and correction of the ship's motions. In the second part we describe our data processing method and computation of horizontal winds. In the third part we discuss our choice of the SNR threshold.

2.3.1 Ship's motion correction

The main difficulty in receiving reliable wind data results from the movements of the ship. The ship's velocity and orientation and their changes influence the directions of the lidar's outgoing and incoming rays. Therefore the ship's velocity and orientation angles are the two main factors for the correction of the measured data. During both cruises PS86 and PS96, the ship was moving with more than 1 m s^{-1} about 50 % of the time. The lidar was aligned with the ship by eye as best as possible (deviations of the yaw angle between lidar and the ship are discussed later in the results section). Measured ship data from the scientific navigational platform are taken to correct each single lidar measurement by the ship's speed and roll–pitch–yaw angles. The resolution of these data is 1 Hz. The correction for the ship's roll and pitch movements can be avoided by using a motion-stabilizing platform (Achtert et al., 2015). We had no such platform, but additionally to the ship's 1 Hz navigation data, we also recorded roll and pitch movements at high-frequency (up to 400 Hz) by the AHRS that was attached to the lidar. The AHRS data were used to determine the roll and pitch offset between the AHRS (or lidar) reference system and the ship's reference system. During PS96 the averaging time of a single ray was typically 12–15 s, so that we corrected each single measurement with the mean value over the averaging time. This introduces an error whenever the ship angle, and thus the lidar angle, changes during this averaging time. In order to reduce the error, all measurements that have a standard deviation of roll or pitch angle larger than 0.5° or yaw angle larger than 2° over this averaging time were excluded from the analysis. Correcting the direction of the lidar measurement by the mean roll and pitch angle during the averaging time should already cause most of the error to average out, as it measures partly too much and partly too little wind speed. But even if this is not the case, for a data point at 1 km distance from the lidar a change in elevation from 75 to 75.5° (25 to 25.5°) causes a difference in height of 2 m (8 m) and the resulting horizontal wind speed error is less than 3.3 % (0.4 %). This is acceptable as we will later interpolate over height intervals of 50 m and only evaluate the horizontal wind in our paper. It should be noted that the correction and filtering process causes almost no loss of data. Only 6 % of the time is the standard deviation of the yaw angle over 15 s larger than 2° and the ship's movement even during ice breaking conditions generally does not result in high-frequency changes of roll and pitch (except some cases

of ramming). The important part is in fact the low-frequency change in roll and pitch (e.g. pumping water from one tank to another, changing cargo) that gets corrected. This can be seen by subtracting a 2 min running median from the roll and pitch data (Fig. 3). The remaining angles are within -0.1 and 0.1° 60–70 % of the time. Without roll and pitch correction, values amount from -2 to 2° for roll (for 95 % of the cases) and 0 to 1.5° for pitch. Therefore a set-up without any roll or pitch correction at all would still provide usable data if a high data quality is not of importance. For example, for a data point at a 1 km distance from the lidar a change in elevation from 75 to 77° (25 to 27°) causes a difference in height of 8 m (31 m) and horizontal wind speed error of less than 13 % (17 %). We also corrected for the influence of the angular velocity of roll pitch and yaw, but it was found to be negligible. For PS96 (PS85) the correction due to angular velocity was less than 0.2 m s^{-1} 99.7 % (99.9 %) of the time and never greater than 0.5 m s^{-1} .

2.3.2 Data processing

First, an SNR threshold was chosen and all data points within one ray with a worse SNR were removed. The SNR is a value given in the lidar output for each scanned Doppler velocity value. It is separate from the empirical noise defined in Sect. 2.3.3 as well as from the “noisy influence” due to other error sources like uncertainties related to the ships movement. The background noise is usually measured at least once a day and at most every hour. For this, the scanning head is turned away from the sky towards the lidar casing and measures the signal while sending no pulses out. Thus the background noise can vary with time and operating conditions and can be different for different HALO instruments. To compute the SNR, the signal strength of the background noise is subtracted from the signal strength of the measurement and afterwards divided by the signal strength of the background noise. If the signal during a measurement is lower than during the background noise scan, it can therefore cause a negative SNR. In general, more background noise scans were performed during PS85, but we did not investigate the background noise further.

Furthermore the first data points near the lidar were removed (approx. the first 30 m) as these measurements are often affected by the outgoing pulse. Then each single ray was segmented into bins of 100 m. For each bin, outliers (radial velocity $> 3 \times$ standard deviation) were removed. If less than 50 % of the data remained or if the standard deviation of the radial velocity of remaining data in the bin was greater than 3 m s^{-1} , the whole bin was removed.

To compute a vertical profile of horizontal wind speed from a complete VAD, we first divided all data points into layers of different heights. A thickness of 50 m was chosen for each layer for the radiosonde comparison, but thicknesses down to 10 m were tested as well. We used the standard assumption for VAD processing that the wind field is horizon-

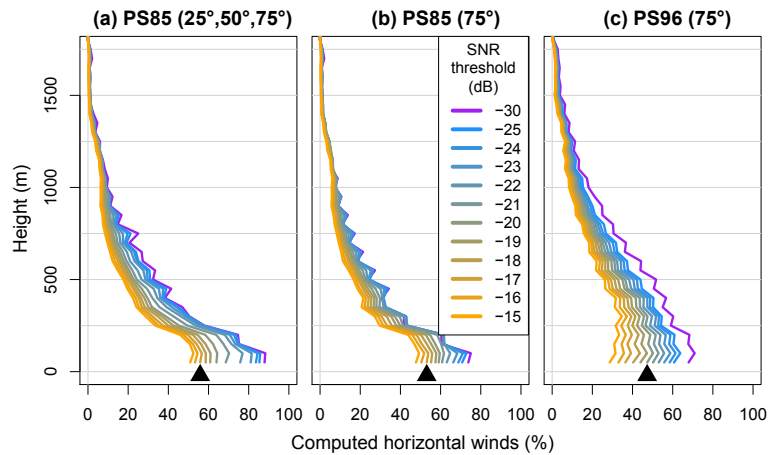


Figure 4. Percentage of wind calculations (speed and direction) from VAD scans as a function of SNR threshold at different heights during PS85 using all elevations (a), only an elevation of 75° (b) and PS96 (c). The total number of VADs for PS85/PS96 was 3552/4250. The black triangle indicates the chosen SNR threshold based on Fig. 5. For the height between 0 and 1750 m this chosen threshold results in 15 % (PS85, all elevations), 14 % (PS85, only 75°) or 21 % (PS96) of computed horizontal winds.

tally homogenous in each layer. The general approach for the processing of VAD scans is the calculation of the 3-D wind by finding the solution to a system of equations. There are two common perspectives on their definition. The first perspective operates in the (local) Cartesian coordinate system (east, north, up), in which wind is described by the components (u, v, w) and the direction of the lidar beam (normalized radius vector (x_L, y_L, z_L)). Each measured Doppler velocity d (negative if wind is blowing towards the lidar) satisfies the following linear equation:

$$d = x_L \cdot u + y_L \cdot v + z_L \cdot w. \tag{1}$$

The second perspective describes wind with horizontal wind speed and direction and the vertical component ($v_h = \sqrt{u^2 + v^2}$ horizontal wind speed, ϕ_h wind direction, w). The Doppler velocity is then a function of the scanning directions in polar coordinates ($\phi =$ azimuth, $\theta =$ elevation).

$$d = \cos(\phi - \phi_h - \pi) \cdot v_h \cdot \cos(\theta) + \sin(\theta) \cdot w \tag{2}$$

As Eq. (1) can be transformed into Eq. (2), they are equivalent (see Appendix). Assuming that the lidar remains stationary and has a fixed elevation angle θ (which is not the case in our set-up), the equation further simplifies to

$$\frac{d}{c_1} = \cos(\phi - \phi_h - \pi) \cdot v_h + w \cdot c_2, \tag{3}$$

with the constants $c_1 = \cos(\theta)$ and $c_2 = \tan(\theta)$. Wind speed and direction can then be determined by a cosine fit for all available scan directions. Although the Eqs. (2) and (3) are more intuitive, and our lidar software already uses the parameters elevation and azimuth, we found it is easier to work in a Cartesian coordinate system to apply corrections and thus choose Eq. (1). Since we have eight rays per VAD (and more

than one measurement per ray in each layer), we get a system of linear equations. Given a measured set of Doppler velocities d_i ($i = 1, \dots, n$) in directions (x_i, y_i, z_i) (east, north, up), the wind speed (u, v, w) can be calculated by solving the overdetermined system:

$$\begin{pmatrix} x_1 & y_1 & z_1 \\ x_2 & y_2 & z_2 \\ \dots & \dots & \dots \\ x_n & y_n & z_n \end{pmatrix} \times \begin{pmatrix} u \\ v \\ w \end{pmatrix} = \begin{pmatrix} d_1 \\ d_2 \\ \dots \\ d_n \end{pmatrix} \tag{4}$$

using the least squares method. To ensure the quality of the data we added the condition that at least six out of eight azimuth angles had data (that was not removed); thus at least measurements in a sector of 270° were available.

As the system of equations is only solved approximately for a given solution (u^*, v^*, w^*) , we can define a measure for the goodness of the fit. Päschke et al. (2015) define the coefficient of determination. We define the fit deviation in our paper as follows:

$$\left\| \begin{pmatrix} x_1 & y_1 & z_1 \\ x_2 & y_2 & z_2 \\ \dots & \dots & \dots \\ x_n & y_n & z_n \end{pmatrix} \times \begin{pmatrix} u^* \\ v^* \\ w^* \end{pmatrix} - \begin{pmatrix} d_1 \\ d_2 \\ \dots \\ d_n \end{pmatrix} \right\|_2. \tag{5}$$

For the purpose of comparing the fit deviation, only scans with the same elevation should be used. It should also be noted that measuring a non-homogenous or non-stationary wind field would result in a larger fit deviation value.

In Fig. 4 we show the amount of computed wind speed and direction data from VAD scans for different SNR thresholds. The increase in computed data stagnates around -30 dB. A further decrease in the SNR threshold only adds data that are thrown out again by the 100 m bin method or for other reasons. One can also see the zig-zag artefact that is produced by

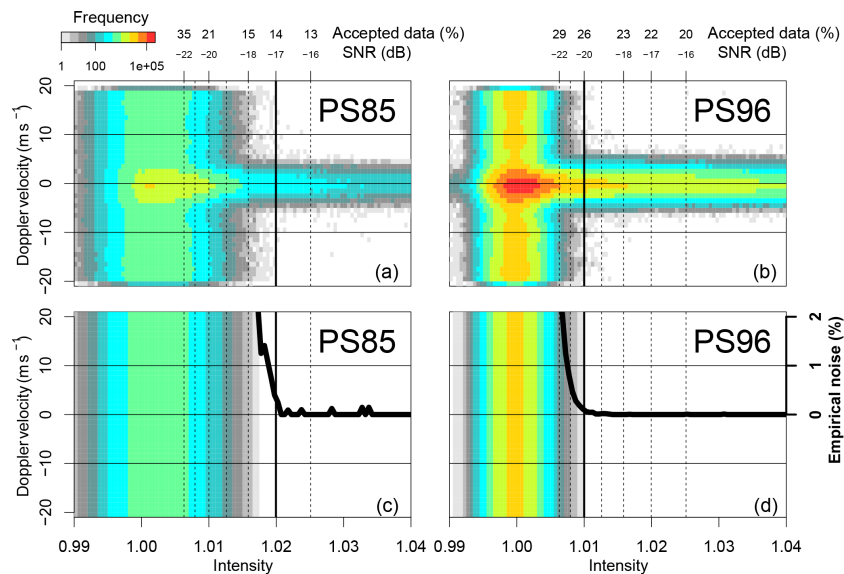


Figure 5. (a, b) Frequency of Doppler velocities of VAD scans with 75° elevation depending on the intensity/SNR and for PS85 (a, c) and PS96 (b, d). Bottom row: empirical noise computed as the mean for points above 10 m s^{-1} or below -10 m s^{-1} . The solid black line shows the ratio of empirical noise and all measured data (a, b) at each intensity/SNR. On the top axis it is also noted how much data would be accepted if the respective (minimal) SNR was chosen.

this 100 m bin combined with computing winds every 50 m. It is more dominant for PS96 as the measurement was taken every 3 m, while the measurements for PS85 were taken every 18 m. The benefit of using additional scans with 25 and 50° elevation for PS85 can be seen for the lowest 750 m if a higher SNR threshold is chosen. The choice of the SNR threshold for this paper is explained in the next section.

2.3.3 Choice of signal-to-noise ratio thresholds

SNR-based thresholds for the separation between reliable and unreliable data points are a common technique for lidar data processing (Päschke et al., 2015; Pearson et al., 2009; Frehlich and Yadlowsky, 1994; Barlow et al., 2011). This value can vary depending on the instrument-specific performance (detector noise) and the variability of atmospheric conditions within the measured volume. The recommendation of the manufacturer for the lidar is -18.2 dB . However, Päschke et al. (2015) showed that this value is rather conservative and reduces the amount of data by up to 40 % (between -20 and -18.2 dB). Hirsikko et al. (2014) use a threshold of -21 dB and state that -25 dB could still be suitable for horizontal wind measurements. Pearson et al. (2009) experimentally find an SNR threshold for reliable data of -23 dB . The potential SNR threshold was already considered during our measurements by adjusting the telescope focal length of the lidar and the integration time (following the recommendations Hirsikko et al., 2014). This is necessary during the measurements, since raw data on single pulses were not stored and thus no post-processing is possible. Figure 4 shows the sensitivity of available data for PS85 and

PS96 on the SNR threshold. We find a similar reduction to Päschke et al. (2015). A rule of thumb for our measurements seems to be that increasing the SNR threshold by 1 dB results in a (relative) loss of 5–10 % of the data. Additionally, due to the different averaging times for each ray during PS85 and PS96 (1.5 vs. 12–15 s), the PS96 data allow for a lower SNR threshold compared to the PS85 data, because averaging over a longer period given the same SNR results in better data. Thus, it makes sense to choose a less strict SNR threshold for the PS96 data set to make both data sets more comparable. Päschke et al. (2015) checked the measured wind speed of vertical staves. Knowing that vertical velocities are close to zero, Päschke et al. (2015) could evaluate the influence of noise from vertical staves for quiescent atmospheric conditions. As we did not have a stabilizing platform, the evaluation of the vertical staves is not possible because of the influence of horizontal wind on the signal. To circumnavigate this problem, we followed a similar approach and evaluated the Doppler velocity from all individual rays for VAD scans with an elevation of 75° (only the first data points near the lidar were removed; see subsection data processing). Since the Doppler velocity is less than 26 % at this elevation due to horizontal wind speed, the range of realistic Doppler velocities should be $\pm 10 \text{ m s}^{-1}$. Data points outside this range can be regarded as wrong (or empirical noise). This condition is used to find an SNR threshold in a three-step procedure. First, we look at the overall frequency distribution of measured Doppler velocities (Fig. 5, top). We assume that the data mainly consist of two parts: the empirical noise (homogenous along all wind speeds; top to bottom) and the wind

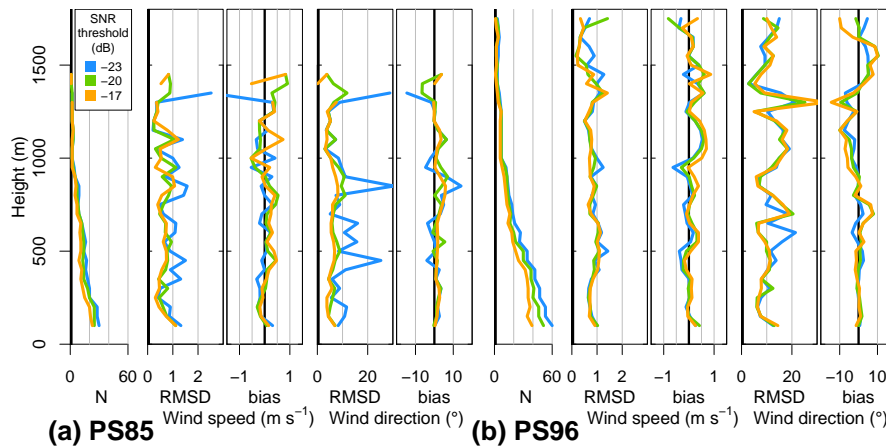


Figure 6. RMSD, bias and number of used radio soundings (N) by height of wind speed and direction for PS85 (a) and PS96 (b). Different colours show different SNR thresholds (-23 blue, -20 dB green, -17 dB orange). Only scans with an elevation of 75° were used.

Table 2. Statistics for all available lidar data compared to radio soundings. M indicates the number of used radio soundings. N indicates the number of compared measurements (N is lower for the wind direction because up to six cases with wind speed $< 0.5 \text{ m s}^{-1}$ are removed). PS85 computed for a -17 dB SNR threshold with only 75° elevation scans (first column, as shown in Fig. 6) and with all $25, 50$ and 75° (second column). PS96 was computed for -20 dB SNR threshold with the default case (standard deviation of yaw angle below 2° for each ray; third column, as shown in Fig. 6) and a stricter case (standard deviation of yaw angle below 0.5° for each ray; fourth column). aR^2 is the correlation coefficient for angular variables.

			Wind speed in m s^{-1}			Wind direction in degrees		
	M	N	RMSD	Bias	R^2	RMSD	Bias	aR^2
PS85 (VAD with 75°)	28	216	0.7	0.1	0.95	6	2	0.99
PS85 ($25, 50, 75^\circ$)	28	226	0.7	-0.1	0.95	6	-3	0.99
PS96 (2° yaw-sd)	58	574	0.8	0.1	0.95	11	0	0.96
PS96 (0.5° yaw-sd)	49	502	0.8	0.0	0.96	12	0	0.95

signal (relatively homogenous along the signal intensity or SNR; left to right). Signal intensity is defined as $\text{SNR}+1$. All points above 10 m s^{-1} or below -10 m s^{-1} are taken to construct an empirical noise distribution as a function of intensity using the mean value (Fig. 5, bottom). In the second step, we take the ratio of the empirical noise and the mean of the measured Doppler velocities for each intensity, which results in an empirical noise fraction (plotted as solid line in Fig. 5, bottom). The empirical noise fraction is close to zero for high intensities and starts to increase rapidly at different SNR values for both data sets. We choose an SNR threshold (step three) of -17 dB for PS85 and -20 dB for PS96. This empirical SNR threshold results in about $14\%/26\%$ of usable raw data for PS85/96. Comparing this to the resulting VAD percentages $14\%/21\%$ (Fig. 4), it should be noted that the decrease for PS96 comes mostly from the restriction $\text{sd}(\text{yaw}) < 2^\circ$ and $\text{sd}(\text{roll/pitch}) < 0.5^\circ$. Without this condition, the computed VAD percentage is 25% .

3 Results

A verification of the lidar wind data is presented in the following by comparisons with radiosondes and the ship measurements. For the statistics of wind direction, the absolute values of the differences are adjusted to be smaller than 180° to avoid the discontinuity in northerly directions (e.g. a difference of 270° becomes -90°). For the correlation of wind direction we used the correlation coefficient for angular variables (Jammalamadaka and Sarma, 1988). Radiosonde data were interpolated linearly with height to match the lidar data. Lidar wind speed and direction were first computed for every VAD and then averaged over a 20 min interval centred around the launch time (plus 100 s) of the radiosonde (100 s after the start the radiosonde is at a height of around 500 m). We excluded all data points with wind speed $< 0.5 \text{ m s}^{-1}$ for the statistics of wind direction, but this condition was only met during PS96 and only for up to six data points at different heights and times. Figure 6 shows the calculated root mean square deviation (RMSD) and bias by height for different SNR thresholds. While -23 dB leads to some larger dif-

Table 3. Statistics as in Table 2 but showing the range of the statistic variables for different computations. These include all possible combinations of the following two (default marked with *): (1) the thickness of layers and thus the interpolation in height of lidar data [10, 20, 30, 40, 50* m] and (2) the time range of used lidar measurements around the radio sounding measurement (100 s after start) [± 5 , 10*, 15, 30 min].

			Wind speed in m s^{-1}			Wind direction in degrees		
	<i>M</i>	<i>N</i>	RMSD	Bias	R^2	RMSD	Bias	aR^2
PS85 (VAD with 75°)	27–28	192–489	0.7	0.1–0.1	0.95–0.96	5–6	1–2	0.99
PS85 (25, 50, 75°)	28	207–508	0.6–0.7	–0.1–0.0	0.95–0.96	6	–3	0.99
PS96 (2° yaw-sd)	39–60	369–1391	0.7–0.8	0.0–0.1	0.95–0.96	11–14	0–1	0.96–0.97
PS96 (0.5° yaw-sd)	32–51	316–1226	0.7–0.8	0.0–0.1	0.96–0.97	12–15	0–1	0.95–0.97

Table 4. Statistics for lidar data (at approx. 50–75 m) compared to the ship anemometer (at 39 m). *N* indicates the number of comparisons (for the wind direction, one case with wind speed $< 0.5 \text{ m s}^{-1}$ was removed). *aR* is the correlation coefficient for angular variables.

	<i>N</i>	Wind speed in m s^{-1}			Wind direction in degrees		
		RMSD	Bias	R^2	RMSD	Bias	aR^2
PS85 (VAD with 75°)	1886	1.1	0.5	0.78	14	9	0.96
PS85 (25, 50, 75°)	1985	0.6	0.0	0.88	8	2	0.98
PS96	2010	0.9	0.0	0.93	12	0	0.95

ferences, particularly for PS85, our empirical thresholds of -20 and -17 dB are found to be reasonable. Furthermore, a systematic dependence on height is not present. We also check for a height dependence of the correlation (not shown), but there was none present. At heights above 1000 m the sample size is relatively small and differences between different SNR thresholds are not robust.

The overall statistics of the radiosonde comparisons are shown in Table 2. Although our data set is smaller than that of Achtert et al. (2015), we find similar results (RMSD for wind speed around 1 m s^{-1} and wind direction around 10°). The biases for the wind speed and direction are very small. When applying a stricter condition for the allowed standard deviation of yaw angle during the measuring and averaging time (last row in Table 2), a clear improvement in the data quality is not seen.

In order to quantify the impact of changes in our standard data processing, the effects of changing the layer thickness and changing the averaging time around the radiosonde launch were investigated. Table 3 summarizes the ranges of the effects RMSD, bias and R^2 . None of these changes had any relevant influence. We also computed the 95 % confidence interval bounds for the biases and found them to be 0.1 m s^{-1} and 1° higher or lower than the biases given in Tables 2 and 3.

As mentioned above, our results are similar to Achtert et al. (2015), who used a motion-stabilized platform and found mean bias for wind speed and direction of 0.3 m s^{-1} and 2° , and a mean standard deviation of 1.1 m s^{-1} and 12° for wind speed and direction respectively. Since the lidar was aligned with the ship's axis only by eye (see Sect. 2), this might

cause a yaw offset. We tried to estimate this yaw offset by checking the correlation of the roll and pitch 1 Hz data from the AHRS (or lidar) and the ship's navigation system. By assuming a yaw offset and correcting the roll and pitch angles, we determined the peak of the correlation. As a result, we found lidar yaw offsets of around -0.5° for PS85 and $+1^\circ$ for PS96 which are in the range of the observed bias. It should be mentioned that the first evaluations yielded a bias of 5 to 7° in wind direction compared to the radio soundings. During maintenance of the lidar after the cruises a misalignment of the lidar scanning direction by the manufacturer was discovered (offset of 5.32° in azimuth). This correction was applied to the present evaluations.

In a second analysis we compared the winds measured on the crow's nest of the ship (König-Langlo, 2014b, 2016b). There are two anemometers (2-D-sonic anemometers, one at each side, König-Langlo et al., 2006) mounted at a height of around 39 m above sea level. The first usable data points of the lidar measurements are at approximately 50 m height. Comparing the wind direction measured by the lidar in 50 m with wind direction in 60 to 200 m, we found an overall linear increase (decrease) of wind direction with height during PS85 (PS96). Assuming this change in wind direction is also present between the 39 m anemometer and the lidar data (approx. 50–75 m), this could lead to a slight positive (negative) bias during PS85 (PS96) of about 1° . An overview is shown in Figs. 7 and 8 and the statistics computed for this comparison are shown in Table 4.

Overall, lidar and ship (anemometer) measurements agree well. However, the anemometers are also disturbed by the

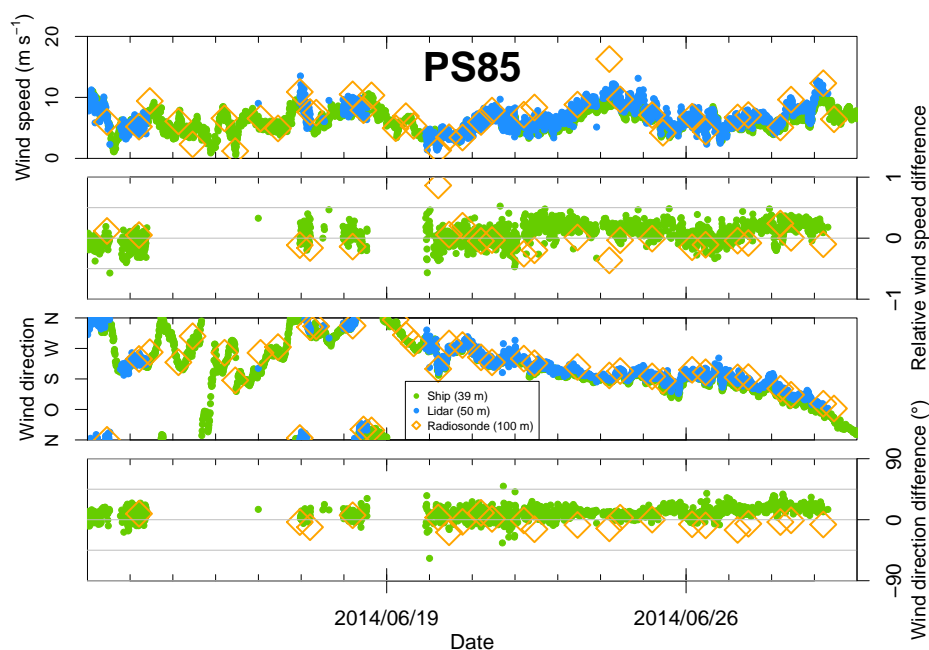


Figure 7. Comparison of wind speed and wind direction between lidar at 50 m height (blue) and ship anemometer (green) for PS85. Radiosonde winds at 100 m are marked (orange diamond) for reference. The (relative) difference is computed as lidar minus anemometer (divided by anemometer) or radiosonde (divided by radiosonde). Only scans with an elevation of 75° were used.

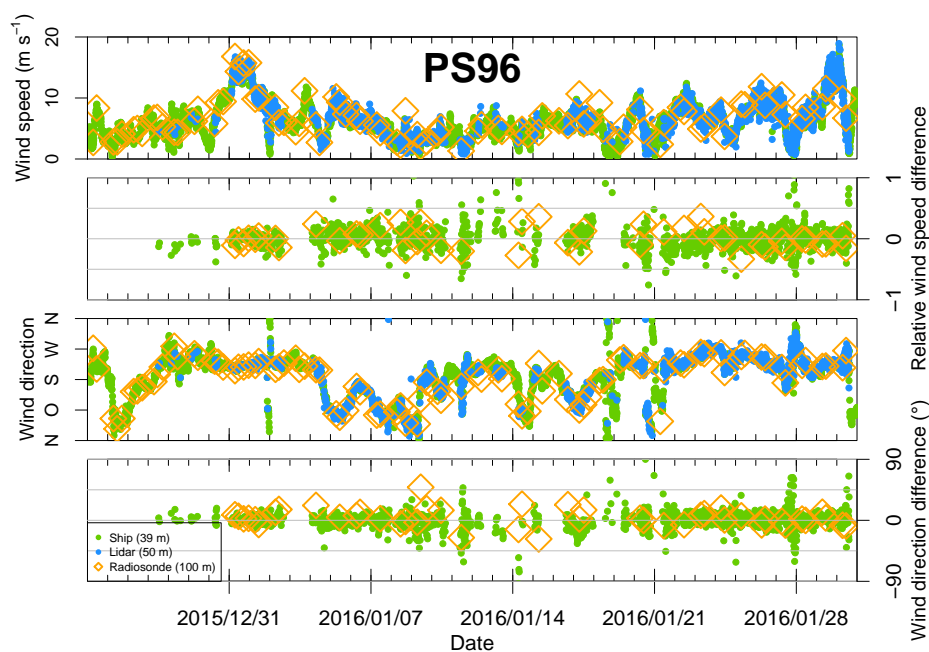


Figure 8. As Fig. 7 but for PS96 (Antarctic).

ship’s superstructure depending on the wind direction (see Sect. 2).

4 Case studies

In the following, we present two case studies. The first one focuses on the choice of the SNR threshold and the second one underlines the added value of lidar measurements com-

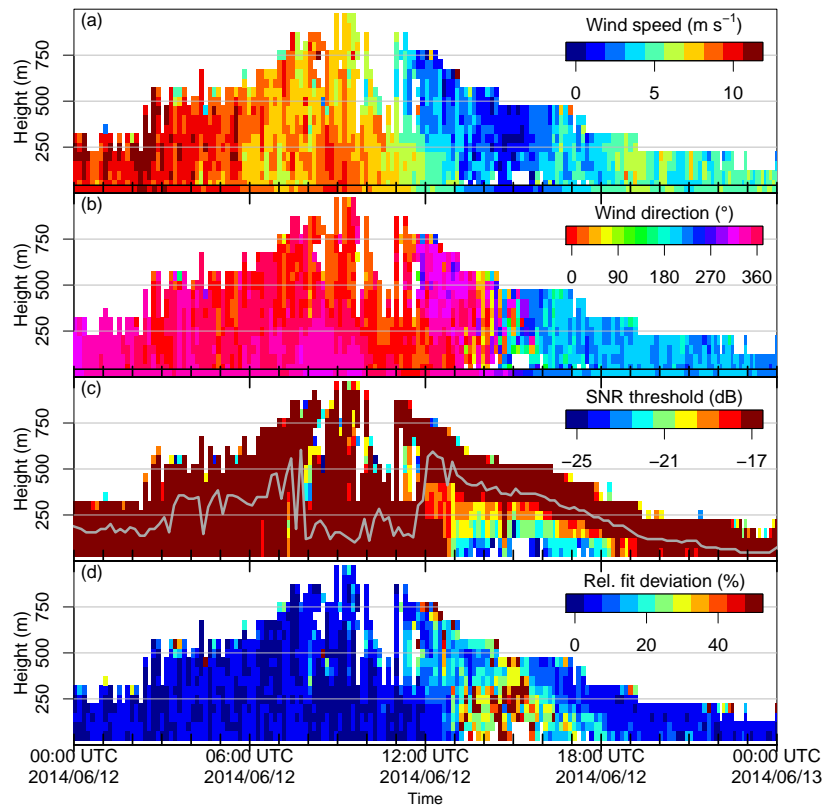


Figure 9. Lidar wind speed (a) and direction (b) for the -25 dB SNR threshold for the 12 June 2014 (location see PS85 in Fig. 1). Colours below the black line (40 m) show the wind measurements of RV *Polarstern* (anemometer). The plot (c) presents the SNR thresholds that would allow for a wind calculation. The grey line is the cloud base from ceilometer measurements of RV *Polarstern*. The relative fit deviation (fit deviation divided by wind speed) is shown in (d). Values exceeding the upper limit in (a) and (d) are included in the highest colour bar bin. Only scans with a 75° elevation were used.

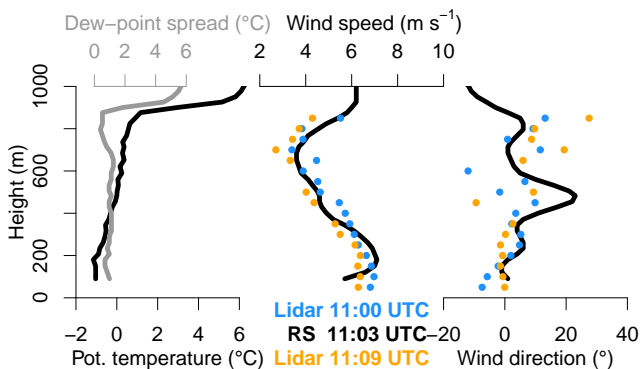


Figure 10. Vertical profiles of potential temperature, dew-point spread, wind speed and direction of radiosondes vs. lidar wind speed and direction for around 11:00 UTC on 12 June 2016. A SNR threshold of -23 dB and elevations of 25, 50 and 75° were used.

pared to the standard ship anemometer and radio sounding data.

4.1 PS85 – Arctic (12 June 2014)

The beginning of 12 June 2014 starts with wind speeds around 8.5 m s^{-1} and a N–NW wind (Fig. 9). By midday, the wind decreases to approx. 2 m s^{-1} and the direction changes almost by 180° to S–SW. Weather charts for this day show that *Polarstern* was navigating through a synoptic high-pressure ridge, which causes the measured wind changes.

The radiosonde wind profile at 11:03 UTC agrees well with the lidar wind profiles at 11:00 and 11:09 UTC (Fig. 10), and the lidar data also agree with the ship's wind measurements (Fig. 9). The potential temperature profile shows an almost neutral stratification with high humidity topped by a strong inversion at 900 m. The plot for the SNR (Fig. 9c) shows that with the conservative SNR threshold determined by the method presented in this study (-17 dB for PS85) the wind speed decreases in the afternoon would only be partially detected. However, the decrease below 250 m seems to be highly realistic in comparison with the ship measurements. Extending the SNR threshold to -20 or -23 dB yields reasonable results overall, but also adds some outliers particularly at the top height of the measurements. The pre-

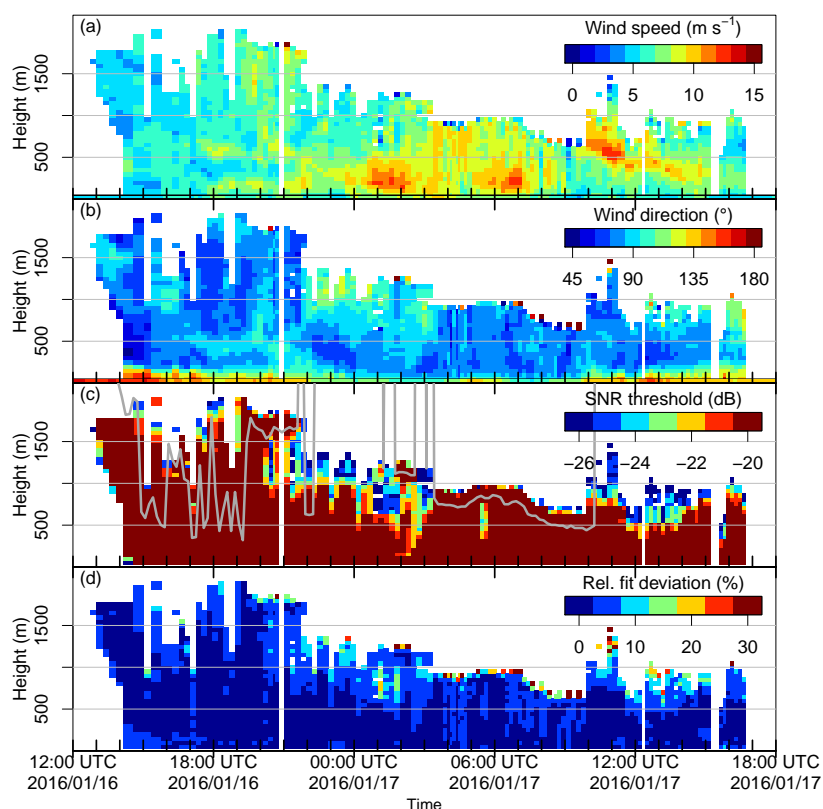


Figure 11. As Fig. 9 but for 16 and 17 January 2016 (Antarctic, PS96) and with a -26 dB SNR threshold.

sented method for determining a conservative SNR threshold seems to distinguish between reliable and unreliable data well. However, for specific cases it does make sense to manually check whether the limit can be extended to gain reliable data. The fit deviation (Fig. 9d) can help with this decision, but note that the high relative fit deviation in the afternoon stems mostly from the low wind speeds. Note that the height difference between the lidar and ceilometer from 08:00 to 12:00 UTC is likely due to a thin layer of low clouds that the lidar could partially penetrate.

4.2 PS96 – Antarctic 16–17 January 2016

The second case study is located in the Antarctic during PS96 (Fig. 11). It is chosen because it presents a stable boundary layer (SBL) with low-level jets (LLJs). The first LLJ was measured just after midnight on the 17 January 2016 between 00:30 and 02:30 UTC, and a second LLJ a few hours later between 05:30 and 07:30 UTC, and the third LLJ between 10:00 and 11:30 UTC (Fig. 11a). The LLJ wind speeds reached a maximum of up to 14 m s^{-1} at a height of 200 m (Fig. 11a). Three radio soundings are available for 16 January 17:00 UTC, and 17 January at 07:00 and 12:00 UTC. Only the profile at 06:52 UTC on 17 January captured one of the LLJs (Fig. 12). The radiosonde profile agrees well with

the lidar winds. The LLJ is located at the top of a surface inversion and is associated with a strong directional shear in the lowest 200 m. It has to be noted that the ship was orientated perpendicular to the wind for this radiosonde launch, so that the ship's influence on the radiosonde winds was minimized for this LLJ situation. The short duration and fast developments of the LLJs illustrate the benefit of vertical wind profiles with high temporal resolution. The dynamics of the LLJs were not studied in detail. They occurred during the passage of a synoptic front, when the ship operated in a polynya in the lee of a huge iceberg (A23A, size about $60 \text{ km} \times 80 \text{ km}$). Baroclinicity is therefore a likely reason for the LLJs. While LLJs caused by inertial oscillations are frequent in the Weddell Sea during winter (Andreas et al., 2000), the observed jets during PS96 are comparable to the situation of the summertime Arctic Ocean, where Jakobson et al. (2013) mostly find baroclinic jets associated with transient cyclones.

5 Conclusions

We presented a verification of wind speed profiles measured by a wind lidar without a stabilizing platform during two cruises of the research vessel *Polarstern* in the Arctic and Antarctic. The ship's motions and orientation were measured by the ship's navigation system and by a high-frequency at-

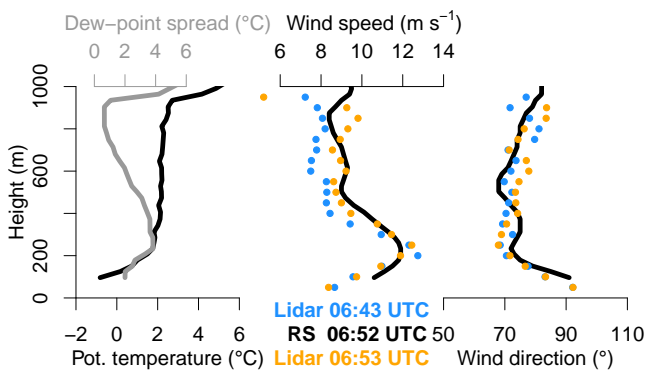


Figure 12. As Fig. 10 but for the LLJ around 07:00 UTC on 17 January 2016 (PS96). A SNR threshold of -26 dB was used.

titude heading reference system. This is the first time that a wind lidar was operated on an icebreaker in the Antarctic. A processing chain including quality control tests with a new empirical SNR threshold method and an error quantification is presented. The wind calculation is generally based on VAD scans with eight directions (rays) at an elevation angle of 75° (an elevation of 85° was discarded after a short test period), thus there is a high oversampling which allows for additional quality tests. Wind retrievals from scans at multiple elevation angles (25, 50 and 75°) slightly improve the quality of the wind profile but take more time. The low aerosol concentrations in polar regions result in a low backscatter. As a strategy for optimizing the backscatter signal for these conditions, the adjustment of the telescope focal length of the lidar and the averaging time is useful. We present a processing chain for the data, which includes a quality control for each ray and a method for deriving an empirical SNR threshold. This threshold can be calculated for individual measurement set-ups (e.g. different number of rays, averaging time), and robust thresholds of -17 and -20 dB are found for the Arctic and Antarctic cruises respectively. Due to the oversampling, an error estimation of the lidar winds can be made, which can be used as additional quality criteria. The lidar wind profiles were compared with the routine meteorological measurements of the ship and radiosonde data. Overall, the radiosonde comparisons yield similar results to those found in Achtert et al. (2015) using

as motion-stabilized lidar. The wind speed bias is very small (0.1 m s^{-1}) for our standard data processing and the RMSD is about 1 m s^{-1} . For wind direction, the RMSD is about 10° and the bias is about 1° , which is comparable to other studies. Overall the results of the post-processing of non-motion-stabilized lidar data achieve comparably high quality to the motion-stabilized lidar study of Achtert et al. (2015). As our study focuses only on horizontal winds it should be noted that the influence on vertical wind and turbulence measurements is higher and was not evaluated. The need for a motion-stabilized lidar for those measurements could be very important. The comparison with the routine wind measurements of the ship at 40 m height yields a larger data set and a similar bias and RMSD. The choice of a longer averaging time is preferred as it allows the SNR threshold to be reduced and thus increases the amount of data. For longer averaging times the influence of the ship's movement can be higher, but this effect is small in our case because the ship operated mainly in sea ice where wave heights are relatively small. It has also to be considered that the wind field around the ship is influenced by the ship's superstructure, particularly if the ship is orientated into the wind. As this often occurs for radiosonde launches during the ship cruise, the lowest 50 m of the radiosonde wind profile should not be used for these situations. Turning the ship perpendicular to the wind is desirable. The two case studies show that for special situations a flexible change in the SNR threshold can be beneficial, and that ABL phenomena like short-lived LLJs are generally not captured by the routine radio soundings. The lidar with a high temporal resolution of 10–15 min can detect these phenomena and would be ideally combined with a temperature profiler with a similar resolution. Alternatively, the lidar measurements can guide dedicated radiosonde launches during future campaigns, since, for example, LLJs can be detected in real-time with the lidar. For conditions with low backscatter due to the low aerosol concentration as it is typical for the polar regions, the possibility of optimizing the averaging time of the lidar would be the storage of the raw data (spectra) for post-processing.

Data availability. Data are available upon request to the corresponding author (zentek@uni-trier.de).

Appendix A

Given measured Doppler velocities d (negative if wind is blowing towards the lidar) in normalized directions (x, y, z) (east, north, up) and the wind speed (u, v, w) , we have the following equation:

$$d = x \cdot u + y \cdot v + z \cdot w. \tag{A1}$$

By transforming the wind (u, v, w) to $(v_h = \sqrt{u^2 + v^2}$ horizontal wind speed, ϕ_h wind direction, $w)$ with $v_h = \phi_h = 0$ if $u = v = 0$ we get

$$d = x \cdot \left(\cos\left(-\phi_h - \frac{\pi}{2}\right) \cdot v_h \right) + y \cdot \left(\sin\left(-\phi_h - \frac{\pi}{2}\right) \cdot v_h \right) + z \cdot w. \tag{A2}$$

By transforming the direction (x, y, z) to $(\theta = \text{elevation angle, } \phi = \text{azimuth angle starting north and turning clockwise})$ with $\phi = 0$ if $\theta = \pm 90^\circ = \pm \frac{\pi}{2}$ we get

$$d = \left(\cos\left(-\phi + \frac{\pi}{2}\right) \cdot \cos(\theta) \right) \cdot \left(\cos\left(-\phi_h - \frac{\pi}{2}\right) \cdot v_h \right) + \left(\sin\left(-\phi + \frac{\pi}{2}\right) \cdot \cos(\theta) \right) \cdot \left(\sin\left(-\phi_h - \frac{\pi}{2}\right) \cdot v_h \right) + \sin(\theta) \cdot w. \tag{A3}$$

By simplifying this, we get

$$d = \left(\cos\left(-\phi + \frac{\pi}{2}\right) \cdot \cos\left(-\phi_h - \frac{\pi}{2}\right) + \sin\left(-\phi + \frac{\pi}{2}\right) \cdot \sin\left(-\phi_h - \frac{\pi}{2}\right) \right) \cdot v_h \cdot \cos(\theta) + \sin(\theta) \cdot w. \tag{A4}$$

Using the trigonometric formula $\cos(a - b) = \cos(a) \cdot \cos(b) + \sin(a) \cdot \sin(b)$ we get

$$d = \left(\cos\left(-\phi + \frac{\pi}{2} + \phi_h + \frac{\pi}{2}\right) \right) \cdot v_h \cdot \cos(\theta) + \sin(\theta) \cdot w. \tag{A5}$$

By simplifying this, we get

$$d = \cos(\phi - \phi_h - \pi) \cdot v_h \cdot \cos(\theta) + \sin(\theta) \cdot w. \tag{A6}$$

Author contributions. RZ carried out the investigation (measurements on PS96), data curation, methodology, formal analysis, verification, software, visualization and writing of the original draft. SK carried out the investigation (measurements on PS85), verification, a review of the writing and editing. GH carried out the investigation (measurements on PS96), conceptualization, methodology, a review of the writing, editing, supervision, project administration and funding acquisition.

Competing interests. The authors declare that they have no conflict of interest.

Acknowledgements. The measurements were performed during the two *Polarstern* cruises PS85 and PS96 funded by the Alfred Wegener Institute under *Polarstern* grants AWI_PS85_01 and AWI_PS96_03. The research was funded by the Federal Ministry of Education and Research (Bundesministerium für Bildung und Forschung–BMBF) as part of the project “Laptev-Sea Transdrift” under grant 03G0833D and by the SPP 1158 “Antarctic research” of the DFG (Deutsche Forschungsgemeinschaft) under grant HE 2740/19.

From all the software that was used we would like to highlight R, RStudio and the R packages doParallel and data.table. We thank our colleague Clemens Drüe for many useful discussions and our colleague Uwe Baltes for help with the cruise preparations.

The publication was funded by the Open Access Fund of Universität Trier and the German Research Foundation (DFG) within the Open Access Publishing funding programme.

Edited by: Ulla Wandinger

Reviewed by: two anonymous referees

References

- Achtert, P., Brooks, I. M., Brooks, B. J., Moat, B. I., Prytherch, J., Persson, P. O. G., and Tjernström, M.: Measurement of wind profiles by motion-stabilised ship-borne Doppler lidar, *Atmos. Meas. Tech.*, 8, 4993–5007, <https://doi.org/10.5194/amt-8-4993-2015>, 2015.
- Andreas, E. L., Claffy, K. J., and Makshtas, A. P.: Low-Level Atmospheric Jets And Inversions Over The Western Weddell Sea, *Bound.-Layer Meteorol.*, 97, 459–486, <https://doi.org/10.1023/a:1002793831076>, 2000.
- Banta, R. M., Pichugina, Y. L., and Brewer, W. A.: Turbulent Velocity-Variance Profiles in the Stable Boundary Layer Generated by a Nocturnal Low-Level Jet, *J. Atmos. Sci.*, 63, 2700–2719, <https://doi.org/10.1175/jas3776.1>, 2006.
- Barlow, J. F., Dunbar, T. M., Nemitz, E. G., Wood, C. R., Gallagher, M. W., Davies, F., O’Connor, E., and Harrison, R. M.: Boundary layer dynamics over London, UK, as observed using Doppler lidar during REPARTEE-II, *Atmos. Chem. Phys.*, 11, 2111–2125, <https://doi.org/10.5194/acp-11-2111-2011>, 2011.
- Berry, D. I., Moat, B. I., and Yelland, M. J.: Airflow distortion at instrument sites on the FS *Polarstern*, techreport, Southampton, Southampton Oceanography Centre, 36 pp. (Southampton Oceanography Centre Internal Document, 69), available at: <http://nora.nerc.ac.uk/id/eprint/502825/> (last access: 18 October 2018), 2001.
- Brooks, I. M., Tjernström, M., Persson, P. O. G., Shupe, M. D., Atkinson, R. A., Canut, G., Birch, C. E., Mauritsen, T., Sedlar, J., and Brooks, B. J.: The Turbulent Structure of the Arctic Summer Boundary Layer During The Arctic Summer Cloud-Ocean Study, *J. Geophys. Res.-Atmos.*, 122, 9685–9704, <https://doi.org/10.1002/2017jd027234>, 2017.
- Calhoun, R., Heap, R., Princevac, M., Newsom, R., Fernando, H., and Ligon, D.: Virtual Towers Using Coherent Doppler Lidar during the Joint Urban 2003 Dispersion Experiment, *J. Appl. Meteorol. Climatol.*, 45, 1116–1126, <https://doi.org/10.1175/jam2391.1>, 2006.
- Damian, T., Wieser, A., Träumner, K., Corsmeier, U., and Kottmeier, C.: Nocturnal Low-level Jet Evolution in a Broad Valley Observed by Dual Doppler Lidar, *Meteorol. Z.*, 23, 305–313, <https://doi.org/10.1127/0941-2948/2014/0543>, 2014.
- Dee, D. P., Uppala, S. M., Simmons, A. J., Berrisford, P., Poli, P., Kobayashi, S., Andrae, U., Balmaseda, M. A., Balsamo, G., Bauer, P., Bechtold, P., Beljaars, A. C. M., van de Berg, L., Bidlot, J., Bormann, N., Delsol, C., Dragani, R., Fuentes, M., Geer, A. J., Haimberger, L., Healy, S. B., Hersbach, H., Hólm, E. V., Isaksen, I., Kållberg, P., Köhler, M., Matricardi, M., McNally, A. P., Monge-Sanz, B. M., Morcrette, J.-J., Park, B.-K., Peubey, C., de Rosnay, P., Tavolato, C., Thépaut, J.-N., and Vitart, F.: The ERA-Interim reanalysis: configuration and performance of the data assimilation system, *Q. J. Roy. Meteorol. Soc.*, 137, 553–597, <https://doi.org/10.1002/qj.828>, 2011.
- Frehlich, R. G. and Yadlowsky, M. J.: Performance of Mean-Frequency Estimators for Doppler Radar and Lidar, *J. Atmos. Ocean. Technol.*, 11, 1217–1230, [https://doi.org/10.1175/1520-0426\(1994\)011<1217:pomfef>2.0.CO;2](https://doi.org/10.1175/1520-0426(1994)011<1217:pomfef>2.0.CO;2), 1994.
- Hirsikko, A., O’Connor, E. J., Komppula, M., Korhonen, K., Pfüller, A., Giannakaki, E., Wood, C. R., Bauer-Pfundstein, M., Poikonen, A., Karppinen, T., Lonka, H., Kurri, M., Heinonen, J., Moisseev, D., Asmi, E., Aaltonen, V., Nordbo, A., Rodriguez, E., Lihavainen, H., Laaksonen, A., Lehtinen, K. E. J., Laurila, T., Petäjä, T., Kulmala, M., and Viisanen, Y.: Observing wind, aerosol particles, cloud and precipitation: Finland’s new ground-based remote-sensing network, *Atmos. Meas. Tech.*, 7, 1351–1375, <https://doi.org/10.5194/amt-7-1351-2014>, 2014.
- Jakobson, L., Vihma, T., Jakobson, E., Palo, T., Männik, A., and Jaagus, J.: Low-level jet characteristics over the Arctic Ocean in spring and summer, *Atmos. Chem. Phys.*, 13, 11089–11099, <https://doi.org/10.5194/acp-13-11089-2013>, 2013.
- Jammalamadaka, S. and Sarma, Y.: A correlation coefficient for angular variables, *Statistical Theory and Data Analysis*, 2, 349 pp., North Holland, 1988.
- König-Langlo, G.: Upper air soundings during POLARSTERN cruise PS85 (ARK-XXVIII/2), <https://doi.org/10.1594/PANGAEA.844803>, 2014a.
- König-Langlo, G.: Continuous meteorological surface measurement during POLARSTERN cruise PS85 (ARK-XXVIII/2), <https://doi.org/10.1594/PANGAEA.839962>, 2014b.
- König-Langlo, G.: Upper air soundings during POLARSTERN cruise PS96 (ANT-XXXI/2 FROSN), <https://doi.org/10.1594/PANGAEA.861658>, 2016a.

- König-Langlo, G.: Continuous meteorological surface measurement during POLARSTERN cruise PS96 (ANT-XXXI/2 FROSN), <https://doi.org/10.1594/PANGAEA.861441>, 2016b.
- König-Langlo, G., Loose, B., and Bräuer, B.: 25 Years of Polarstern Meteorology, WDC-MARE Reports, 4, 1–137, <https://doi.org/10.2312/wdc-mare.2006.4>, 2006.
- Kumer, V.-M., Reuder, J., Dorninger, M., Zauner, R., and Grubišić, V.: Turbulent kinetic energy estimates from profiling wind LiDAR measurements and their potential for wind energy applications, *Renew. Energy*, 99, 898–910, <https://doi.org/10.1016/j.renene.2016.07.014>, 2016.
- Päschke, E., Leinweber, R., and Lehmann, V.: An assessment of the performance of a 1.5 μm Doppler lidar for operational vertical wind profiling based on a 1-year trial, *Atmos. Meas. Tech.*, 8, 2251–2266, <https://doi.org/10.5194/amt-8-2251-2015>, 2015.
- Pearson, G., Davies, F., and Collier, C.: An Analysis of the Performance of the UFAM Pulsed Doppler Lidar for Observing the Boundary Layer, *J. Atmos. Ocean. Technol.*, 26, 240–250, <https://doi.org/10.1175/2008jtecha1128.1>, 2009.
- Pichugina, Y. L., Banta, R. M., Brewer, W. A., Sandberg, S. P., and Hardesty, R. M.: Doppler Lidar-Based Wind-Profile Measurement System for Offshore Wind-Energy and Other Marine Boundary Layer Applications, *J. Appl. Meteorol. Climatol.*, 51, 327–349, <https://doi.org/10.1175/jamc-d-11-040.1>, 2012.
- Spren, G., Kaleschke L., and Heygster, G.: Sea ice remote sensing using AMSR-E 89-GHz channels, *J. Geophys. Res-Oceans*, <https://doi.org/10.1029/2005JC003384>, 2008.
- Tjernström, M., Leck, C., Birch, C. E., Bottenheim, J. W., Brooks, B. J., Brooks, I. M., Bäcklin, L., Chang, R. Y.-W., de Leeuw, G., Liberto, L. D., de la Rosa, S., Granath, E., Graus, M., Hansel, A., Heintzenberg, J., Held, A., Hind, A., Johnston, P., Knulst, J., Martin, M., Matrai, P. A., Mauritsen, T., Müller, M., Norris, S. J., Orellana, M. V., Orsini, D. A., Paatero, J., Persson, P. O. G., Gao, Q., Rauschenberg, C., Ristovski, Z., Sedlar, J., Shupe, M. D., Sierau, B., Sirevaag, A., Sjogren, S., Stetzer, O., Swietlicki, E., Szczodrak, M., Vaattovaara, P., Wahlberg, N., Westberg, M., and Wheeler, C. R.: The Arctic Summer Cloud Ocean Study (ASCOS): overview and experimental design, *Atmos. Chem. Phys.*, 14, 2823–2869, <https://doi.org/10.5194/acp-14-2823-2014>, 2014.
- Tucker, S. C., Senff, C. J., Weickmann, A. M., Brewer, W. A., Banta, R. M., Sandberg, S. P., Law, D. C., and Hardesty, R. M.: Doppler Lidar Estimation of Mixing Height Using Turbulence, Shear, and Aerosol Profiles, *J. Atmos. Ocean. Technol.*, 26, 673–688, <https://doi.org/10.1175/2008jtecha1157.1>, 2009.
- Vaisala: Radiosonde RS92-SGP, data sheet, available at: <https://www.vaisala.com/sites/default/files/documents/RS92SGP-Datasheet-B210358EN-F-LOW.pdf> (last access: 2 January 2018), 2013.

4.3 Publication 2

distributed under the Creative Commons Attribution 4.0 License
<https://creativecommons.org/licenses/by/4.0/>



Verification of the regional atmospheric model CCLM v5.0 with conventional data and lidar measurements in Antarctica

Rolf Zentek and Günther Heinemann

Department of Environmental Meteorology, University of Trier, Trier, Germany

Correspondence: Rolf Zentek (zentek@uni-trier.de)

Received: 17 May 2019 – Discussion started: 13 August 2019

Revised: 16 January 2020 – Accepted: 4 March 2020 – Published: 6 April 2020

Abstract. The nonhydrostatic regional climate model CCLM was used for a long-term hindcast run (2002–2016) for the Weddell Sea region with resolutions of 15 and 5 km and two different turbulence parametrizations. CCLM was nested in ERA-Interim data and used in forecast mode (suite of consecutive 30 h long simulations with 6 h spin-up). We prescribed the sea ice concentration from satellite data and used a thermodynamic sea ice model. The performance of the model was evaluated in terms of temperature and wind using data from Antarctic stations, automatic weather stations (AWSs), an operational forecast model and reanalyses data, and lidar wind profiles. For the reference run we found a warm bias for the near-surface temperature over the Antarctic Plateau. This bias was removed in the second run by adjusting the turbulence parametrization, which results in a more realistic representation of the surface inversion over the plateau but resulted in a negative bias for some coastal regions. A comparison with measurements over the sea ice of the Weddell Sea by three AWS buoys for 1 year showed small biases for temperature around ± 1 K and for wind speed of 1 m s^{-1} . Comparisons of radio soundings showed a model bias around 0 and a RMSE of 1–2 K for temperature and 3–4 m s^{-1} for wind speed. The comparison of CCLM simulations at resolutions down to 1 km with wind data from Doppler lidar measurements during December 2015 and January 2016 yielded almost no bias in wind speed and a RMSE of ca. 2 m s^{-1} . Overall CCLM shows a good representation of temperature and wind for the Weddell Sea region. Based on these encouraging results, CCLM at high resolution will be used for the investigation of the regional climate in the Antarctic and atmosphere–ice–ocean interactions processes in a forthcoming study.

1 Introduction

Regional climate models (RCMs) are a valuable tool for improving our understanding of processes and interactions of the climate system in the polar regions. These processes are, e.g. atmosphere–ice–ocean (AIO) interactions, which are particularly pronounced when sea ice formation is involved. This is associated with strong impacts on the surface energy fluxes and the atmospheric boundary layer (ABL). The added value of RCMs compared to coarser reanalysis and global climate models (GCMs) has been shown in a number of studies (e.g. Rummukainen, 2010) and is the background of the Polar-CORDEX (COordinated Regional Downscaling Experiment) initiative (Akperov et al., 2018). For the polar regions, the spatial and temporal coverage by the observational network is sparse compared to midlatitudes; therefore RCMs are the only means of providing climatological information at a high resolution with full spatial coverage (e.g. Kohnemann et al., 2017). High-resolution atmospheric simulations are also important for forcing ocean models (Haid et al., 2015) and the understanding of the surface mass balance (Souverijns et al., 2018; Gorodetskaya et al., 2014). A high resolution is also necessary to resolve topographic effects such as foehn winds, which could play a role for the instability of ice shelves (Cape et al., 2015), and katabatic winds (Ebner et al., 2014; Heinemann, 1997).

For the Antarctic, van Lipzig (2004) showed that for a sufficient consideration of topography-induced atmospheric processes a resolution of at least 15 km is necessary. The hydrostatic regional climate model RACMO (Regional Atmospheric Climate Model) was used by van Lipzig (2004) with a 14 km resolution for the period 1987–1993. The RACMO model was also used by van Wessem et al. (2015) at a high resolution of 5.5 km over the period 1979–2013 for the

Antarctic Peninsula (AP), and more detailed and more pronounced temperature and wind speed gradients compared to the ERA-Interim forcing (approx. 80 km horizontal resolution) were found, which are mostly related to the katabatic wind. However, the sea ice cover data set with 80 km resolution and the assumption that nonhydrostatic effects are small at 5 km resolution are drawbacks of that study. Foehn winds were studied by Elvidge et al. (2015) particularly for the Larsen C ice shelf using the Met Office Unified Model at 1.5 km grid size. King et al. (2017) used model data from the Antarctic Mesoscale Prediction System (AMPS) with 5 km resolution for the summer season 2010/11 to also study foehn wind effects over the Larsen C Ice Shelf. Turton et al. (2017) studied foehn effects over the Larsen C Ice Shelf in May 2011 using the nonhydrostatic polar WRF model with 1.5 and 5 km resolution and found in general better results for the higher resolution. These studies were performed with nonhydrostatic models but for rather short periods. The need for nonhydrostatic models for high-resolution regional climate simulations is outlined by Giorgi and Gutowski (2015) and Prein et al. (2015).

In the present study the regional nonhydrostatic Consortium for Small-Scale Modeling (COSMO) model in Climate Mode (COSMO-CLM; abbreviated as CCLM) is used to run simulations for the Antarctic with resolutions of ≈ 15 and ≈ 5 km for the time period from 2002 to 2016. The simulation is forced with ERA-Interim reanalysis data and is the first long-term hindcast simulation with a high-resolution nonhydrostatic regional climate model for the Weddell Sea region. The main purpose of the simulations is the study of AIO interactions in polynyas (see Ebner et al., 2014), which require a high resolution also in the sea ice data used as boundary conditions for the simulations. Thus we focus on the period since 2002, for which high-resolution sea ice data from microwave satellite sensors are available (see Sect. 2). The CCLM data are also used as atmospheric forcing for a high-resolution sea ice/ocean model (see Haid et al., 2015).

This data set of atmospheric variables is compared to conventional measurements like radio soundings (RSs) and both manned stations (MSs) and automatic weather stations (AWSs). Further, an investigation is presented concerning the usage of Doppler wind lidar measurements in polar regions for verifications of model simulations. In Sect. 2 the model and data sets used for the simulation and the verification are described, followed by a short comparison to another model and reanalyses (Sect. 3), then the results of the verification (Sect. 4), and finally the summary (Sect. 5) and conclusions (Sect. 6).

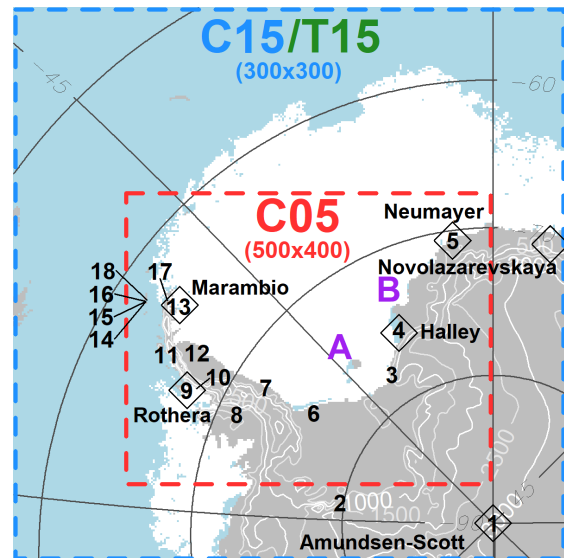


Figure 1. Overview of the C15/T15 (blue/green) and C05 (red) simulation domains, locations of six radio sounding stations (diamonds), surface/automatic weather stations (numbers), and locations of the RV *Polarstern* during our two case studies A and B (purple). Topography contours are plotted every 500 m, and sea ice concentration $> 70\%$ for the 1 June 2015 is shown in white. (Note that the T15 domain is the same as the C15 domain.)

2 Data and methods

2.1 CCLM

The CCLM is a regional nonhydrostatic model and is used as the community model for German climate research. It is a modified version of the COSMO model (version 5.0; Steppeler et al., 2003; <http://www.cosmo-model.org>, last access: 31 March 2020; archived documentation at zenodo; Zentek, 2019) used by the Climate Limited-area Modelling (CLM)-Community (Rockel et al., 2008; <http://www.clm-community.eu>, last access: 31 March 2020). Three different model setups are used for the simulations (see Table 1 and Fig. 1).

The first simulation with a resolution of ≈ 15 km (C15) is forced with ERA-Interim (Dee et al., 2011) for the time period from 2002 to 2016, and the domain covers a quarter of Antarctica centred over the Weddell Sea. The second simulation with a resolution of ≈ 5 km (C05) is nested inside the C15 domain and is only done for winter periods (April–September) in 2002–2016. The third simulation (T15) uses the same setup as C15, but the turbulence parametrization was changed, since deficits in the C15 simulations were found for the stable boundary layer. These modifications are based on the studies of Cerenzia et al. (2014), Hebbinghaus and Heinemann (2006), and Souverijns et al. (2019). In the standard version of CCLM, the diffusion coefficients for heat and momentum are restricted to the minimal value

Table 1. Overview of the different simulations. The grid size for C01 and T01 was changed for each day with a minimal (maximal) size of 200×200 (353×464).

	Simulations					
	C15	T15	C05	T05	C01	T01
Turbulence parameters changed	no	yes	no	yes	no	yes
Actual grid size (for rotated lat = 0)	13.88 km		5.55 km		1.11 km	
Grid size	300×300		400×400		$> 200 \times 200$	
Grid resolution (in rotated system)	0.125°		0.05°		0.01°	
SSO used	yes		yes		no	
Period	Jan–Dec 2002–2016		Apr–Sep 2002–2016		Case study only: Dec 2015, Jan 2016	

of $0.4 \text{ m}^2 \text{ s}^{-1}$. In the T15 simulation, these minimal diffusion coefficients were set to $0.01 \text{ m}^2 \text{ s}^{-1}$ to allow for a very stable boundary layer (SBL) over the Antarctic ice sheet during winter. Further, the standard setup of CCLM uses a parametrization of the impact of the inhomogeneity of the surface via the energy transfer from subgrid-scale eddies on the turbulent kinetic energy (TKE). Since this leads to an overestimation of the TKE in the SBL (Cerenzia et al., 2014), this parametrization was removed in the T15 runs.

All simulations have a vertical resolution of 60 levels that are terrain-following on the ground and gradually change into pressure-following coordinates around a height of 12 km with the model top being at 25 km. The runs were performed in a forecast mode, i.e. daily 30 h simulations to keep the hindcast close to reality. We used the first 6 h as spin-up in order to allow for the atmosphere to adapt to the difference between the high-resolution sea ice data from satellite and the coarse-resolution temperatures from ERA-Interim.

Over land, we use the standard land surface model of CCLM (TERRA; see archived documentation at zenodo; Zentek, 2019). The soil model has eight layers (down to 15 m) and allows for an additional snow layer on top of the soil, which varies with precipitation and sublimation. For the land ice regions, soil was replaced by snow using the parameters listed in Table 2. Over sea ice the model was adapted to polar regions by the implementation of a thermodynamic sea ice model (Schröder et al., 2011). The snow temperature profile is initialized with the forcing data, and then the snow temperatures freely evolve. The surface albedo for inland ice and ice shelves is kept constant and has no seasonal variations. The albedo of sea ice is parametrized as a function of ice thickness and temperature by a modified K ϕ ltzow scheme (K ϕ ltzow, 2007) as described in Gutjahr et al. (2016).

Further, the RTopo2 data set (Schaffer and Timmermann, 2016; Schaffer et al., 2016) is used for the topography as the default data set of CCLM did not include ice shelves. Parameters for the subgrid-scale orography (SSO; Lott and Miller, 1997) module were computed for the new data set, and the SSO module was used for both the 15 and 5 km simulation.

For sea ice data, daily sea ice concentration (SIC) is used. The data are based on AMSR-E (Advanced Microwave Scanning Radiometer – for Earth Observing System) and AMSR2 (Advanced Microwave Scanning Radiometer 2), and for data gaps SSMIS (Special Sensor Microwave Imager/Sounder) satellite measurements (Spren et al., 2008; Ezraty et al., 2007) are used. The resolution of the sea ice concentration data is 6.25 km for AMSR-E/AMSR2 but is coarser for SSMIS (12.5 km). Details of the data used are given in Table 3. Sea surface temperature (SST) data and initial surface temperature were taken from ERA-Interim. In the case of inconsistency between SST and SIC (surface temperature below the freezing temperature of -1.7°C for a SIC of 0%), the SST was set to the freezing temperature. The SIC data included some missing values, which were replaced in the following way. In a first step, missing values were filled with values from the day before and after (mean if both were available). In a second step, days for which no data were available were interpolated linearly in time (overall 35 d; maximal 9 d in succession). This still left some missing values (mostly along the coastline due to the different land masks of RTopo2 and AMSR-E/SSMIS/AMSR2). These remaining missing values are filled in a third step with an iterative procedure for each day separately using the surrounding grid points.

A fractional sea ice cover is not used in the model, thus for each grid box there is only one value of sea ice thickness, which is assumed to cover the whole grid box. Benefits of modelling a fractional sea ice cover are investigated in Gutjahr et al. (2016). As daily sea ice thickness data like PIOMAS (Zhang and Rothrock, 2003) are not available for Antarctica, we assume two different ice classes depending on the initial sea ice concentration. Grid points with a sea ice concentration of 0%–15% are set to open water. For 15%–70% a sea ice thickness of 0.1 m is assumed (see e.g. Gutjahr et al., 2016). For 70%–100% we assume a thickness of 1 m, which is a reasonable estimate for the Weddell Sea (see Kurtz and Markus, 2012). With a threshold of 70% SIC commonly used for the identification of polynyas, this choice is in accordance with previous studies (Ebner et al., 2014; Bauer et al.,

Table 2. Overview of surface parameters.

Parameter	Value
Snow heat capacity (inland ice/ice shelf)	$0.73 \times 10^6 \text{ J m}^{-3} \text{ K}^{-1}$
Snow heat conductivity (inland ice/ice shelf)	$0.30 \text{ W m}^{-1} \text{ K}^{-1}$
Albedo (inland ice/ice shelf)	0.80
Heat capacity sea ice/snow on sea ice	$1.91/0.63 \times 10^6 \text{ J m}^{-3} \text{ K}^{-1}$
Heat conductivity sea ice/snow on sea ice	$2.26/0.75 \text{ W m}^{-1} \text{ K}^{-1}$
Albedo (sea ice)	0.17 (10 cm)/0.84 (1 m)

Table 3. Overview of sea ice concentration data used in CCLM. Download for CERSAT/IFREMER at <http://cersat.ifremer.fr/data/> (last access: 31 March 2020) and for Uni Bremen at <https://seaice.uni-bremen.de/start/data-archive/> (last access: 31 March 2020).

Satellite	Provider	Time period
SSMI	CERSAT/IFREMER	1 Jan 2002 to 31 May 2002
AMSR-E	Uni Bremen	1 Jun 2002 to 4 Oct 2011
SSMI ^a	Uni Bremen	5 Oct 2011 to 23 Jul 2012
AMSR2	Uni Bremen	24 Jul 2012 to 31 Dec 2016

^a There were two data sets of SSMI data based on different sensors (F17 and F18). A comparison for the overlapping periods of 2 months (August, September) with AMSR-E (2011) and AMSR2 (2012) were compared with the F17 and F18 SSMI data. Standard deviation was computed, and it was found that F17 is closer to AMSR-E and F18 is closer to AMSR2, but overall F17 seemed to have less deviation in the area of interest. So only the F17 data were taken for October 2011–July 2012.

2013). For grid points with a sea ice thickness of 0.1 m the modified Køltzow scheme yields an albedo of 0.07, and we assume no snow cover. For a thickness of 1 m the albedo is 0.84 (for temperatures lower than -2°C) and a fixed snow layer of 10 cm snow cover (Schröder et al., 2011) is assumed.

Lastly we want to point out some differences between the present model setup and the setup of Souverijns et al. (2019), as they also used the CCLM model for simulations in the Antarctic. Souverijns et al. (2019) used CCLM with the community land model CLM (van Kampenhout et al., 2017), while we used default land surface model of CCLM with the adaptations described above. While we used daily high-resolution (6 km) sea ice data from satellites, they used coarse-resolution ERA-Interim data (80 km) for the sea ice. In addition, they used only the standard one-layer sea ice model of CCLM. They also ran CCLM in climate mode and applied spectral nudging, while we used forecast mode with a restart every day and applied forcing only at the boundaries.

2.2 AMPS and ERA

Beside the forcing data set ERA-Interim (Dee et al., 2011), the newer ERA5 reanalysis data (Hersbach et al., 2018) and data from the Antarctic Mesoscale Prediction System (AMPS; Bromwich et al., 2005; Powers et al., 2012) are used for comparisons. ERA5 reanalysis data are the new version of ERA-Interim reanalysis data. Both data sets are products

of the European Centre for Medium-Range Weather Forecasts. The AMPS data set was produced as a collaborative effort between the Mesoscale and Microscale Meteorology Laboratory of the National Center for Atmospheric Research and The Ohio State University. The horizontal/temporal resolutions are approximately 80 km (6 h)⁻¹ (ERA-Interim), 30 km h^{-1} (ERA5), and 10 km (3 h)⁻¹ (AMPS).

2.3 AWSs and surface stations

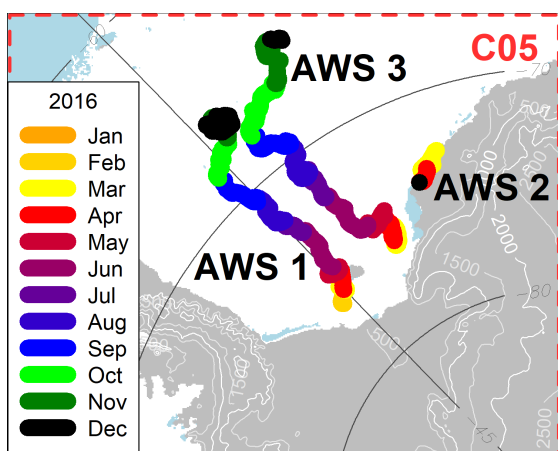
We use near-surface temperature and wind measurements from manned stations (MSs) and automatic weather stations (AWSs). The location of used MSs and AWSs are shown in Fig. 1 (numbers), and detailed information is given in Table 4. The data were collected by the national Antarctic operators and collated by the British Antarctic Survey (ftp://ftp.bas.ac.uk/src/SCAR_EGOMA, last access: 31 March 2020).

Because maintenance of AWSs is difficult for logistic reasons, they are more likely to include measurement errors. Thus we used the data from MSs whenever possible and only fell back to AWS data for regions where no MS was available. An examination of the data showed some obviously wrong data where the wind speed drops, e.g. from 15 to 0 m s^{-1} between two data records. As there were also longer periods even over days during which the data showed 0 m s^{-1} , we refrained from searching for these drop-offs with a threshold and instead removed all wind data with a wind speed of 0 m s^{-1} . This removed less than 8 % of the data for each station, except for three manned stations (Belgrano II, Esperanza, and San Martin) where up to 35 % were removed. Furthermore the wind direction values for the years 2002–2005 of the Larsen AWSs were removed as there seemed to be an offset compared to all following years.

As this MS and AWS data set lacks observations over the ocean and sea ice, we also used another data set from three AWSs (Grosfeld et al., 2016) that were placed on ice floes and covers each a time span of about 1 year. As they were placed on ice floes, these AWSs drifted through the Weddell Sea from January to December 2016. The locations are shown in Fig. 2. For this data set we only removed four outliers for which longitude and latitude were obviously wrong. Further, the last 31 data points from AWS 3 were removed as

Table 4. Information on the surface stations. The label “yes” over land indicates that the surface type of the compared model grid point is land and not water. Years give the approximate data record length in years. AWS: automatic weather station; KGI: on King George Island.

	No.	Station	Longitude	Latitude	Height (m)			Land		Years
					real	C05	C15	C05	C15	
Inland	1	Amundsen–Scott	0.00	−90.00	2835		2796		yes	15
	2	Union (AWS)	−83.27	−79.76	767		1173		yes	6
East coast	3	Belgrano II	−34.62	−77.87	256	235	388	yes	yes	14
	4	Halley	−26.22	−75.43	30	14	19	yes	yes	15
	5	Neumayer	−8.25	−70.67	50	35	36	yes	yes	14
South pen.	6	Limbert (AWS)	−59.15	−75.87	58	58	57	yes	yes	10
	7	Butler (AWS)	−60.17	−72.20	115	8	34	yes	yes	12
	8	Fossil (AWS)	−68.28	−71.32	66	182	279	yes	yes	10
Middle pen.	9	Rothera	−68.12	−67.57	32	1	7	yes		15
	10	San Martin	−67.13	−68.12	4	104	145		yes	15
	11	Vernadsky	−64.27	−65.25	11	0	0			15
	12	Larsen (AWS)	−61.47	−67.00	43	37	31	yes	yes	10
North pen.	13	Marambio	−56.72	−64.23	198	0	3			15
	14	Great Wall (KGI)	−58.97	−62.22	10	37	61	yes		14
	15	Marsh(KGI)	−58.98	−62.18	10	20	61	yes		8
	16	Bellingshausen (KGI)	−58.88	−62.183	16	35	61			13
	17	Esperanza	−56.98	−63.40	13	212	201	yes	yes	15
	18	Jubany/Carlini (KGI)	−58.63	−62.23	4	72	119	yes	yes	15

**Figure 2.** Overview of tracks of the three AWS buoys inside the C05 domain. Topography and sea ice concentration as in Fig. 1.

the AWS 3 data stops in December, and a corruption in the end is very likely.

2.4 Radio soundings

To assess the model performance over the whole atmosphere, radio sounding (RS) data were downloaded from the University of Wyoming (<http://weather.uwyo.edu/upperair/sounding.html>, last access: 31 March 2020). The location of RSs are shown in Fig. 1 (diamonds), and detailed informa-

tion is given in Table 5. Some RSs had an unrealistic pressure value at a given height. To remove these, we checked whether or not the deviation from the mean pressure was bigger than 3 times the standard deviation for that height. This removed only 2 %–3 % of the RSs. Further, we only selected RSs done at either 00:00 UTC for Amundsen–Scott and Novolazarevskaya or 12:00 UTC for Halley, Marambio, Neumayer, and Rothera, because these were the only times when the RSs were done regularly.

2.5 Wind lidar

In the austral summer 2015/16 we conducted in situ measurements in the Weddell Sea region. We installed a Doppler lidar onboard the RV *Polarstern* and measured vertical profiles of horizontal wind speed and direction from 24 December till 30 January. In Zentek et al. (2018) we compared the measurements to radio soundings and ship measurements and found a bias (root-mean-square deviation) of approx. $0.1 (1) \text{ m s}^{-1}$ for wind speed and $1 (10)^\circ$ for wind direction, respectively. Lidar wind profiles are available with a vertical resolution of 10 m and with a temporal resolution of ca. 15 min. For the comparison, profiles were average to hourly values and 50 m height resolution (Zentek and Heinemann, 2019a).

For the purpose of comparisons we also set up another model domain with a 1 km resolution and nested it inside the 5 km domain. We ran both with the original settings

Table 5. Information on radio sounding stations. Observation (Obs) at UTC indicates the hour when the sounding was done. Interval shows the usual time difference between the radio soundings (for 85 % of all radio soundings). N indicates the number of radio soundings during 2002–2016.

Station	Longitude	Latitude	Height (m)			Obs at	Interval (in days)	N
			real	C05	C15	UTC		
Marambio	−56.63	−64.23	198	16	5	12	1–5	1312
Neumayer	−8.27	−70.67	50	40	41	12	1	4765
Novolazarevskaya	11.83	−70.77	119		216	0	1	5224
Rothera	−68.13	−67.57	16	6	12	12	1–3	954
Halley	−26.66	−75.58	30	34	35	12	1	4723
Amundsen–Scott	0.00	−90.00	2835		2800	0	1	5168

(C01/C05) and changed turbulence parameters (T01/T05) for the measuring period (see Table 1).

2.6 Methods

For the comparison of CCLM with AMPS and ERA-Interim data, the latter were interpolated bilinearly to the CCLM grid points. For the comparisons to measurements (MS, AWS, RS, and lidar) the nearest neighbouring grid point of CCLM was selected. For surface stations, the CCLM temperature was corrected with 1 K per 100 m for the height difference between the station and the respective grid point (see Tables 4 and 5 for information on grid point heights and difference to the actual station height).

For the radio sounding comparisons, we made a vertical linear interpolation of model and radio sounding data to the same pressure level (equidistant, every 50 hPa). Only data at a certain pressure level were analysed if the number of measurements was more than half of the median of the number of observations over all heights. Prior to the calculation of the correlation for temperature, monthly means were subtracted to remove influence from the seasonal cycle.

In the case of the three AWS buoys on ice floes, the wind speed was measured at a height of approximately 2 m. We therefore assumed a logarithmic wind profile and neutral stability with a roughness length of 0.001 m and thus scaled CCLM 10 m wind speed by a factor of 0.825 in order to calculate the 2 m wind speed. For the AWSs over land no correction was applied as the height of sensors was uncertain or unknown.

For the lidar comparisons we interpolated model, reanalyses, and lidar data to an equidistant grid (height every 50, up to 1000 m). As ERA-Interim only has output every 6 h, we did not interpolate linearly in between, in order to have a sharper distinction to ERA5. Further, note that the lidar data are on average over 1 h around every full hour, which removes small-scale variability as the single measurements were done approximately every 15 min for 1–2 min. This makes it better comparable to the simulation data because although the output is instantaneous, it is unlikely that it shows

turbulence on such a small scale as it always represents the wind average over the whole model grid box.

The wind comparisons are based on the magnitude of wind speed and the wind direction (no vector differences) unless stated otherwise. For wind direction we always assume a maximal possible difference of 180° and removed cases where wind speed is lower than 0.5 m s^{-1} . We compute the root-mean-square error (RMSE) and use the Pearson correlation coefficient (Corr) for temperature and wind speed but use an adapted version for angular variables (Jammalamadaka and Sarma, 1988) (circ.Corr) for wind direction.

3 Comparison with AMPS and ERA

Although a verification with measurements is preferable, due to the small number of stations in polar regions this is not possible for the whole model domain. A comparison to other simulations is therefore an addition to the evaluation, although it has its limits. Gossart et al. (2019) found that in some respects different reanalyses (including ERA5 and ERA-Interim) differ greatly between each other in Antarctica, and thus comparisons of CCLM with these data should not be seen as a validation.

In this analysis the near-surface variables of CCLM are compared with ERA-Interim, ERA5, and AMPS. We computed monthly mean values over the period of 2002–2016 of 2 m temperature and 10 m wind speed. As the data sets of AMPS (with the latest configuration) do not cover the whole period, we selected the years 2014–2016 for the main comparisons. For ERA-Interim we show both time periods.

The 2 m temperature differences for C15 for the winter (April–September) and summer (January–March and October–December) are shown in Fig. 3. The differences for summer are small. For winter C15 is 1–3 K colder over sea ice than ERA5 and ERA-Interim, but this is still a small difference. Over the East Antarctic Plateau (topography approximately higher than 2 km), a large temperature difference of up to 8 K compared to ERA5/ERA-Interim and up to 15 K compared to AMPS is visible during winter.

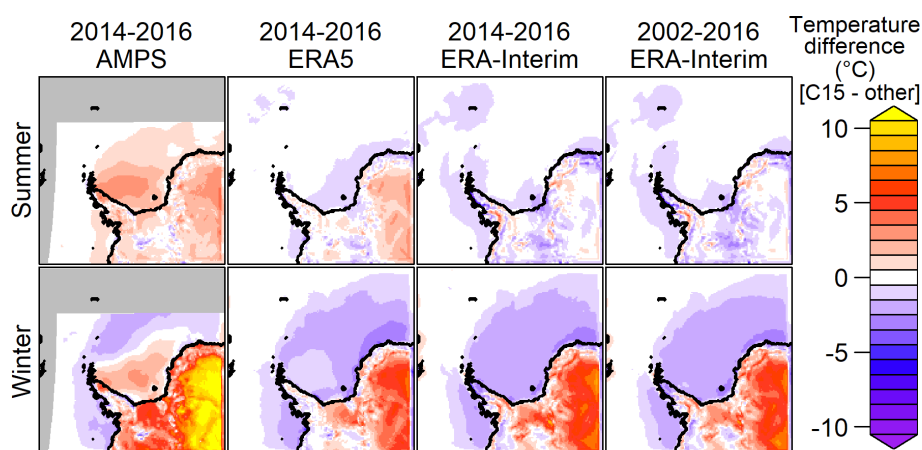


Figure 3. The 2 m temperature difference (C15 minus AMPS, ERA5, and ERA-Interim) for the years 2014–2016 and 2002–2016. Summer (October–March, top) and winter (April–September, bottom) are shown separately. The grey area is outside the AMPS domain.

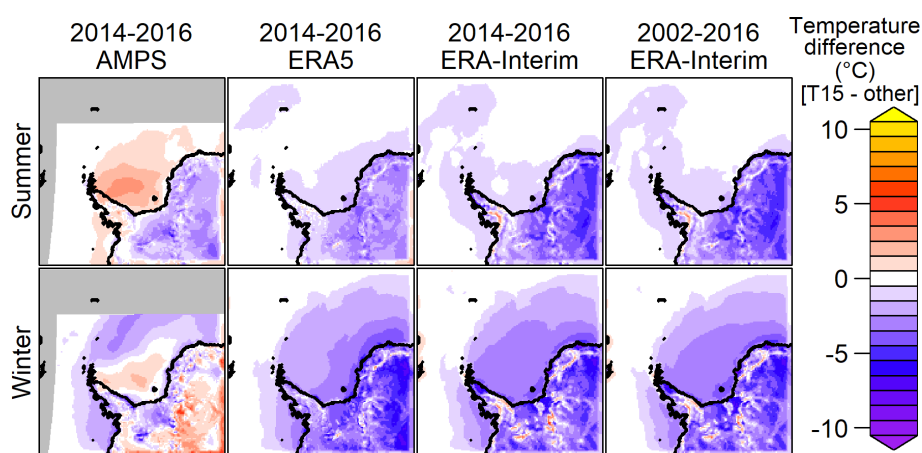


Figure 4. As Fig. 3 but for T15.

The study by Gossart et al. (2019) showed the largest differences in mean temperature between reanalyses over the interior of Antarctica during winter (approx. 8 K) and that ERA and ERA-Interim are warmer than the observations. An evaluation of AMPS (Fig. A1 in Bromwich et al., 2005) showed only a small bias (down to -3 K) of AMPS in the interior of Antarctica. Verifications using surface and radio sounding data (shown in Sect. 4) confirmed that C15 is too warm over the plateau and that this could be attributed to a too strong mixing in the surface boundary layer. This was the reason for changing the turbulence parametrization (T15).

As the change in turbulence parameters allows for more stable atmospheric boundary layer, T15 is overall colder than C15 near the surface, but this influence is very weak during summer or over the sea ice. The 2 m temperature differences for T15 are shown in Fig. 4. Over land and especially over the East Antarctic Plateau the strong difference in winter present in C15 is reduced in T15 compared to AMPS and even turns into a negative difference compared to ERA5 and

ERA-Interim. Figure 5 shows the 10 m wind speed differences for C15 for the summer and winter period. The differences for T15 are very similar (Fig. S1 in the Supplement). Compared to ERA5 and ERA-Interim, C15 shows stronger winds (up to 5 m s^{-1} faster) over the Antarctic Peninsula and in the katabatic wind areas. For the winter period C15 simulates slightly weaker winds over the northern part of the sea ice when compared to ERA5 and ERA-Interim, which may be a result of the different sea ice parametrizations. The difference in C15 compared to AMPS is mainly negative over the ice sheet and slightly positive for the Filchner–Ronne Ice Shelf. The C05 simulation (not shown) shows slightly higher 10 m winds (1 m s^{-1}) compared to the C15 simulation and slightly lower (1 K) 2 m temperature.

Overall the C15 simulation is comparable to ERA5, ERA-Interim, and AMPS model data except for the large temperature difference (C15 warmer) during winter over high topography. When using the modified turbulence scheme, the

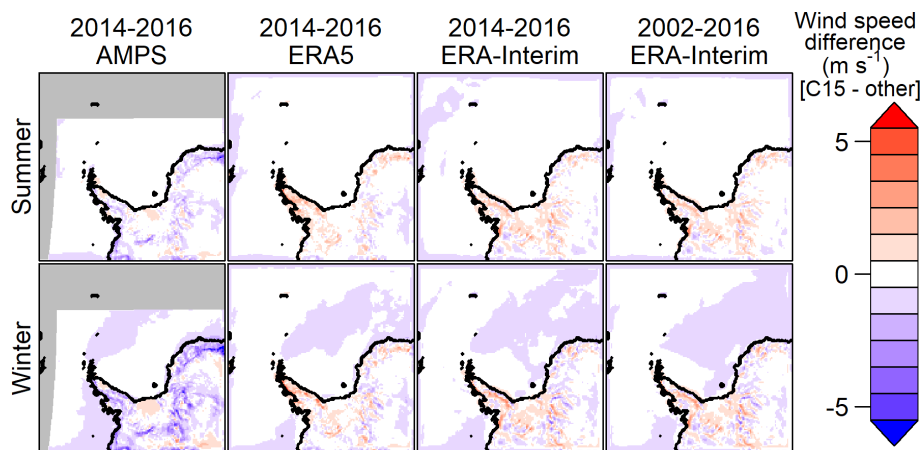


Figure 5. As Fig. 3 but for 10 m wind speed.

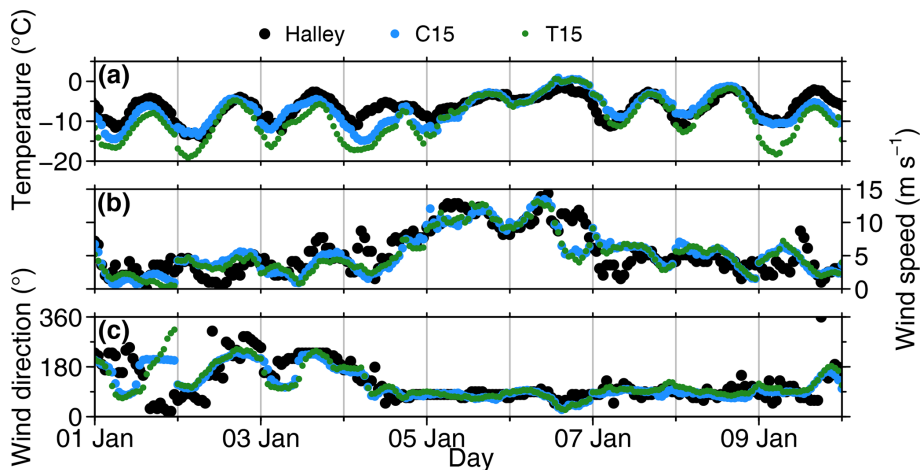


Figure 6. Comparison for Halley of (a) 2 m temperature, (b) 10 m wind speed, and (c) 10 m wind direction for station measurements (black), C15 (blue), and T15 (green) during January 2016. Vertical grey lines indicate the restart of the daily simulations.

difference with respect to the ERA is reversed (T15 colder), but it becomes more similar to AMPS.

4 Comparison to observations

4.1 AWSs and surface stations

To further investigate the differences between CCLM and other simulations from the last section, we compared C15 and T15 with surface measurements. The selection of stations was done after a quality check and using only stations with sufficient record length. In addition the stations should represent typical areas of the Weddell Sea region. The locations of the selected stations are shown in Fig. 1, and detailed information is given in Table 4.

A 10 d comparison of measurements and CCLM model output at the station Halley is shown in Fig. 6. Both C15 and T15 capture the daily cycle of temperature, but T15 under-

estimates the temperature during some nights with low wind speeds. Wind speed and direction of C15 and T15 are similar and agree very well with the measurements. Only during the first day is the change in wind direction different, but the wind speed for this day is also very low.

For the full comparison of C05, C15, and T15 with all stations we calculated monthly bias, RMSE, and correlation for winter and summer separately. Statistics for 2 m temperature are shown in Fig. 7.

The problem of the temperature bias of C15 over the plateau can be demonstrated for the Amundsen–Scott data (no. 1). The +8 K bias for C15 in winter is reduced to less than 1 K in the case of T15, thus showing better performance of T15. The improvement can also be seen for summer. On the other hand, a small cold bias is present for T15 for the coastal region. The statistics for 10 m wind speed (Fig. 8) and direction (Fig. 9) show almost no difference between C15 and T15. The reduced bias of T15 compared to C15 in wind

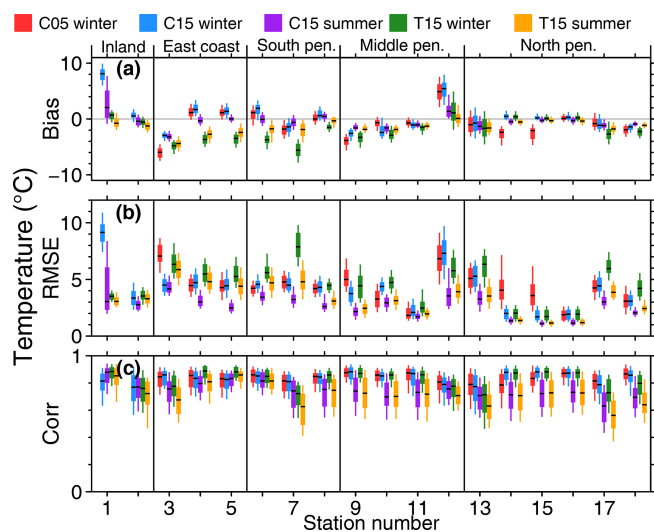


Figure 7. CCLM (a) 2 m temperature bias, (b) RMSE, and (c) correlation for C05, C15, and T15 for different surface stations (see Table 4). Boxes indicate the 25%/75% quantiles, and whiskers indicate the 10%/90% quantiles; the median is indicated by a black line inside the box. Statistics (bias, RMSE, and correlation) are calculated for every month.

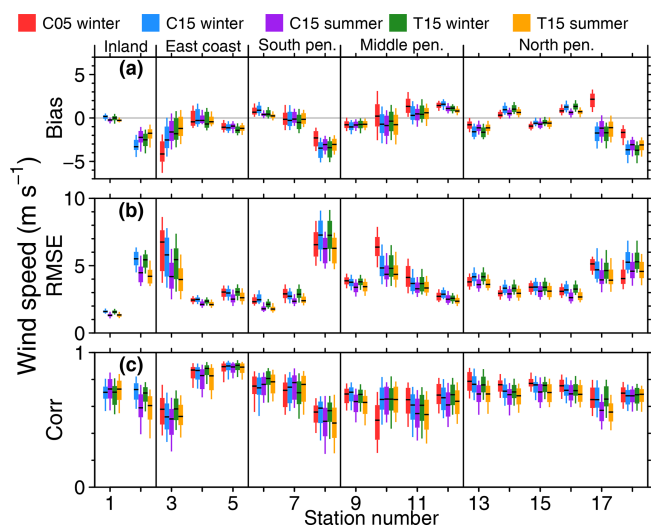


Figure 8. As Fig. 7 but for 10 m wind speed.

direction for Amundsen–Scott (no. 1) is a result of better representation of the stable boundary layer in T15. This yields colder surface temperatures that allow for a stronger wind shear and thus a reduced wind direction bias.

At AWS Union (no. 2) wind direction is almost constant with time, which results in a low correlation although the bias and RMSE are comparable to other stations. For AWS Fossil (no. 8) there are two dominant wind directions both measured and simulated, but they do not always coincide in time, and thus the RMSE is also very high.

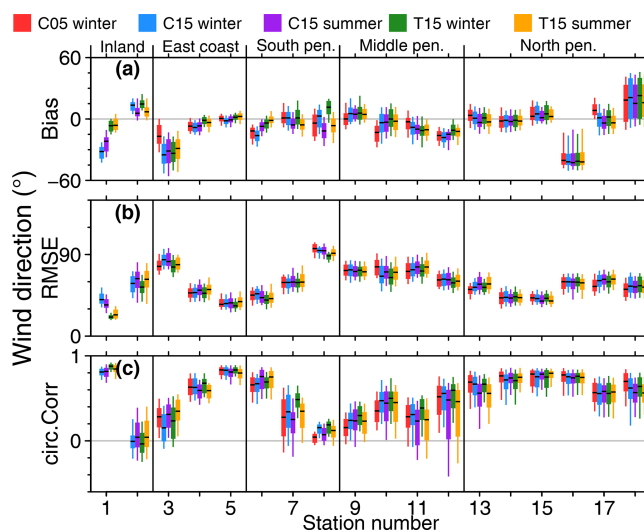


Figure 9. As Fig. 7 but for 10 m wind direction.

The strong bias in wind direction for Bellingshausen (no. 16) is likely explained by the different small-scale topography around the stations, which is not captured at the model resolutions. Also, a data error at the station cannot be ruled out, as the other northern Antarctic Peninsula stations are relatively close to each other and do not show this bias. The reasons for the high bias and RMSE of wind direction for Belgrano II (no. 3) are also likely a result of small-scale topography effects.

Overall CCLM has a tendency to perform slightly better during summer, and differences between the model runs C05, C15, and T15 are only visible in the case of 2 m temperature. When calculating daily instead of monthly bias, RMSE, and correlation, the results are similar but show a much higher variance. These statistics are shown in Figs. S2, S3, and S4.

In Sect. 3, differences in temperature and wind speed were found compared to AMPS, ERA5, and ERA-Interim over sea ice. Observations over sea ice are rare, but the three drifting AWS buoys allow for a comparison of a full yearly cycle for the year 2016. All buoys were deployed in January 2016 near the east coast of the Weddell Sea but at different positions. The no. 1 and 3 buoys drifted from their original position near the coast of northwards out of the Weddell Sea and no. 2 stayed near the east coast (see Fig. 2). An overview of the measurements for the AWS 3 buoy is shown in Fig. 10. The seasonal cycle of temperature is captured by all model runs, and wind speed and direction agree well.

The bias and RMSE of CCLM based on hourly temperature and wind speed for all AWSs are given in Tables 6 and 7. Overall AWS 1 and AWS 3 show similar statistics as both drifted relatively synchronously northwards, while AWS 2 stayed close to the coast north of the station Halley (no. 4). C15 shows a temperature bias of $-0.3/-0.8$ K for AWS 1/AWS 3 during winter, while T15 shows a slightly larger bias of $-1.4/-1.7$ K. This is not as high as the pre-

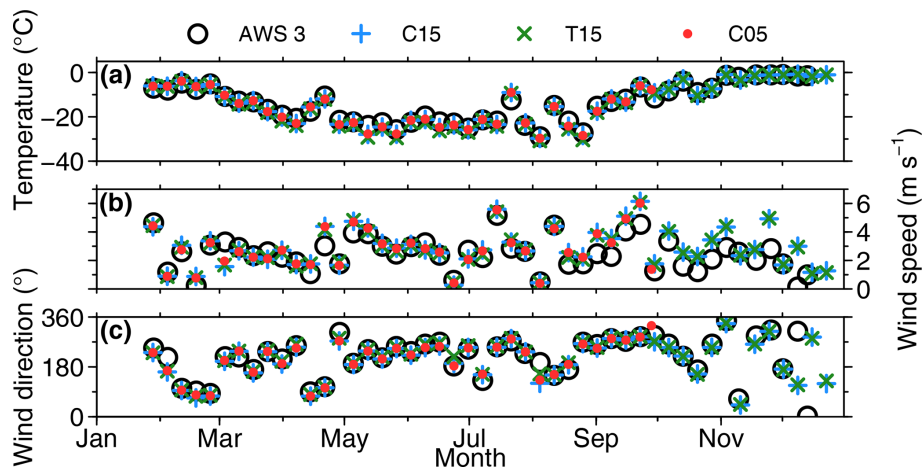


Figure 10. (a) Weekly temperature, (b) wind speed, and (c) wind direction in 2016 for AWS 3 buoy in black (see Fig. 2), C15 (blue), T15 (green), and C05 (red). The weekly mean was computed for zonal and meridional winds.

viously seen cold bias over sea ice during winter of CCLM compared to ERA-Interim and ERA5 of -2 K for C15 and -3 K for T15 (see Figs. 3 and 4). The RMSE is approx. 4 (3) K during summer (winter). For wind speed the RMSE is around 1.5 to 2 m s^{-1} , and biases are equal to or smaller than 0.7 m s^{-1} during summer and a little higher, around 1 m s^{-1} , during winter (Figs. S5 and S6).

4.2 Radio soundings

The location of the radio soundings are shown in Fig. 1 as diamonds. Note that Novolazarevskaya is very close to the model boundary (eight grid points), and CCLM may be partly influenced by the ERA-Interim boundary data. The radio soundings are done regularly at 00:00 UTC (6 h after model start) for Novolazarevskaya and Amundsen–Scott and 12:00 UTC (18 h after model start) for Marambio, Neumayer, Rothera, and Halley.

To address the differences between C15 and T15, a comparison of the mean temperature for the lowest 1 km of the atmosphere is shown in Fig. 11. The changed turbulence parametrization only influences the cases of strong surface inversions. For Amundsen–Scott (f) there is a clear improvement in T15 for the mean SBL structure during winter and also a slight improvement during summer. Similar but weaker improvements can be seen for the eastern Weddell Sea – Halley (e) and Neumayer (b). However, for Novolazarevskaya (c) and Rothera (d) a stronger bias in the lowest 100 m is present for T15.

The whole profiles of the temperature statistics (Fig. 12) show almost no bias except below 800 hPa, and the RMSE is around 1 K in the upper troposphere for the coastal stations. The bias is slightly lower for C05 (only winter) and for C15 in summer. The correlations are larger than 0.8. These results are similar to the findings of Souverijns et al. (2019), which show a mean average error of 0.5 to 1.4 K. For

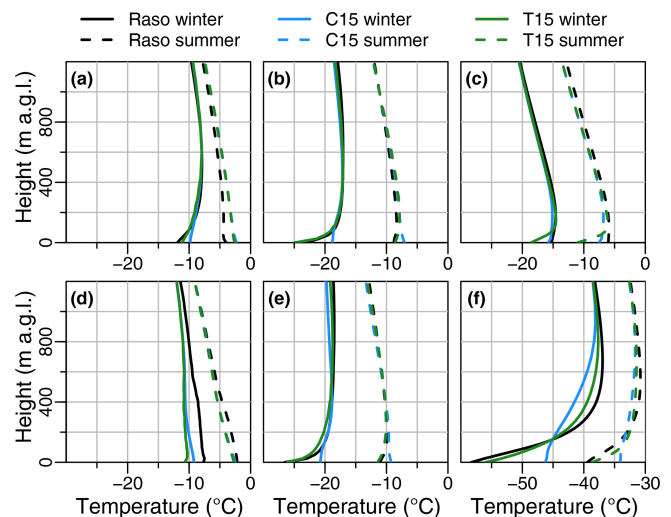


Figure 11. Mean temperature of radio sounding (Raso; black), C15 (blue), and T15 (green) during winter (solid line) and during summer (dashed line) for the stations (a) Marambio, (b) Neumayer, (c) Novolazarevskaya, (d) Rothera, (e) Halley, and (f) Amundsen–Scott. Note the different range on the x axis for (f) Amundsen–Scott. The abbreviation a.g.l. is short for “above ground level”, meaning above the surface.

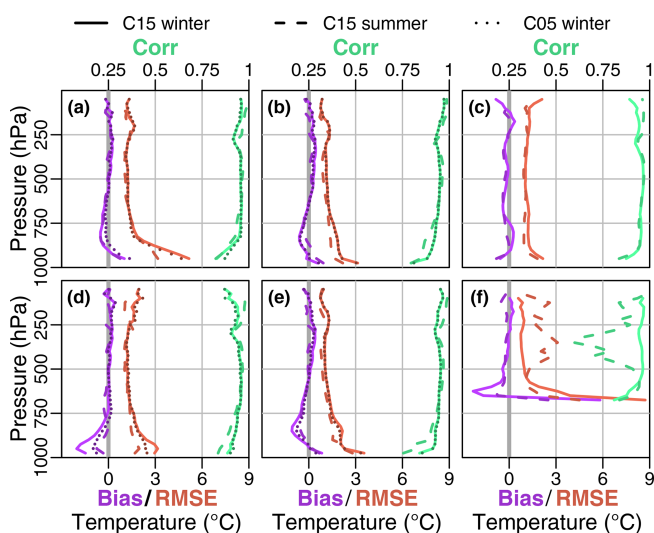
Amundsen–Scott (f) a large positive bias and a large RMSE is present in the lowest layers, which is most pronounced in winter. While for the winter the RMSE and the correlation above 500 hPa are comparable to the coastal stations, a larger RMSE and correlations of less than 0.75 are present above 500 hPa during summer. The higher resolution of C05 yields only slight improvements for Marambio (a) and Rothera (d) at the Antarctic Peninsula, where the influence of the topography is larger than at the other stations. We did not include

Table 6. CCLM temperature bias and RMSE for the three AWS buoys (see Fig. 2). *N* indicates the number of data points (hours) in 2016. Winter months are April–September, and summer months are January–March and October–December.

Name	<i>N</i> (hours)	Temperature bias				Temperature RMSE			
		Winter		Summer		Winter		Summer	
		C15	T15	C15	T15	C15	T15	C15	T15
AWS 1	7044	−0.3	−1.4	0.9	0.7	3.7	4.0	2.7	2.8
AWS 2	7915	2.5	0.4	1.5	0.8	4.9	3.6	3.6	3.2
AWS 3	6640	−0.8	−1.7	0.1	−0.1	3.4	4.0	2.3	2.4

Table 7. As Table 6 but for wind speed.

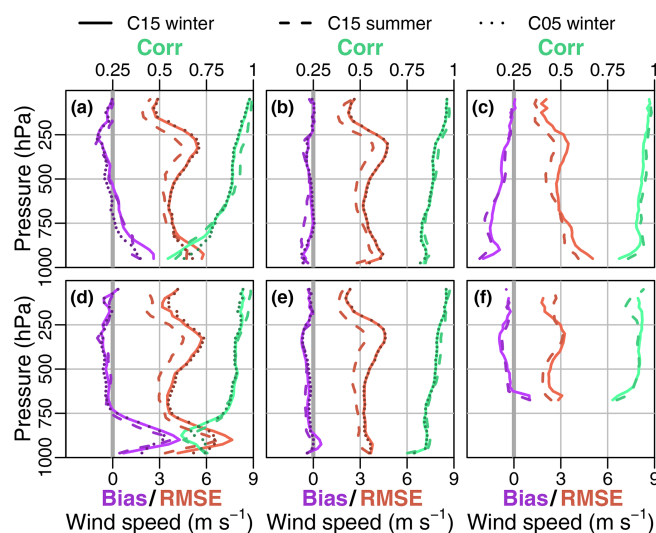
Name	<i>N</i> (hours)	Wind speed bias				Wind speed RMSE			
		Winter		Summer		Winter		Summer	
		C15	T15	C15	T15	C15	T15	C15	T15
AWS 1	7044	1.0	0.8	0.5	0.4	1.8	1.8	1.5	1.5
AWS 2	7915	1.2	0.9	0.7	0.6	2.0	1.8	1.7	1.6
AWS 3	6640	0.7	0.6	0.7	0.7	1.8	1.9	2.0	2.0

**Figure 12.** Temperature bias, RMSE (bottom axes), and correlation (top axes) of C15 during winter (solid line), C15 during summer (dashed line), and C05 during winter (dotted line) for the stations (a) Marambio, (b) Neumayer, (c) Novolazarevskaya, (d) Rothera, (e) Halley, and (f) Amundsen–Scott.

T15 in Fig. 12 as the statistics were almost identical to C15 with the exception of the lowest levels for Amundsen–Scott.

Above the surface inversion, differences for C05, C15, and T15 and the summer and winter season are relatively small, with only a minor exception of a small increase in RMSE above 500 hPa for Amundsen–Scott (f) during summer.

For the comparison of wind speed (Fig. 13) and direction (Fig. 14) we excluded T15 again, as it was almost identi-

**Figure 13.** Like Fig. 12 but for wind speed.

cal to C15. The bias is again almost 0 except near the surface. The RMSE for wind speed is around 3 to 4 m s^{−1} and slightly lower during summer. Bias and RMSE are largest for Marambio (a) and Rothera (d) in the lowest 200 hPa, and as for the temperature C05 yields slight improvements for these stations. Souverijns et al. (2019) found a mean average error for wind speed of 2.1 to 3.6 m s^{−1} for all seasons. The RMSE for wind direction is around 50° near the surface and reduces with height to 20° at 250 hPa, except for Amundsen–Scott (f) where it stays around 50°.

4.3 Wind lidar

Wind profile measurements from lidar data are available for 24 December 2015 to 30 January 2016. We selected two case studies for comparisons. The first one features the occurrence of three low-level jets (LLJs) during a night and the following morning. The second case study gives an overview of the differences and similarities between lidar measurements and simulations during a 10 d period.

4.3.1 Overall statistics

We also computed the overall statistics for all available lidar measurements (see Table 8). The different CCLM runs are very similar, with no or only very small bias in wind speed and a RMSE of around 2 m s^{-1} . For wind direction there was a small bias of -5° present and a RMSE of 30° . ERA5 and ERA-Interim show similar values. This good agreement could stem partially from the fact that the radio soundings of the ship ($2\text{--}3 \text{ d}^{-1}$) are assimilated in ERA5 and ERA-Interim, which show also good agreement with the lidar data (Zentek et al., 2018). The computation of the statistics for different heights showed that the wind speed RMSE of CCLM is largest around a height of 1000 m, while the RMSE of ERA5 and ERA-Interim is mostly constant with height (Fig. S7).

4.3.2 Case study A

During the night from 16 to 17 January 2016 the RV *Polarstern* operated in a polynya in the lee of the iceberg A23 (see Fig. 1). Three LLJ events were observed with the lidar (Fig. 15). The first LLJ occurred between 00:00 and 02:00 UTC (LLJ1). The LLJ between 06:00 and 08:00 UTC (LLJ2) was captured by the radio sounding at 07:00 UTC (Zentek et al., 2018), and the wind maximum between 10:00 and 14:00 UTC (LLJ3) was also measured by a radio sounding at heights of 800 to 1000 m at 12:00 UTC. While the 6-hourly ERA-Interim data cannot reproduce the structure and evolution of the wind field of the lidar measurements, the hourly ERA5 data capture LLJ2 and LLJ3, which is likely explained by the assimilation of radio sounding data. However, the LLJ wind speeds are underestimated, and LLJ1 is missing in ERA5. The CCLM simulations (nested in ERA-Interim) show that the increase in resolution yields increased wind speeds particularly for LLJ3, but the height of the LLJ is too low. An indication of LLJ1 is seen in the CCLM simulations, but the wind speed is underestimated. The overall pattern of the wind direction field is well reproduced by all CCLM simulations. Since the position of the ship was not stationary for this period, we also tested for a dependency on the chosen grid point of the model, by choosing one grid point over the iceberg A23 and one in the middle of the open polynya instead of the ship location. This had only a small

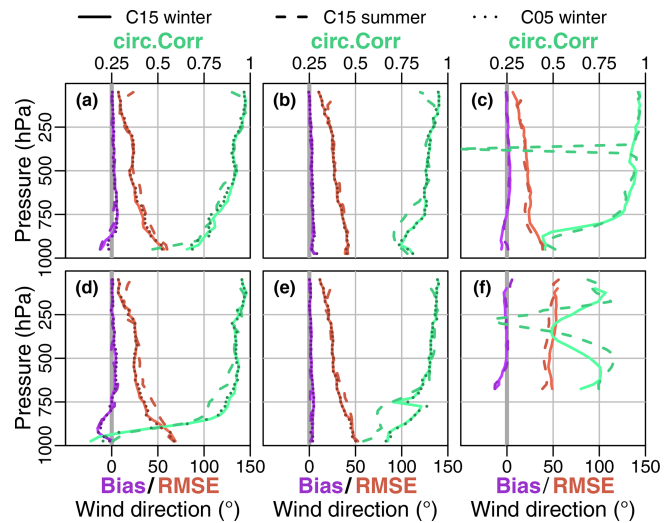


Figure 14. Like Fig. 12 but for wind direction.

effect, and we therefore concluded that all the changes and patterns are mostly time and height dependent.

4.3.3 Case study B

From 20 to 30 January 2016 RV *Polarstern* was navigating around the area of the Brunt Ice Shelf (see Fig. 1). The days show a broad variety of different wind patterns (Fig. 16) ranging from no wind (on the 21st) to wind speeds exceeding 20 m s^{-1} (on the 29th) and also featuring vertically inhomogeneous winds both in speed and direction (on the 24th–26th). On the scale of days, T15, ERA5, ERA-Interim, and the lidar show the same evolution of the wind field. On smaller scales, CCLM and the lidar show more detail, but CCLM does not always agree well with the lidar (e.g. on the 26th). ERA5 agrees well with the lidar data and sometimes even catches the small-scale details of measured wind patterns (e.g. on the 27th). T05 and T01 are very similar to T15, with only little-increased wind speeds (Fig. S8).

If we presume that the lidar measurements are representative of the winds in the whole area that is covered by the model grid box, this case study gives a good impression of how reliable reanalyses and models are on those scales; e.g. for a simulated LLJ we cannot always assume that a LLJ was really present, even if the overall RMSE is shown to be smaller than 3 m s^{-1} .

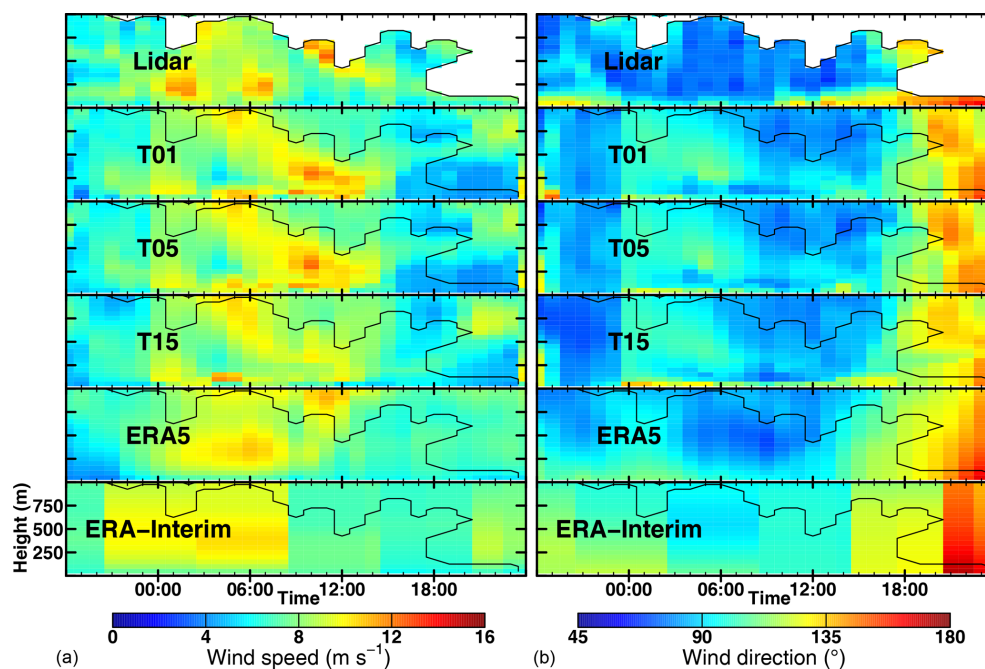
5 Summary

We used the nonhydrostatic model COSMO-CLM (CCLM) in forecast mode and nested in ERA-Interim data to produce a long-term hindcast (2002–2016) for the Weddell Sea region with resolutions of approximately 15 and 5 km and two different turbulence parametrizations. Sea ice concentration is prescribed from satellite data, and a thermodynamic sea ice

Table 8. Bias and RMSE for wind speed and direction compared to lidar measurements during December 2015 and January 2016.

		C01*	T01*	C05	T05	C15	T15	ERA5	ERA-Interim
Wind speed (m s^{-1})	Bias	0.0	0.1	0.0	0.1	-0.1	0.0	-0.3	-0.2
	RMSE	2.1	2.4	2.2	2.3	2.3	2.3	1.7	2.0
Wind direction ($^{\circ}$)	Bias	-3	-5	-3	-5	-5	-5	-1	-2
	RMSE	28	30	32	29	32	30	22	29

* The runs with 1 km resolution were not performed for the whole period but only for 37 and 25 d (out of 39 d) for T01 and C01, respectively.

**Figure 15.** Time–height cross sections for (a) wind speed and (b) direction for 16 January 2016 18:00 UTC to 17 January 2016 12:00 UTC.

model is used. In this paper we evaluated the performance of the model in terms of temperature, wind speed, and direction using data from Antarctic stations and AWSs over land and sea ice. Comparisons to the AMPS model and reanalyses data showed good agreement, except for a large difference in surface temperature over the Antarctic Plateau. The warm bias is also found in comparison to measurements at the Amundsen–Scott station (surface and radio sounding), where the reference run C15 showed a strong warm bias near the surface (+8 K). This bias was removed in the second run T15 by adjusting the turbulence parametrization, which results in a more realistic representation of the surface inversion over the Antarctic Plateau. But this caused also a small cold bias (down to -4 K) for other surface stations located on ice shelves in the eastern Weddell Sea. A comparison with measurements over the sea ice of the Weddell Sea done by three AWS buoys for 1 year showed small biases for temperatures around ± 1 K and for wind speed of 1 m s^{-1} .

Comparisons with radio soundings showed a model bias around 0 for all model levels except near the surface. In general, a RMSE of 1–2 K for temperature and $3\text{--}4 \text{ m s}^{-1}$ for wind speed was found.

The comparison of CCLM simulations at resolutions down to 1 km with wind data from Doppler lidar measurements during December 2015 and January 2016 in the southern and eastern Weddell Sea yielded almost no bias in wind speed and a RMSE of ca. 2 m s^{-1} . For wind direction the bias was ca. -5° with a RMSE of around 30° . Overall, CCLM is able to produce realistic evolution and structures of the wind in the ABL, but for specific events like LLJs differences in the timing and locations of the LLJs occur.

6 Conclusions and outlook

CCLM shows a good representation of temperature and wind for the Weddell Sea region. The adjustment of the turbulence parametrization for very stable conditions is important

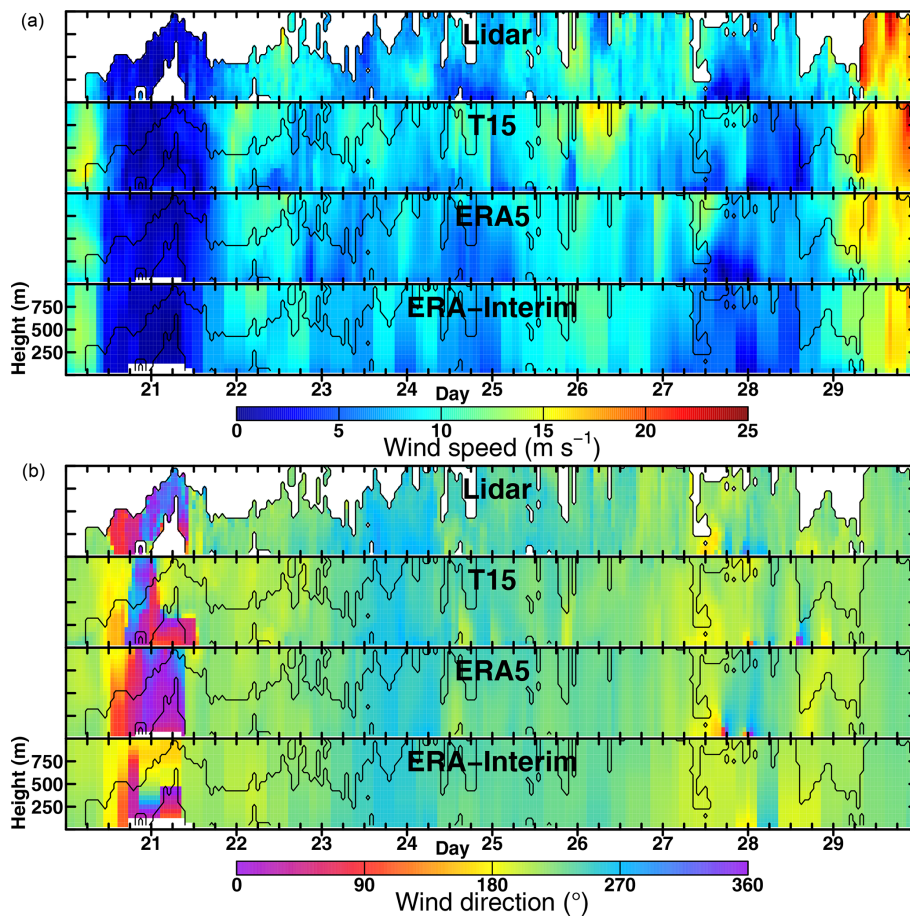


Figure 16. Time–height cross sections for (a) wind speed and (b) direction for 20 January 00:00 UTC to 30 January 00:00 UTC.

for the realistic representation of the surface inversion over the Antarctic Plateau. Since verification data for simulations are rare in the Antarctic, new types of measurements like Doppler lidar or controlled meteorological balloons (Hole et al., 2016) can give additional insights into the performance of atmospheric models. For the comparisons of CCLM with ship-based Doppler lidar in the present study the benefit of CCLM compared to ERA5 is small due to the facts that the data from the ship were assimilated in the reanalysis and effects of topography were small. A larger benefit is seen for polynya areas and the Antarctic Peninsula with small-scale topography. The YOPP (Year of Polar Prediction) project will lead to more and enhanced observational data, which can be used for further verifications in the future. Future work with CCLM will be the study of atmosphere–ice–ocean interactions processes and quantification of sea ice production in polynyas.

Code and data availability. The COSMO-CLM model is completely free of charge for all research applications. The current version of the COSMO-CLM model is available from the CCLM website: <https://www.clm-community.eu> (last access:

31 March 2020) under the licence <http://www.cosmo-model.org/content/consortium/licencing.htm> (last access: 31 March 2020). The particular version of the CCLM model used in this study is based on the official version 5.0 with additions to the sea ice module (according to Schröder et al., 2011) and the changes in the turbulence parametrizations described in this study. If eligible, access can be granted to the model source code at zenodo (Zentek and Heinemann, 2019b). The model output used in this study is archived at zenodo (Zentek and Heinemann, 2019c). The full model output data will be archived for a limited amount of time and are available on request (zentek@uni-trier.de). The model documentation is archived at zenodo (Zentek, 2019). The scripts and configurations to run the simulations are archived at zenodo as well (Zentek and Heinemann, 2019d). The scripts used to analyse the simulations and produce the figures in this paper are archived at zenodo as well (Zentek and Heinemann, 2019e).

Supplement. The supplement related to this article is available online at: <https://doi.org/10.5194/gmd-13-1809-2020-supplement>.

Author contributions. RZ carried out the setup of the model, simulation, data curation, methodology, validation, visualization, and

writing of the original draft. GH carried out the conceptualization, methodology, review of the writing, editing, supervision, project administration, and funding acquisition.

Competing interests. The authors declare that they have no conflict of interest.

Acknowledgements. The lidar measurements were performed during the *Polarstern* cruise PS96 funded by the Alfred-Wegener-Institut under *Polarstern* grant AWI_PS96_03. The COSMO-CLM model was provided by the German Meteorological Service and the CLM community. Computing time was provided by DKRZ. AWS buoy sea ice measurements for 2016 are from <http://www.meereisportal.de> (last access: 31 March 2020) (funding: REKLIM-2013-04). From all of the software that was used, we would like to highlight cdo, nco, R, and RStudio and the R package data.table. We thank Niels Souverijns (KU Leuven, Belgium) and our colleagues in Trier for helpful discussions.

Financial support. The research was funded by the SPP 1158 “Antarctic research” of the DFG (Deutsche Forschungsgemeinschaft) under grant HE 2740/19. The publication was funded by the Open Access Fund of Universität Trier and the German Research Foundation (DFG) within the Open Access Publishing funding programme.

Review statement. This paper was edited by Fabien Maussion and reviewed by two anonymous referees.

References

- Akperov, M., Rinke, A., Mokhov, I. I., Matthes, H., Semenov, V. A., Adakudlu, M., Cassano, J., Christensen, J. H., Dembitskaya, M. A., Dethloff, K., Fettweis, X., Glisan, J., Gutjahr, O., Heinemann, G., Koenigk, T., Koldunov, N. V., Laprise, R., Mottram, R., Nikiéma, O., Scinocca, J. F., Sein, D., Sobolowski, S., Winger, K., and Zhang, W.: Cyclone Activity in the Arctic From an Ensemble of Regional Climate Models (Arctic CORDEX), *J. Geophys. Res.-Atmos.*, 123, 2537–2554, <https://doi.org/10.1002/2017JD027703>, 2018.
- Bauer, M., Schröder, D., Heinemann, G., Willmes, S., and Ebner, L.: Quantifying polynya ice production in the Laptev Sea with the COSMO model, *Polar Res.*, 32, 20922, <https://doi.org/10.3402/polar.v32i0.20922>, 2013.
- Bromwich, D. H., Monaghan, A. J., Manning, K. W., and Powers, J. G.: Real-Time Forecasting for the Antarctic: An Evaluation of the Antarctic Mesoscale Prediction System (AMPS), *Mon. Weather Rev.*, 133, 579–603, <https://doi.org/10.1175/mwr-2881.1>, 2005.
- Cape, M. R., Vernet, M., Skvarca, P., Marinsek, S., Scambos, T., and Domack, E.: Foehn winds link climate-driven warming to ice shelf evolution in Antarctica, *J. Geophys. Res.-Atmos.*, 120, 11037–11057, <https://doi.org/10.1002/2015JD023465>, 2015.
- Cerenzia, I., Tampieri, F., and Stefania Tesini, M.: Diagnosis of Turbulence Schema in Stable Atmospheric Conditions and Sensitivity Tests, *COSMO Newsl.*, 14, 28–36, 2014.
- Dee, D. P., Uppala, S. M., Simmons, A. J., Berrisford, P., Poli, P., Kobayashi, S., Andrae, U., Balmaseda, M. A., Balsamo, G., Bauer, P., Bechtold, P., Beljaars, A. C. M., van de Berg, L., Bidlot, J., Bormann, N., Delsol, C., Dragani, R., Fuentes, M., Geer, A. J., Haimberger, L., Healy, S. B., Hersbach, H., Hólm, E. V., Isaksen, I., Kållberg, P., Köhler, M., Matricardi, M., McNally, A. P., Monge-Sanz, B. M., Morcrette, J.-J., Park, B.-K., Peubey, C., Rosnay, P. D., Tavolato, C., Thépaut, J.-N., and Vitart, F.: The ERA-Interim reanalysis: configuration and performance of the data assimilation system, *Q. J. Roy. Meteor. Soc.*, 137, 553–597, <https://doi.org/10.1002/qj.828>, 2011.
- Ebner, L., Heinemann, G., Haid, V., and Timmermann, R.: Katabatic winds and polynya dynamics at Coats Land, Antarctica, *Antarct. Sci.*, 26, 309–326, <https://doi.org/10.1017/S0954102013000679>, 2014.
- Elvidge, A. D., Renfrew, I. A., King, J. C., Orr, A., Lachlan-Cope, T. A., Weeks, M., and Gray, S. L.: Foehn jets over the Larsen C Ice Shelf, Antarctica, *Q. J. Roy. Meteor. Soc.*, 141, 698–713, <https://doi.org/10.1002/qj.2382>, 2015.
- Ezraty, R., Girard-Ardhuin, F., Piollé, J. F., Kaleschke, L., and Heygster, G.: Arctic and Antarctic sea ice concentration and Arctic sea ice drift estimated from SSM/I. User’s manual, version 2.1, available at: <ftp://ftp.ifremer.fr/ifremer/cersat/products/gridded/psi-drift/documentation/ssmi.pdf>, (last access: 5 May 2019), 2007.
- Giorgi, F. and Gutowski, W. J.: Regional Dynamical Downscaling and the CORDEX Initiative, *Annu. Rev. Env. Resour.*, 40, 467–490, <https://doi.org/10.1146/annurev-environ-102014-021217>, 2015.
- Gorodetskaya, I. V., Tsukernik, M., Claes, K., Ralph, M. F., Neff, W. D., and Van Lipzig, N. P. M.: The role of atmospheric rivers in anomalous snow accumulation in East Antarctica, *Geophys. Res. Lett.*, 41, 6199–6206, <https://doi.org/10.1002/2014GL060881>, 2014.
- Gossart, A., Helsen, S., Lenaerts, J. T. M., Broucke, S. V., van Lipzig, N. P. M., and Souverijns, N.: An Evaluation of Surface Climatology in State-of-the-Art Reanalyses over the Antarctic Ice Sheet, *J. Climate*, 32, 6899–6915, <https://doi.org/10.1175/jcli-d-19-0030.1>, 2019.
- Grosfeld, K., Treffeisen, R., Asseng, J., Bartsch, A., Bräuer, B., Fritzsche, B., Gerdes, R., Hendricks, S., Hiller, W., Heygster, G., Krumpen, T., Lemke, P., Melzheimer, C., Nicolaus, M., Ricker, R., and Weigelt, M.: Online sea-ice knowledge and data platform, available at: <http://www.meereisportal.de> (last access: 31 March 2020), Polarforschung, Bremerhaven, Alfred Wegener Institute for Polar and Marine Research and German Society of Polar Research, 143–155, <https://doi.org/10.2312/polfor.2016.011>, 2016.
- Gutjahr, O., Heinemann, G., Preußner, A., Willmes, S., and Drüe, C.: Quantification of ice production in Laptev Sea polynyas and its sensitivity to thin-ice parameterizations in a regional climate model, *The Cryosphere*, 10, 2999–3019, <https://doi.org/10.5194/tc-10-2999-2016>, 2016.
- Haid, V., Timmermann, R., Ebner, L., and Heinemann, G.: Atmospheric forcing of coastal polynyas in the south-

- western Weddell Sea, *Antarct. Sci.*, 27, 388–402, <https://doi.org/10.1017/S0954102014000893>, 2015.
- Hebbinghaus, H. and Heinemann, G.: LM simulations of the Greenland boundary layer, comparison with local measurements and SNOWPACK simulations of drifting snow, *Cold Reg. Sci. Technol.*, 46, 36–51, <https://doi.org/10.1016/j.coldregions.2006.05.003>, 2006.
- Heinemann, G.: Idealized simulations of the Antarctic katabatic wind system with a three-dimensional mesoscale model, *J. Geophys. Res.-Atmos.*, 102, 13825–13834, <https://doi.org/10.1029/97JD00457>, 1997.
- Hersbach, H., de Rosnay, P., Bell, B., Schepers, D., Simmons, A., Soci, C., Abdalla, S., Alonso-Balmaseda, M., Balsamo, G., Bechtold, P., Berrisford, P., Bidlot, J.-R., Boisséson, E. d., Bonavita, M., Browne, P., Buizza, R., Dahlgren, P., Dee, D., Dragani, R., Diamantakis, M., Flemming, J., Forbes, R., Geer, A. J., Haiden, T., Hólm, E., Haimberger, L., Hogan, R., Horányi, A., Janiskova, M., Laloyaux, P., Lopez, P., Muñoz-Sabater, J., Peubey, C., Radu, R., Richardson, D., Thépaut, J.-N., Vitart, F., Yang, X., Zsótér, E., and Zuo, H.: Operational global reanalysis: progress, future directions and synergies with NWP, ERA Report Series, <https://doi.org/10.21957/tkic6g3wm>, 2018.
- Hole, L. R., Bello, A. P., Roberts, T. J., Voss, P. B., and Vihma, T.: Measurements by controlled meteorological balloons in coastal areas of Antarctica, *Antarct. Sci.*, 28, 387–394, <https://doi.org/10.1017/s0954102016000213>, 2016.
- Jammalamadaka, S. and Sarma, Y.: A correlation coefficient for angular variables, *Statistical Theory and Data Analysis 2*, Elsevier Science Publishers B.V. (North.Holland), 1988.
- King, J. C., Kirchaessner, A., Bevan, S., Elvidge, A. D., Kuipers Munneke, P., Luckman, A., Orr, A., Renfrew, I. A., and van den Broeke, M. R.: The Impact of Föhn Winds on Surface Energy Balance During the 2010–2011 Melt Season Over Larsen C Ice Shelf, Antarctica, *J. Geophys. Res.-Atmos.*, 122, 12062–12076, <https://doi.org/10.1002/2017JD026809>, 2017.
- Kohnemann, S. H. E., Heinemann, G., Bromwich, D. H., and Gutjahr, O.: Extreme Warming in the Kara Sea and Barents Sea during the Winter Period 2000–16, *J. Climate*, 30, 8913–8927, <https://doi.org/10.1175/jcli-d-16-0693.1>, 2017.
- Költzow, M.: The effect of a new snow and sea ice albedo scheme on regional climate model simulations, *J. Geophys. Res.*, 112, D07110, <https://doi.org/10.1029/2006jd007693>, 2007.
- Kurtz, N. T. and Markus, T.: Satellite observations of Antarctic sea ice thickness and volume, *J. Geophys. Res.-Oceans*, 117, C08025, <https://doi.org/10.1029/2012JC008141>, 2012.
- Lott, F. and Miller, M. J.: A new subgrid-scale orographic drag parametrization: Its formulation and testing, *Q. J. Roy. Meteor. Soc.*, 123, 101–127, <https://doi.org/10.1002/qj.49712353704>, 1997.
- Powers, J. G., Manning, K. W., Bromwich, D. H., Cassano, J. J., and Cayette, A. M.: A Decade of Antarctic Science Support Through Amps, *B. Am. Meteorol. Soc.*, 93, 1699–1712, <https://doi.org/10.1175/bams-d-11-00186.1>, 2012.
- Prein, A. F., Langhans, W., Fossler, G., Ferrone, A., Ban, N., Goergen, K., Keller, M., Tölle, M., Gutjahr, O., Feser, F., Brisson, E., Kollet, S., Schmidli, J., Van Lipzig, Nicole P. M., and Leung, R.: A review on regional convection-permitting climate modeling: Demonstrations, prospects, and challenges, *Rev. Geophys.*, 53, 323–361, <https://doi.org/10.1002/2014RG000475>, 2015.
- Rockel, B., Will, A., and Hense, A.: The Regional Climate Model COSMO-CLM (CCLM), *Meteorol. Z.*, 17, 347–348, <https://doi.org/10.1127/0941-2948/2008/0309>, 2008.
- Rummukainen, M.: State-of-the-art with regional climate models, *WIRES Clim. Change*, 1, 82–96, <https://doi.org/10.1002/wcc.8>, 2010.
- Schaffer, J. and Timmermann, R.: Greenland and Antarctic ice sheet topography, cavity geometry, and global bathymetry (RTopo-2), links to NetCDF files, PANGAEA, <https://doi.org/10.1594/pangaea.856844>, data set to: Schaffer, J., Timmermann, R., Arndt, J. E., Kristensen, S. S., Mayer, C., Morlighem, M., and Steinhage, D.: A global, high-resolution data set of ice sheet topography, cavity geometry, and ocean bathymetry, *Earth Syst. Sci. Data*, 8, 543–557, <https://doi.org/10.5194/essd-8-543-2016>, 2016.
- Schaffer, J., Timmermann, R., Arndt, J. E., Kristensen, S. S., Mayer, C., Morlighem, M., and Steinhage, D.: A global, high-resolution data set of ice sheet topography, cavity geometry, and ocean bathymetry, *Earth Syst. Sci. Data*, 8, 543–557, <https://doi.org/10.5194/essd-8-543-2016>, 2016.
- Schröder, D., Heinemann, G., and Willmes, S.: The impact of a thermodynamic sea-ice module in the COSMO numerical weather prediction model on simulations for the Laptev Sea, Siberian Arctic, *Polar Res.*, 30, 6334, <https://doi.org/10.3402/polar.v30i0.6334>, 2011.
- Souverein, N., Gossart, A., Gorodetskaya, I. V., Lhermitte, S., Mangold, A., Laffineur, Q., Delcloo, A., and van Lipzig, N. P. M.: How does the ice sheet surface mass balance relate to snowfall? Insights from a ground-based precipitation radar in East Antarctica, *The Cryosphere*, 12, 1987–2003, <https://doi.org/10.5194/tc-12-1987-2018>, 2018.
- Souverein, N., Gossart, A., Demuzere, M., Lenaerts, J. T. M., Medley, B., Gorodetskaya, I. V., Vanden Broucke, S., and van Lipzig, N. P. M.: A New Regional Climate Model for POLAR-CORDEX: Evaluation of a 30-Year Hindcast with COSMO-CLM 2 Over Antarctica, *J. Geophys. Res.-Atmos.*, 124, 1405–1427, <https://doi.org/10.1029/2018JD028862>, 2019.
- Spren, G., Kaleschke, L., and Heygster, G.: Sea ice remote sensing using AMSR-E 89-GHz channels, *J. Geophys. Res.*, 113, 14485, <https://doi.org/10.1029/2005jc003384>, 2008.
- Stoppel, J., Doms, G., Schättler, U., Bitzer, H. W., Gassmann, A., Damrath, U., and Gregoric, G.: Meso-gamma scale forecasts using the nonhydrostatic model LM, *Meteorol. Atmos. Phys.*, 82, 75–96, <https://doi.org/10.1007/s00703-001-0592-9>, 2003.
- Turton, J., Kirchaessner, A., Ross, A., King, J., and Kuipers Munneke, P.: Foehn-induced surface melting of the Larsen C ice shelf, Antarctica, in: EGU General Assembly Conference Abstracts, vol. 19 of EGU General Assembly Conference Abstracts, 23–28 April, Vienna, 4692 pp., 2017.
- van Kampenhout, L., Lenaerts, J. T. M., Lipscomb, W. H., Sacks, W. J., Lawrence, D. M., Slater, A. G., and van den Broeke, M. R.: Improving the Representation of Polar Snow and Firn in the Community Earth System Model, *J. Adv. Model. Earth Sy.*, 9, 2583–2600, <https://doi.org/10.1002/2017ms000988>, 2017.
- van Lipzig, N. P. M.: Precipitation, sublimation, and snow drift in the Antarctic Peninsula region from a regional atmospheric model, *J. Geophys. Res.*, 109, 31739, <https://doi.org/10.1029/2004JD004701>, 2004.

- van Wessem, J. M., Reijmer, C. H., van de Berg, W. J., van den Broeke, M. R., Cook, A. J., van Uft, L. H., and van Meijgaard, E.: Temperature and Wind Climate of the Antarctic Peninsula as Simulated by a High-Resolution Regional Atmospheric Climate Model, *J. Climate*, 28, 7306–7326, <https://doi.org/10.1175/JCLI-D-15-0060.1>, 2015.
- Zentek, R.: COSMO documentation (archived version from 2019, uploaded with permission of the DWD), <https://doi.org/10.5281/zenodo.3339384>, 2019.
- Zentek, R. and Heinemann, G.: Wind and backscatter profiles measured by a wind lidar during POLARSTERN cruise PS96 (ANT-XXXI/2 FROSN), <https://doi.org/10.1594/PANGAEA.902794>, 2019a.
- Zentek, R. and Heinemann, G.: CCLM simulation (Antarctica 2002–2016) – model source codes and domain files, <https://doi.org/10.5281/zenodo.3355411>, 2019b.
- Zentek, R. and Heinemann, G.: CCLM simulation (Antarctica 2002–2016) – selected data, <https://doi.org/10.5281/zenodo.3355401>, 2019c.
- Zentek, R. and Heinemann, G.: CCLM simulation (Antarctica 2002–2016) – scripts and configuration files, <https://doi.org/10.5281/zenodo.3339363>, 2019d.
- Zentek, R. and Heinemann, G.: CCLM simulation (Antarctica 2002–2016) – analysis and plotting scripts, <https://doi.org/10.5281/zenodo.3361625>, 2019e.
- Zentek, R., Kohnemann, S. H. E., and Heinemann, G.: Analysis of the performance of a ship-borne scanning wind lidar in the Arctic and Antarctic, *Atmos. Meas. Tech.*, 11, 5781–5795, <https://doi.org/10.5194/amt-11-5781-2018>, 2018.
- Zhang, J. and Rothrock, D. A.: Modeling Global Sea Ice with a Thickness and Enthalpy Distribution Model in Generalized Curvilinear Coordinates, *Mon. Weather Rev.*, 131, 845–861, [https://doi.org/10.1175/1520-0493\(2003\)131<0845:MGSIIWA>2.0.CO;2](https://doi.org/10.1175/1520-0493(2003)131<0845:MGSIIWA>2.0.CO;2), 2003.

4.4 Publication 3

distributed under the terms and conditions of the Creative Commons Attribution (CC BY) license

<https://creativecommons.org/licenses/by/4.0/>

Article

A Model-Based Climatology of Low-Level Jets in the Weddell Sea Region of the Antarctic

Günther Heinemann *  and Rolf Zentek 

Department of Environmental Meteorology, University of Trier, 54286 Trier, Germany; zentek@uni-trier.de
* Correspondence: heinemann@uni-trier.de; Tel.: +49-651-201-4623

Abstract: Low-level jets (LLJs) are climatological features in polar regions. It is well known that katabatic winds over the slopes of the Antarctic ice sheet are associated with strong LLJs. Barrier winds occurring, e.g., along the Antarctic Peninsula may also show LLJ structures. A few observational studies show that LLJs occur over sea ice regions. We present a model-based climatology of the wind field, of low-level inversions and of LLJs in the Weddell Sea region of the Antarctic for the period 2002–2016. The sensitivity of the LLJ detection on the selection of the wind speed maximum is investigated. The common criterion of an anomaly of at least 2 m/s is extended to a relative criterion of wind speed decrease above and below the LLJ. The frequencies of LLJs are sensitive to the choice of the relative criterion, i.e., if the value for the relative decrease exceeds 15%. The LLJs are evaluated with respect to the frequency distributions of height, speed, directional shear and stability for different regions. LLJs are most frequent in the katabatic wind regime over the ice sheet and in barrier wind regions. During winter, katabatic LLJs occur with frequencies of more than 70% in many areas. Katabatic LLJs show a narrow range of heights (mostly below 200 m) and speeds (typically 10–20 m/s), while LLJs over the sea ice cover a broad range of speeds and heights. LLJs are associated with surface inversions or low-level lifted inversions. LLJs in the katabatic wind and barrier wind regions can last several days during winter. The duration of LLJs is sensitive to the LLJ definition criteria. We propose to use only the absolute criterion for model studies.

Keywords: Antarctic; stable boundary layer; low-level jets; inversion; katabatic winds



Citation: Heinemann, G.; Zentek, R. A Model-Based Climatology of Low-Level Jets in the Weddell Sea Region of the Antarctic. *Atmosphere* **2021**, *12*, 1635. <https://doi.org/10.3390/atmos12121635>

Academic Editors: Giampietro Casasanta, Stefania Argentini and Igor Petenko

Received: 4 November 2021
Accepted: 4 December 2021
Published: 7 December 2021

Publisher's Note: MDPI stays neutral with regard to jurisdictional claims in published maps and institutional affiliations.



Copyright: © 2021 by the authors. Licensee MDPI, Basel, Switzerland. This article is an open access article distributed under the terms and conditions of the Creative Commons Attribution (CC BY) license (<https://creativecommons.org/licenses/by/4.0/>).

1. Introduction

Low-level jets (LLJs) are climatological features in polar regions. Strong wind shear occurs below and above the LLJ core, which has a strong influence on the turbulence structure. LLJs are relevant for long-range associated transports on a scale of several hundreds of kilometers, such as in atmospheric river events [1].

There are several mechanisms for the generation of LLJs in polar regions. We start with an overview of these different types of LLJs with references of observational studies. In zones of high baroclinicity such as synoptic fronts or boundary layer fronts at the sea ice edge, the vertical shear of the geostrophic wind and surface friction generate baroclinic LLJs. For the Antarctic, [2] presents observations of an LLJ over the sea ice of the Weddell Sea associated with a synoptic front. In [3], they show observational case studies of baroclinic LLJs at the sea ice edge in the Arctic. In [4], they found for an observational study for a five months period over Arctic sea ice that most LLJs were baroclinic. The study of [5] covered a full Arctic winter period in the Laptev Sea and they concluded that the main driving mechanism for LLJs was baroclinicity.

A second mechanism for LLJs over flat terrain is the inertial oscillation caused by a stabilization of the atmospheric boundary layer (ABL). The formation of a stable boundary layer (SBL) can be caused by the formation of a surface inversion by surface cooling, but also by warm air advection. For an observational study over the sea ice of the Weddell Sea, [6] identified the inertial oscillation as the most frequent process for LLJs. An example

of an inertial oscillation LLJ observed with tether sondes over the Ronne ice shelf is shown by [7].

Katabatic winds forming in the SBL over slopes of polar ice sheets are typically associated with LLJs. An aircraft-based study of katabatic winds over Greenland has shown LLJs exceeding 20 m/s [8,9]. For the Antarctic, such detailed measurements over the slopes of the inland ice do not exist. Doppler sodar measurements of wind profiles on 28 days over a slope south of Halley station (Antarctica) showed LLJs at levels below 60 m and with maximum winds of 8–10 m/s [10]. These winds are relatively weak compared to the near-surface measurements of katabatic winds in other areas of the Antarctic [11,12]. For coastal stations in the East Antarctic, [11] reported mean monthly near-surface wind speeds of around 12 m/s during the summer (December–January), but from March to October, mean monthly wind speeds of 15–25 m/s were observed. Observations of katabatic LLJs in East Antarctica during summer show a pronounced daily course with wind maxima around 10 m/s [13]. At Dome C (East Antarctica), [14] observed very shallow LLJs (below 35 m) during the summer. Analyses of radiosonde profiles at Antarctic coastal stations for 2010–2017 showed low-level katabatic jets in the mean wind profiles [15].

Topographic LLJs are caused by the channelling of the flow in the SBL by gaps or by the response of the flow to mountain barriers. Prominent examples for the Antarctic are barrier winds along the Antarctic Peninsula [16] and the Transantarctic Mountains at the Ross Ice Shelf [17,18]. However, only near-surface observations are available for these studies. One of the rare observational studies of gap flow jets during foehn events at the Antarctic Peninsula is shown by [19] using aircraft data. A weak LLJ during a foehn event detected by radiosonde measurements over the Larsen Ice Shelf is shown by [20], while a strong LLJ with 15 m/s during a foehn situation over the Larsen Ice Shelf was measured by [21] using aircraft data.

While observational studies of the ABL structure in the Antarctic are rare, numerical weather forecast and regional climate models (RCMs) have been used in the last decades for the understanding of ABL processes and their interactions. Numerical models are the only means to study these processes at a high resolution with full 3D spatial coverage and to provide climatological information. A vast amount of numerical model studies for shorter periods and case studies exist for phenomena such as LLJs for barrier winds (e.g., [17,22]), gap flow jets (e.g., [19]), katabatic LLJs (e.g., [23,24]) and LLJs above the sea ice of the Weddell Sea [25]. Ref. [26] show that for a sufficient consideration of topography-induced atmospheric processes a resolution of at least 15 km is necessary. Most climatological studies using RCMs have focused on the near-surface wind field and the surface energy and mass balance (e.g., [27–29]). A climatology of the katabatic wind structure for East Antarctica is shown by [30] using the hydrostatic regional climate model RACMO (regional atmospheric climate model) with 55 km resolution for the period 1980–2004. They find a katabatic LLJ exceeding 10 m/s at a height of about 200 m above the surface for the winter and concluded that the resulting turbulent mixing is the dominant heat loss in the ABL.

In the present study, we present a climatology of LLJs for the Antarctic based on simulations with the regional non-hydrostatic consortium for small-scale modelling (COSMO) model in climate mode (COSMO-CLM (CCLM)). CCLM is used for simulations with a resolution of about 15 km for the period 2002 to 2016. One-hourly data are used to derive mean annual and seasonal statistics of LLJ frequency, wind speed and boundary layer characteristics associated with LLJs.

2. Materials and Methods

2.1. The CCLM Model

The COSMO-CLM (CCLM) model is a non-hydrostatic regional climate model used by a large climate research community. CCLM has been applied for several studies of the ABL in the polar regions [27,31–35]. For the present paper, CCLM is used with a horizontal resolution of 15 km for the Weddell Sea region of the Antarctic (Figure 1) with the setup as described in [31]. Initial and boundary data are taken from ERA-Interim reanalyses [36]

with six-hourly resolution. The model is used in a forecast mode (reinitialized daily at 18:00 UTC, with a spin-up time of 6 h). No nudging is performed. Model output is available every 1 h. In the vertical, the model extends up to 25 km with 60 vertical levels, 14 levels are below 500 m in order to obtain a high resolution of the boundary layer. The first model level is at 5 m above the surface. CCLM uses a two-layer sea ice model [37] and modifications for the stable boundary layer [31,34]. Sea ice concentration is taken from AMSR-E (advanced microwave scanning radiometer—for Earth Observing System) and AMSR2 (advanced microwave scanning radiometer 2) data, and for data gaps SSMIS (special sensor microwave imager/sounder) data are used [38]. Sea ice thickness is prescribed with 1 m for sea-ice concentrations (SIC) exceeding 70%, which is a reasonable estimate for the Weddell Sea (see [39]). Thin ice with 10 cm thickness is attributed to areas with $15\% < \text{SIC} \leq 70\%$, and areas with $\text{SIC} \leq 15\%$ are ice-free. The albedo of sea ice is parameterized as a function of ice thickness and temperature as described in [35].

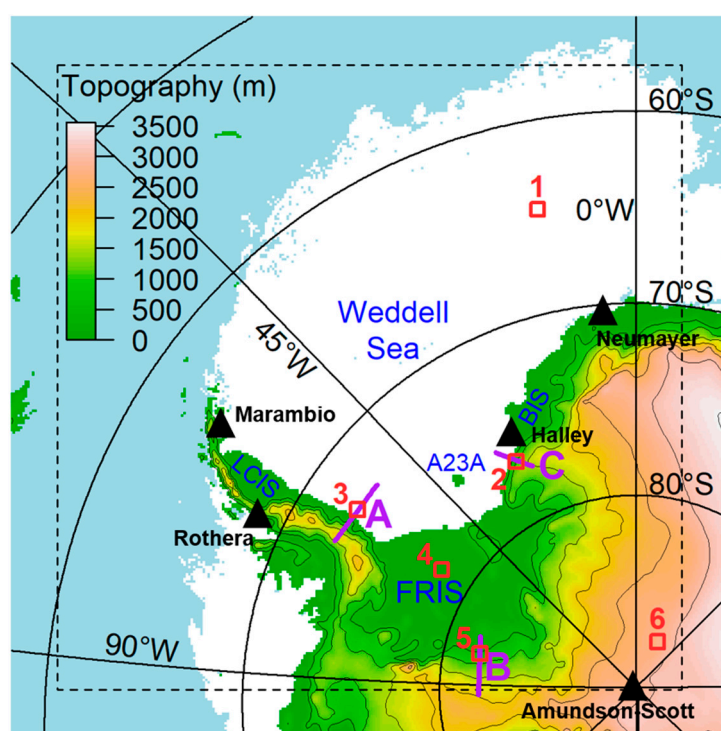


Figure 1. Model domain of CCLM with topography (shaded and isolines every 500 m) and sea ice area (white) for a day in winter (iceberg A23A marked). The dashed box shows the area used for the evaluation, A, B and C mark cross-sections. The red squares mark specific areas for case studies and statistics. FRIS = Filchner-Ronne Ice Shelf, LCIS = Larsen-C Ice Shelf, BIS = Brunt Ice Shelf. Black triangles mark radiosonde stations inside the evaluation domain.

Topography data with 1 km resolution are taken from [40]. The sub-grid scale variance of the topography is used for the roughness length parameterization over land. The total roughness length is the sum of the roughness length computed from the land use and from the standard deviation (SD) of the sub-grid scale orography (SSO) depending on the grid size as described in [41]. The SSO SD (Figure 2a) is typically smaller than 20 m but can also exceed 100 m in areas with highly structured topography. Around a few mountain peaks values up to 300 m are present. While the roughness length from land use is only 0.001 m for the inland ice, the total roughness length is much larger in areas with large SSO SD (Figure 2b) with typical values of 0.02–0.04 m, but also with peak values exceeding 1.0 m. The information about the SSO is also used for the form drag parameterization of mountains. The scheme of [42] is implemented in CCLM.

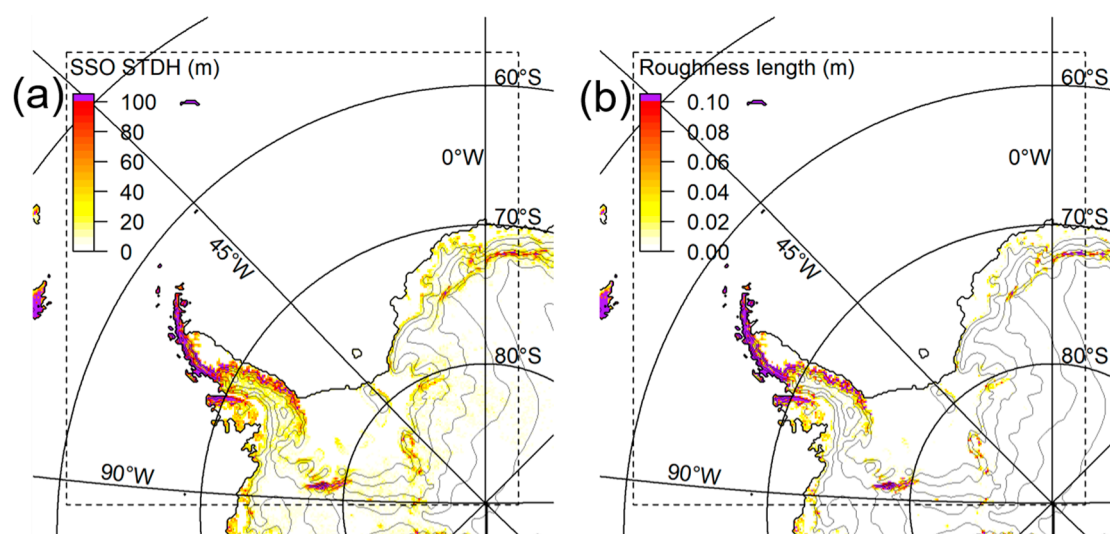


Figure 2. (a) Standard deviation of the sub-grid scale orography (SSO). (b) Roughness length over the land areas. The dashed box shows the area used for the evaluation.

A full technical documentation of the CCLM model can be found in [43]. The modifications for the stable boundary layer include a reduction in the lower limit of minimum diffusion coefficients to improve the simulation of the surface inversion [31] and katabatic winds over ice sheets [34].

2.2. Low-Level Jet Detection

Low-level jets are distinct wind maxima in the lower troposphere. For the specific definition, different criteria are used in the literature. A common criterion is to set a threshold for the anomaly of the wind maximum compared to the wind speeds below and above the height of the jet. Most studies use a value of 2 m/s as an absolute criterion, e.g., [4–6]. Ref. [44] defined the jet core height as the height of the maximum wind speed, which is at least 25% and 2 m/s larger than the next minima. This definition prevents a false classification at very low wind speeds (absolute criterion) and at very high wind speeds (relative criterion). The relative criterion serves also as a filter for turbulence-generated wind maxima at high wind speeds [44].

In this study we use the LLJ definition according to [44], but with modified search criteria. In addition, we investigate the sensitivity to different values of the relative criterion. In a first step, we search for the wind maxima below 1000 m and minima below 1500 m by using the vertical gradient of the wind speed (see Figure 3). If the gradient at the top level (1500 m) is negative, the top level is considered a local minimum. Then it is tested, if the wind decreases above and below the maxima according to the absolute criterium within a search radius, which is taken as the minimum of 1.5 times the jet height (h_{jet}) and $(0.2h_{\text{jet}} + 300 \text{ m})$, which limits the search radius to an upper limit of 500 m. This prevents the detection of very broad wind maxima. In the case of multiple maxima, [44] state to simply take the lowest maximum as LLJ height, but we found that this fails in several cases. One case is that two maxima are close together so that they actually represent one LLJ. The detection method described above would reject both maxima, if the minimum between the maxima is not low enough to fulfil the absolute and relative criteria. The method was thus expanded by using a lower bound for the search radius and additional checks. In order to prevent a local minimum between two maxima being created by a single data point, we take at least two data points below and above the maximum level to search for minima. If more than one maximum fulfilling all these steps are found, we take the lowest as a detected LLJ. In a last step, we apply the relative criterion with different values. The LLJ detection is performed for every CCLM grid point with hourly resolution for the period

2002–2016, which results in about 130,000 profiles at each of the ca. 67,000 grid points for the investigation period.

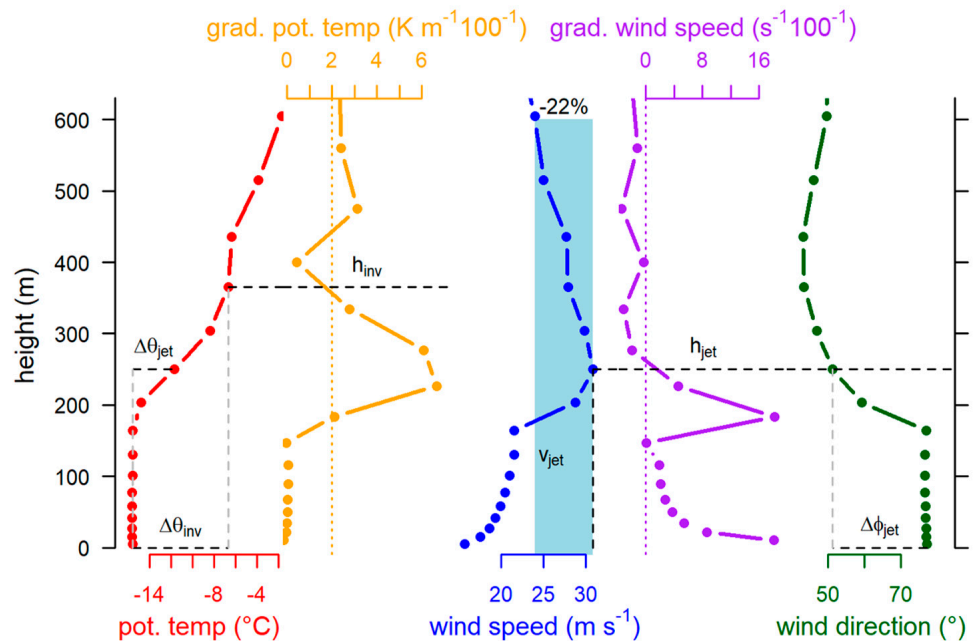


Figure 3. Overview of the vertical search algorithm for the inversion height (h_{inv}), inversion strength ($\Delta\theta_{inv}$), LLJ height (h_{jet}), LLJ speed (v_{jet}), LLJ temperature difference ($\Delta\theta_{jet}$), and LLJ wind direction difference ($\Delta\phi_{jet}$). Vertical profiles are shown for potential temperature (red), gradient of potential temperature (orange), wind speed (blue), gradient of wind speed (purple) and wind direction (green) for a grid point over sea ice (point 1 in Figure 1) at 1100 UTC on 1 July 2016. The light blue bar shows the search radius, the relative decrease within the search radius is given in percent. Dots mark the model levels.

The choice of the relative criterion was found to be of great importance for the overall statistics of the LLJ frequency. The sensitivity for different values from 0% (only absolute criterion of 2 m/s) to 25% are shown in Figure 4. The frequency is defined as the number of profiles with LLJ relative to the total number of profiles. While the difference between 0%, 5% and 10% is very small, the change for 15% is larger particularly over the ocean and sea ice areas. For larger values of this criterion a further decrease of LLJ frequency over ocean and sea ice can be seen, but the decrease is also large over the inland ice. In the following evaluations, we do not take the relative criterion into account, but we show comparisons to 15% and 25% relative criterion in some figures.

2.3. Boundary Layer and Inversion Height

The height of the boundary layer is computed in CCLM as the height where the bulk Richardson number exceeds a value of 0.33 for the SBL [45] and 0.22 for the convective boundary layer (CBL) [46]. Additionally, we compute the height of the surface inversion or the height of an elevated inversion similar to [47]. In this method, the inversion height is computed as the height, where the gradient of the potential temperature drops from above to below a threshold value in a search from bottom to top. This is performed separately for surface inversions and elevated inversions (100 to 1000 m). Elevated inversions are typical for an SBL with strong winds such as katabatic or gap flows [34,47]. If no elevated inversion is found, surface inversions are searched by applying the same check starting at the surface.

This procedure is demonstrated by the LLJ case over the sea ice in Figure 3. This case during winter shows a well-mixed boundary layer for the lowest 200 m capped by an inversion. The maximum of the temperature gradient occurs at the inversion base, and

the inversion height is determined as about 370 m, if a threshold of 2 K/100 m is taken. In this case study, the LLJ height is close to the inversion base, but below the inversion height. The LLJ shows a distinct directional shear of about 30° compared to the near-surface and mixed-layer values.

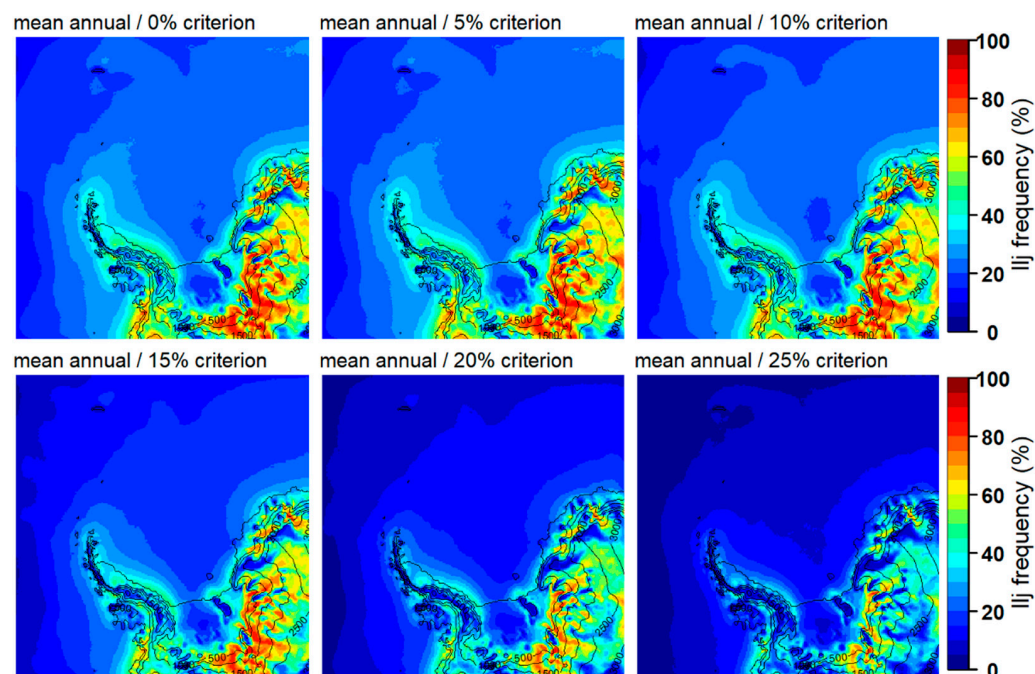


Figure 4. LLJ frequency for 2002–2016 for different relative criteria (all with 2 m/s absolute criterion).

The used method determines the top of the inversion as the inversion height and is sensitive to the choice of the threshold for the temperature gradient. This choice follows other studies which used values of 2 K/100 m [47,48] or 1.5 K/100 m [9]. The sensitivity of the inversion height with respect to different thresholds is shown in Figure S1 in the supplement. A higher threshold leads to lower inversions over the inland ice and over the sea ice, but the sensitivity is relatively weak. A threshold of 2 K/100 m was taken for the evaluations of this study.

3. Results

3.1. Case Studies of LLJs

3.1.1. LLJ over the Sea Ice on 1 July 2016

The vertical profiles for this case were already shown in Figure 3. A very strong LLJ with 30 m/s is present at about 250 m. The decrease in the wind speed with height inside the search radius is 22%. When applying the relative criterion of 25%, as proposed by [44], this very strong LLJ would not be detected. The synoptic situation at 1100 UTC on 1 July 2016 is shown in Figure 5a. The profile shown in Figure 3 is located close to a frontal zone of a cyclone close to the sea ice edge. The 10 m wind is very high, south of the frontal zone. The wind speed difference between 200 m and 800 m shows a narrow zone of more than 10 m/s decrease of the wind with height (Figure 5b), which reflects that the LLJ extends over a large distance.

3.1.2. Katabatic LLJ over Coats Land on 10 June 2014

The vertical profiles for this case are shown in Figure 6 for 0500 UTC 10 June 2014, an overview of the synoptic situation is given in Figure 7. A well-defined LLJ with 17 m/s is present at about 50 m, which is at the height of the surface inversion. The wind minimum with less than 5 m/s is found at 400 m. Since the wind decrease with height inside the search radius is larger than 25%, this LLJ would have been also detected using the criteria

of [44]. The wind direction turns slightly in the katabatic layer but shows a large change to southwesterly winds at a height of 400 m. Figure 7a shows that the katabatic wind over Coats Land is influenced by a cyclone with its center of the Brunt Ice Shelf (see Figure 1). The katabatic flow merges with the southwesterly flow along the coast associated with the cyclone (Figure 7b), which also dominates the flow above the katabatic layer. This is a case where the synoptic pressure gradient is opposite to the katabatic forcing. This situation was found also for other katabatic wind events over Coats Land by [24].

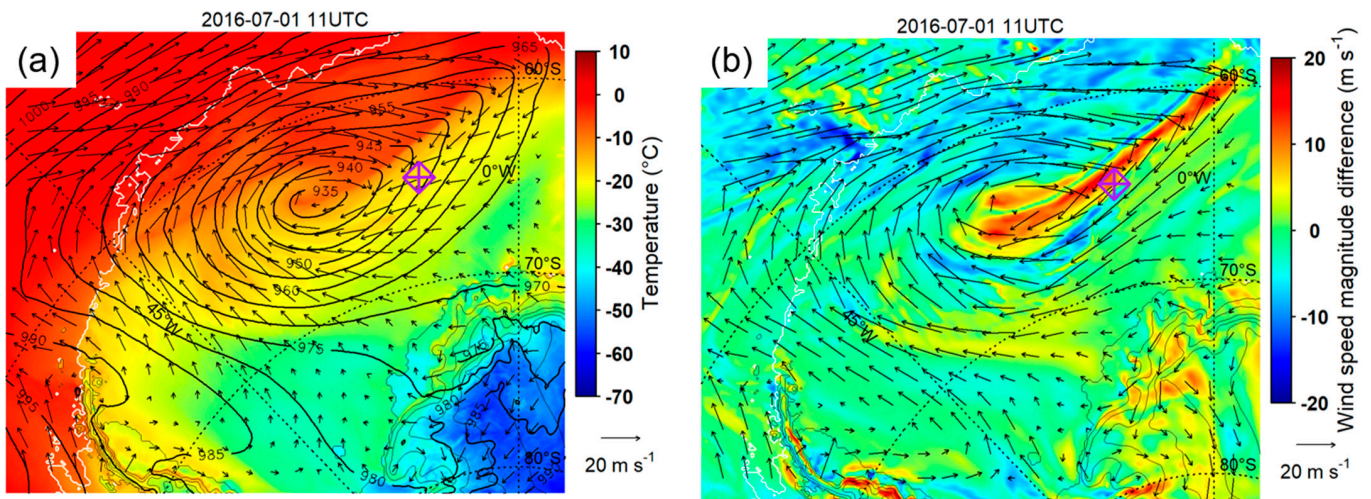


Figure 5. (a) Mean sea level pressure (MSLP, isolines every 5 hPa), 2 m temperature (color bar) and 10 m-wind vector (at every 10th grid point) and (b) wind speed difference between 200 m and 800 m and 200 m-wind vectors for 1100 UTC 1 July 2016 for a subregion of the model domain. The diamond marks the location of the wind profile of Figure 3. The sea ice edge is marked by a thick white line. Topography is shown as grey isolines every 500 m.

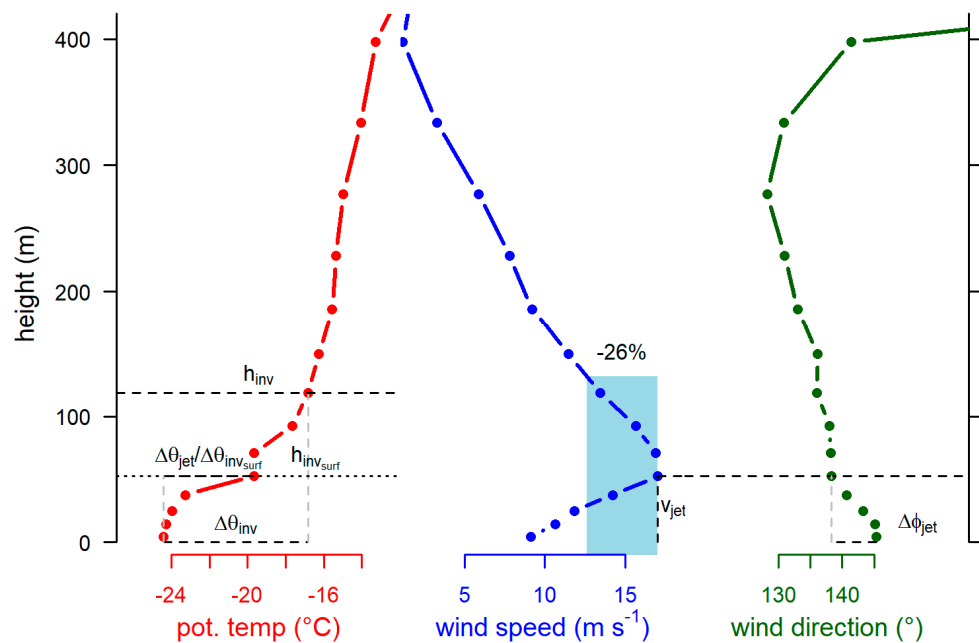


Figure 6. Vertical profiles of the potential temperature (red), wind speed (blue), and wind direction (green) for a grid point over Coats Land (point 2 in Figure 1) for 0500 UTC 10 June 2014 (see Figure 7 for the location). The light blue bar shows the search radius, the relative decrease within the search radius is given in percent. Dots mark the model levels.

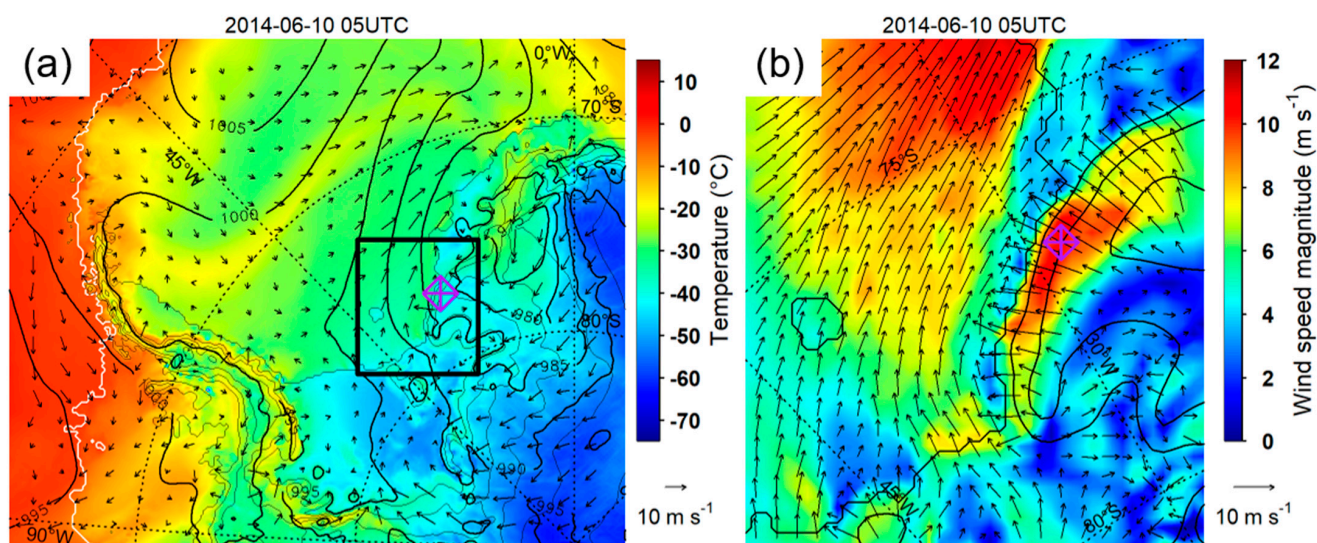


Figure 7. (a) Mean sea level pressure (MSLP, isolines every 5 hPa), 2 m temperature (color bar) and 10 m-wind vector (at every 10th grid point) for the Weddell Sea region and (b) 10 m-wind speed (color bar) and 10 m-wind vector (at every 2nd grid point) for 0500 UTC 10 June 2014 for a subregion of the model domain (marked by the box in (a)). The diamond marks the location of the wind profile of Figure 6. Topography is shown as gray and black isolines every 500 m in (a) and (b), respectively.

The main difference of this katabatic LLJ to the case of a baroclinic LLJ over the sea ice is that the wind speed in the lowest 50 m is much weaker in the katabatic layer, since the synoptic pressure gradient near the surface is very large for the baroclinic LLJ. In the katabatic case, the LLJ is associated with a surface inversion, while the baroclinic LLJ is at the top of a well-mixed boundary layer.

3.2. Wind Climatology of the ABL

Figure 8 shows the mean wind field at 10 m above the ground for the period 2002–2016. The different regimes of the near-surface wind can be clearly seen. Highest mean winds occur in the katabatic wind regime over the slopes of the ice sheet. The katabatic wind is also associated with the highest values of the directional constancy (directional constancy is defined as the ratio of the magnitude of the mean wind vector and the mean wind speed). The katabatic wind-field structure shows small-scale variations, which are a result of topographic channeling (Figure 1) but are also caused by the structures in the roughness length by subgrid-scale orography (Figure 2), since a high SSO SD leads to a large roughness length. As a second regime, the barrier flow at the east side of the Antarctic Peninsula can be seen as a flow parallel to the topography with increased values of the directional constancy. The northern part of the model domain is dominated by the westerly flow with increased wind, but relatively low constancy. Sea ice areas in the southern Weddell Sea as well as the area of the Filchner–Ronne Ice Shelf has weak wind and also low constancy. An exception is Berkner Island, which develops its own katabatic wind field with high constancy. The wind fields at 100, 200 and 500 m (supplementary material Figures S2–S4) show that the wind over the ice sheet has a downslope component at 100 m, but turns parallel to the topography isolines for 200 and 500 m.

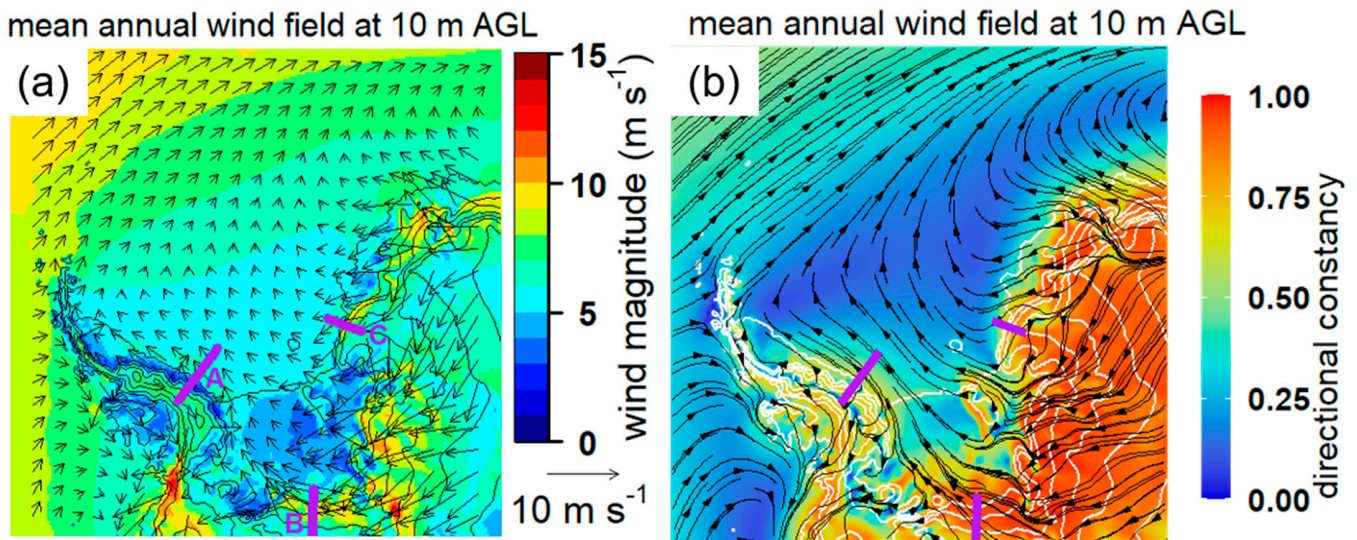


Figure 8. Mean wind field for 2002–2016 at 10 m. (a) Mean wind vector (at every 10th grid point) and wind speed, (b) directional constancy with streamlines. Topography is shown as black and white isolines every 500 m in (a) and (b), respectively. Cross-sections A, B and C are marked (see also Figure 1).

More insight into the wind field structure can be obtained by cross-sections. Here, we focus on the wintertime situation for three regions (marked in Figures 1 and 8 as A–C). For the katabatic wind region of Coats Land (Figure 9), the downslope wind component (along the cross-section) has values of more than 4 m/s only in a shallow layer above the surface (lowest 100 m). The across-slope wind component shows a low-level maximum of 9 m/s over the lower part of the slope. The potential temperature structure reflects the presence of an SBL over the slope. The mean wind speed shows an LLJ with a maximum of 12 m/s at about 200 m agl. This reflects that the katabatic wind is deflected to the left of the fall line by the Coriolis force (see Figure 8) and shows a vertical shear of the wind direction as the wind adjusts to the geostrophic balance with decreasing friction.

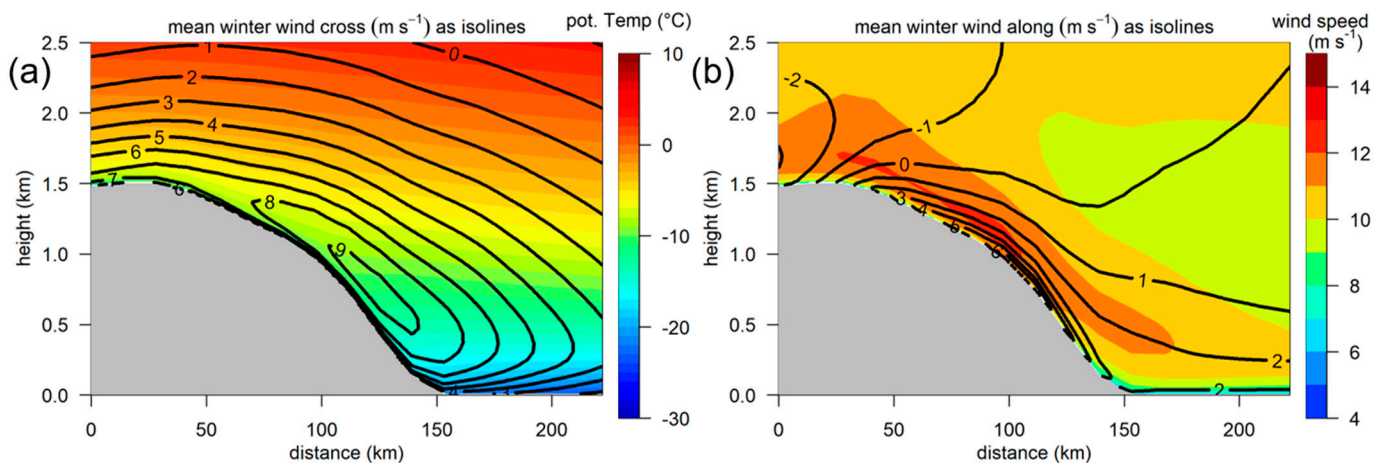


Figure 9. Cross-section C in the katabatic wind region over Coats Land (see Figures 1 and 8) for April–September 2002–2016 for (a) the crosswind component (isolines every 1 m/s) and the potential temperature (color scale) and (b) the along-wind (downslope) component (isolines every 1 m/s) and the mean wind speed (color scale).

Cross-section A (Figure 10) represents the barrier wind region at the eastern side of the Antarctic Peninsula. The crosswind (north) component (Figure 10a) shows the barrier wind with a southerly wind maximum of more than 7 m/s below 500 m agl. The potential temperature reflects the strong static stability. The mean wind speed (Figure 10b) shows

the barrier wind less well-defined with wind speeds of more than 11 m/s and a stronger maximum with more than 14 m/s near the top of the orography at the lee side of the mountains, which is associated with a strong westerly wind (along-wind component). Here, we see the impact of the flow over the mountain top generating downslope flow (as indicated also by the potential temperature structure over the upper part of the slope). It should be noted that the cross- and along-wind components are computed as means from all time steps, thus the magnitude of the mean wind vector is smaller than the mean wind speed.

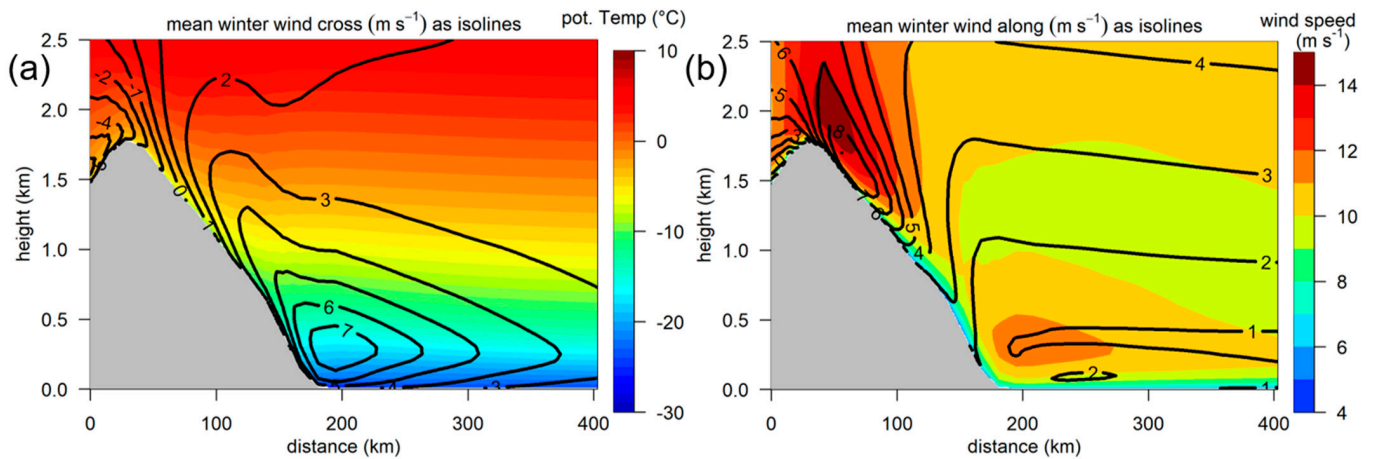


Figure 10. Cross-section A in the barrier wind region at the Antarctic Peninsula (see Figures 1 and 8) for April–September 2002–2016 for (a) the crosswind (north) component (isolines every 1 m/s) and the potential temperature (color scale) and (b) the along-wind (east) component (isolines every 1 m/s) and the mean wind speed (color scale).

Cross-section B (Figure 11) is located at the southern end of the FRIS. The wind field in the lowest 500 m is dominated by the crosswind component (Figure 11a), which shows a well-defined maximum at about 100 m agl. The mean wind speed is only slightly larger (Figure 11b). As for the katabatic wind of cross-section C the downslope wind component is much smaller (about 5 m/s) and is confined to a very shallow layer above the ground (Figure 11b). The field of the potential temperature structure shows the SBL over the slope.

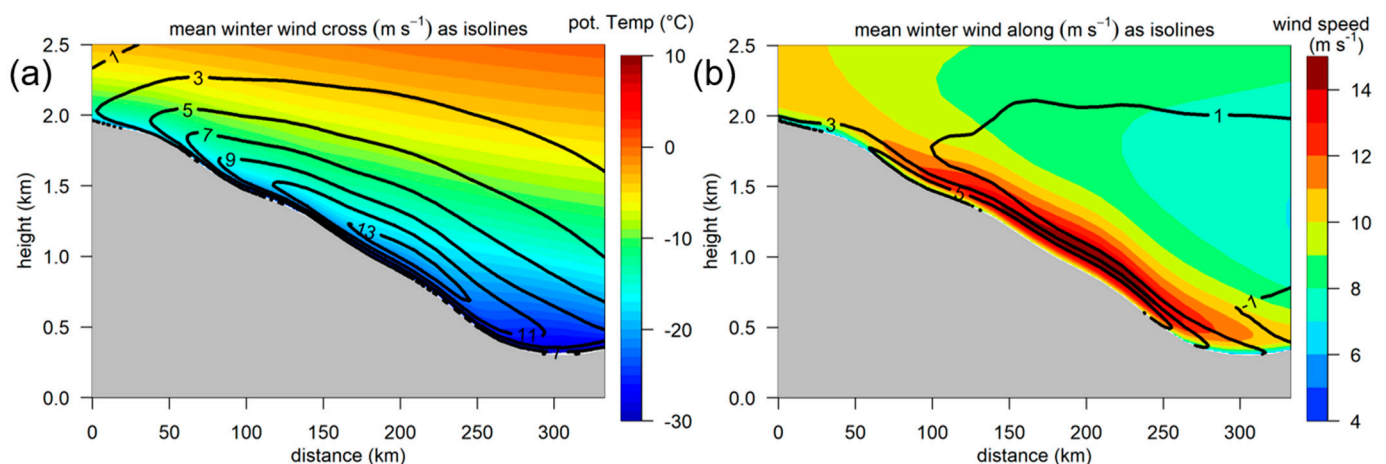


Figure 11. Cross-section B in the southern part of the FRIS (see Figures 1 and 8) for April–September 2002–2016 for (a) the crosswind component (isolines every 2 m/s) and the potential temperature (color scale) and (b) the along-wind (downslope) component (isolines every 2 m/s) and the mean wind speed (color scale).

3.3. Low-Level Jet Statistics

3.3.1. Comparison to Radiosonde Data

An extensive verification of CCLM simulations for the Antarctic with the same model data as used in the present study is shown by [31]. They conclude that the comparisons with the available radiosonde stations in the model area (see Figure 1) for 2002–2016 showed a wind speed bias close to 0 for the whole troposphere except for the lowest 2 km, where a slight positive bias of 2–3 m/s was found for stations near the Antarctic Peninsula (Marambio and Rothera), while the bias was smaller than 1 m/s for stations on ice shelves (Neumayer, Halley) and on the plateau (Amundsen-Scott).

The LLJ detection algorithm is applied to the radiosonde data from the five stations shown in Figure 1 and is compared to the results of the simulated profiles at the same position and time (Figure 12). Some problems were encountered concerning the radiosonde data availability, both in time and vertical levels (see Table 1).

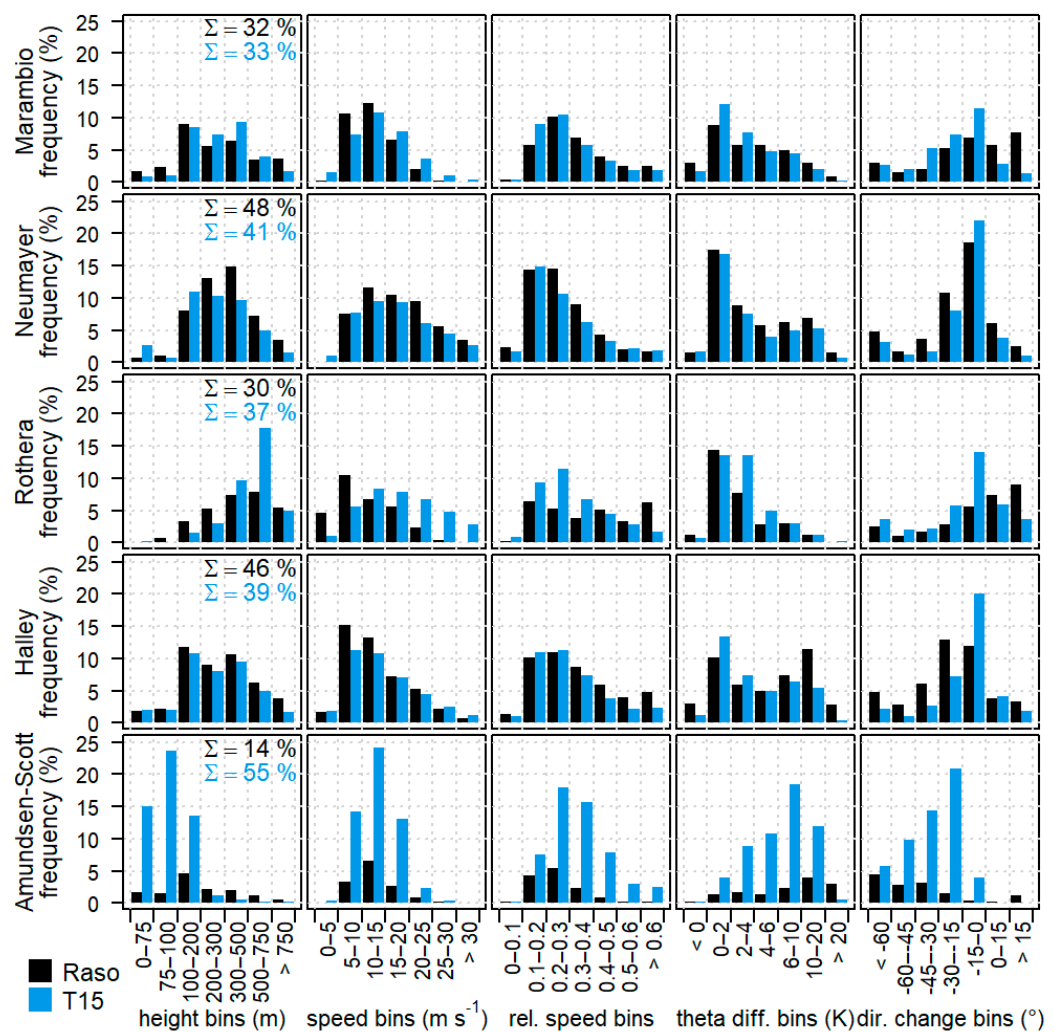


Figure 12. Distribution functions (absolute frequencies, total frequencies in the first column) of LLJ characteristics from radiosondes (black) and CCLM simulations (blue) for 2002–2016. The different radiosonde stations are in the rows, the columns show distribution functions of LLJ height (in m), LLJ speed (in m/s), the relative wind speed change within the search radius, the potential temperature difference between the jet height and the surface (in K), and the change of the wind direction (in °) between the jet height and 5 m. Note the unequal bin width of LLJ height and potential temperature difference.

Table 1. Availability of radiosonde data for 2002–2016 (see Figure 1).

Station	Profiles	Data Gaps	Remarks
Marambio	1364	2007–2008	Sparse data in 2002–2009
Neumayer	5355	no	
Rothera	1021	2008–2011	No data for 8 to 11 months per year in 2002–2012
Halley	4877	no	
Amundsen-Scott	7664	no	Vertical resolution in the lowest 500 m for 2002–2004 is too coarse to detect LLJs

Overall, there is good agreement except for the Amundsen-Scott station at the south pole. Here the number of LLJs with heights at about 100 m is much larger in the simulations than in the radiosonde data. Since only few LLJs have heights larger than 200 m, this has an impact on all distributions at that station. It is known that the wind profile from radiosondes is inaccurate for low levels, since the balloon has to adapt to the ambient wind speed, the wind field is disturbed by obstacles and buildings, and errors occur by the pendulum motion of the radiosonde, which is corrected by a low-pass filter, which results in a vertical resolution of 200 m [49]. The distributions of LLJ heights and speeds are almost identical for Neumayer and Halley, broader distributions are found in the simulations for Marambio and Rothera. The distributions of the relative wind speed change within the search radius show the problem of the choice of the relative criterion. Since the maxima lie between 0.1 and 0.3 (10–30%) for most stations, the application of a relative criterion of 25% as proposed by [44] will miss a large part of LLJs. This indicates that a value of 25% for this criterion seems to be too restrictive, particularly at very high wind speeds. The overall statistics for all LLJs detected in the CCLM and RS data sets are shown in Table 2. The bias for the jet height has reasonable values, if the height exceeds 200 m. The bias in speed is small except for Rothera, where the local topography influences on the wind field might not be adequately represented in the simulations with 15 km resolution.

Table 2. Statistics of LLJs from radiosonde (RS) and model data for 2002–2016 for all LLJs (mean values are given for CCLM data, bias is CCLM-RS).

Station	Frequency in %		Height in m		Speed in m/s		Rel. Speed Change in %	
	RS	CCLM	Mean	Bias	Mean	Bias	Mean	Bias
Marambio	32	33	315	−17	14.0	1.3	30	−4
Neumayer	48	41	286	−84	17.0	−1.1	27	0
Rothera	30	37	531	53	18.0	6.9	30	−12
Halley	46	39	291	−50	14.3	0.9	30	−5
Amundsen-Scott	14	55	102	−150	12.9	−0.3	33	7

All LLJs occur in SBL conditions for all stations. The potential temperature difference between at the jet height and the surface for the simulated and observed LLJs is similar for all stations except at the south pole. The change of the wind direction between the jet height and 5 m is mostly negative, although for Marambio and Rothera some LLJs have a positive change in wind direction. The bias towards negative values reflects that the change of the wind direction with height is consistent with the decreasing friction with height.

3.3.2. Climatology from Model Simulations

Figure 13 shows the LLJ frequency for 2002–2016 for the winter (April–September), the summer (December–January) and the annual average. The annual average is clearly dominated by the winter period. All months except December and January were found to

show similar LLJ frequencies. In summer (December–January), the katabatic wind shows a clear daily cycle and is much weaker compared to winter months. This reduces the LLJ frequency over the ice sheet from more than 80% in winter to less than 40% in summer.

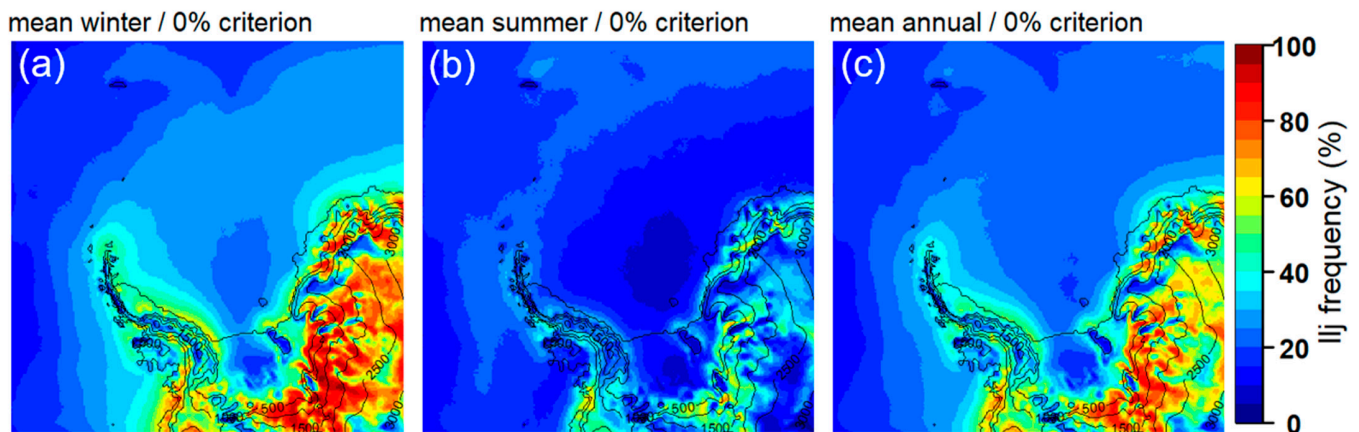


Figure 13. LLJ frequency for 2002–2016 for the winter (a), the summer (b,c) the annual average.

The winter average of the LLJ speed for 2002–2016 is shown in Figure 14a. This distribution has to be interpreted together with the frequency distribution (Figure 13a). The mean LLJ speed in the katabatic wind regime is about 15 m/s, but 20 m/s is also exceeded in some areas. The barrier wind regime, which has medium values of LLJ frequency, shows values of 15–20 m/s. The mean LLJ speed increases towards the northern Weddell Sea, but the LLJ frequency is below 30% in these areas. The inter monthly standard deviation of the LLJ speed (not shown) has a very high variability in regions with high sub-grid variance of the orography and in the coastal zone of the eastern Weddell Sea, where the wind field is dominated by cyclones moving from the northern Weddell Sea towards the Antarctic coast. The winter average of the LLJ height (Figure 14b) is generally below 150 m for the inland ice, and around 200–300 m over the sea ice. Plots for the summer and annual average (supplementary material Figure S8) show that the LLJs over the ice sheet are much weaker during summer.

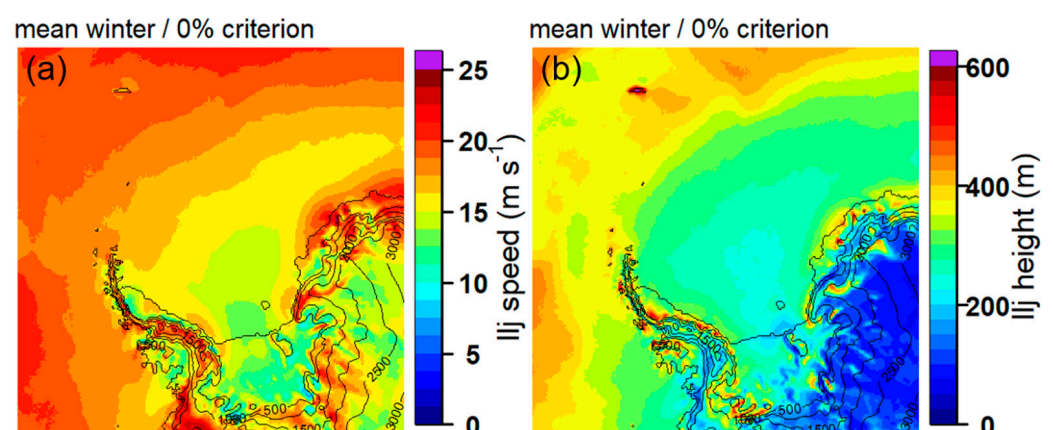


Figure 14. Winter (April–September) average of the (a) LLJ speed and (b) LLJ height for 2002–2016.

More insight into the statistics of LLJ characteristics can be obtained by looking at the distribution functions of hourly values of LLJ height and speed. Figure 15 shows these distributions for selected grid points over ocean/sea ice (point 1 in Figure 1) and inland ice (point 6 in Figure 1) for three different values of the relative criterium (0, 15 and 25%). Over the ocean area, the LLJ heights are distributed almost equally over all height ranges (Figure 15c). The speed distribution shows a very broad maximum and a large dependency

on the choice of the relative criterion (Figure 15a). For the katabatic wind regime, almost all LLJs are below 200 m (Figure 15d), while the speed distribution shows a clear maximum for 10–20 m/s and an asymmetric shape (Figure 15b). The choice of 0% or 15% for the relative criterion has only a small influence, but a value of 25% reduces the number of LLJs considerably. A plot summarizing the statistics for different subareas is shown in Figures S9 and S10 in the Supplementary Materials.

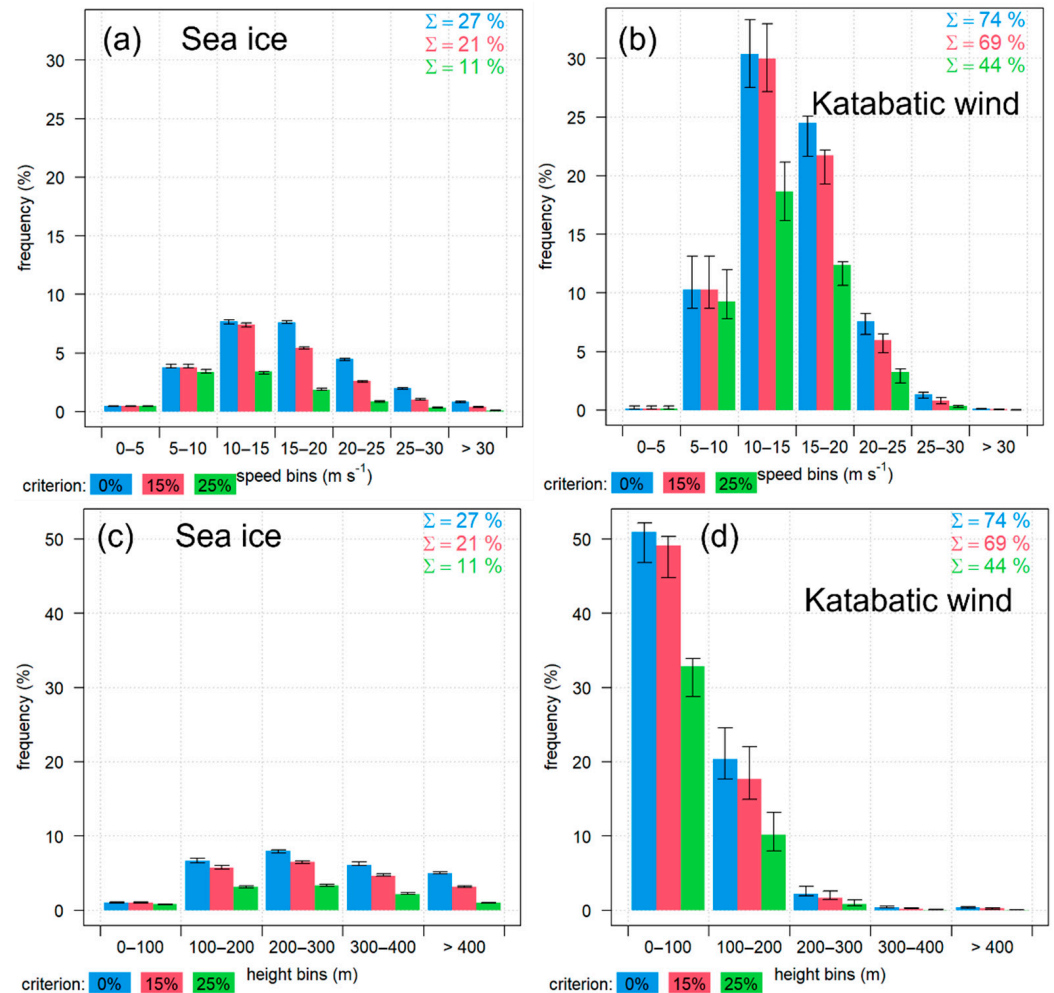


Figure 15. Distribution functions (absolute frequencies, total frequencies in the respective colors) of LLJ height and speed based on hourly values using different relative criteria (color bars) for winters 2002–2016 for location 1 (sea ice, (a,c)) and location 6 (inland ice, (b,d), see Figure 1 for positions). The whiskers indicate the maximum and minimum values for the surrounding 24 grid points. The overall frequencies for the different relative criteria are shown as numbers in the respective colors.

As further LLJ characteristics, we look at the duration of the LLJs. The statistics of the LLJ event durations is shown in Figure 16 for the selected points shown in Figure 1. A LLJ event is defined as the period where in consecutive profiles the LLJ criteria are fulfilled and the height of the LLJ shows no large jumps. As expected from the results presented above, there are more and longer LLJs in winter than in summer. These differences are small over the ocean/sea ice (OC), where there is only a slight increase in LLJs lasting more than one day. The same holds for LLJs over the FRIS (FR). The seasonal differences are most pronounced over the ice sheet (IS), where LLJs with a duration of more than 1 day occur frequently during winter. The barrier wind region at the Antarctic Peninsula (A) shows also an increase in the LLJ duration during winter, particularly for events with more than 24 h duration. At Coats Land (C), LLJs with less than 1 day duration dominate during winter and summer. For cross-section B in the southern part of the FRIS, the high

frequencies of LLJs are found in both seasons, and the fraction of LLJs with longer duration increases in winter. It has to be noted that the statistics of LLJ durations is sensitive to the relative criterion (see Figure S18 in the Supplementary Materials). When increasing the relative criterion, the length of LLJ events decreases and less LLJs lasting longer than 10 days are found over the ice sheet.

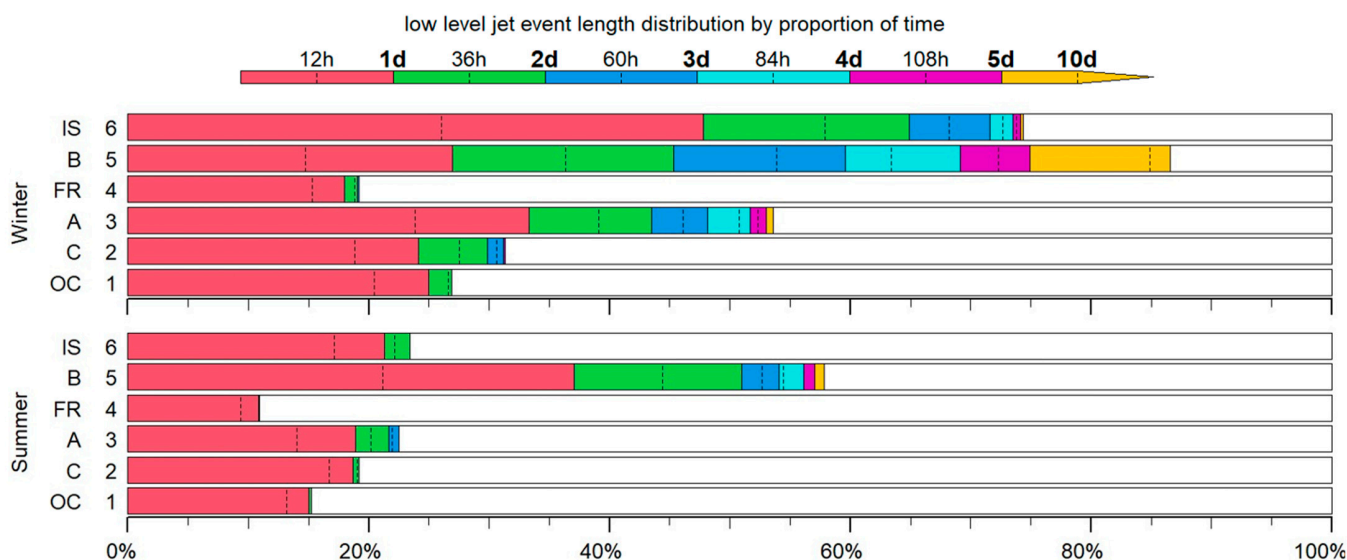


Figure 16. Distribution for the length of LLJ events (fraction of time of the respective LLJs events) for winter and summer 2002–2016 for the points 1–6 shown in Figure 1. Point 1 is located over the ocean (OC), points 2–4 are located in cross-sections A–C, point 5 is located over the central FRIS (FR) and point 6 is located over the ice sheet (IS). The colored bars represent the relative frequencies in 24 h bins, the value for 12 h is marked by a line inside the 24 h bin. For the last bin (yellow) the line marks 10 days.

The seasonal differences of the duration of events seem to be related to the daily cycle during summer, but also to generally weaker winds during summer compared to winter. For higher winds, it is more likely that the absolute LLJ criterion is exceeded more frequently and that the duration is longer. If the LLJ wind anomaly is less than 2 m/s for some period during the LLJ development, a long LLJ will be split into separate shorter events. The seasonality of the LLJ strength is most pronounced over the ice sheet, while it is relatively weak over the sea ice and ocean areas (see Figures 14 and S8). The duration of katabatic LLJs near the coast in the eastern Weddell Sea (cross-section C) is also influenced by the transient cyclones passing over the Weddell Sea or by mesocyclones developing near the coast [50].

The directional shear between the jet and the lowest model level (5 m) is negative in the average for all regions and seasons (not shown). This reflects that the change of the wind direction with height is consistent with the decreasing friction with height. The LLJ stability (difference between the potential temperature at the jet height and the surface) is shown in Figure 17 (boundary layer height and inversion statistics are presented in the Supplementary Materials, Figures S11–S17). While during winter the inversion frequency is higher than 90% over the inland ice, the FRIS and the sea ice (Figure S12), the inversion strength exceeds 15K only over the inland ice and the FRIS (Figure S14). This pattern is similar for the LLJ stability (Figure 17), and low values of stability correspond to high LLJ speeds (Figure 14), which reflects the strong mixing associated with the jets. This mixing seems to strongly affect the strength of the surface inversion (Figure S17). LLJs during summer are associated with relative weak surface inversions and LLJ stability (Figures 17 and S17).

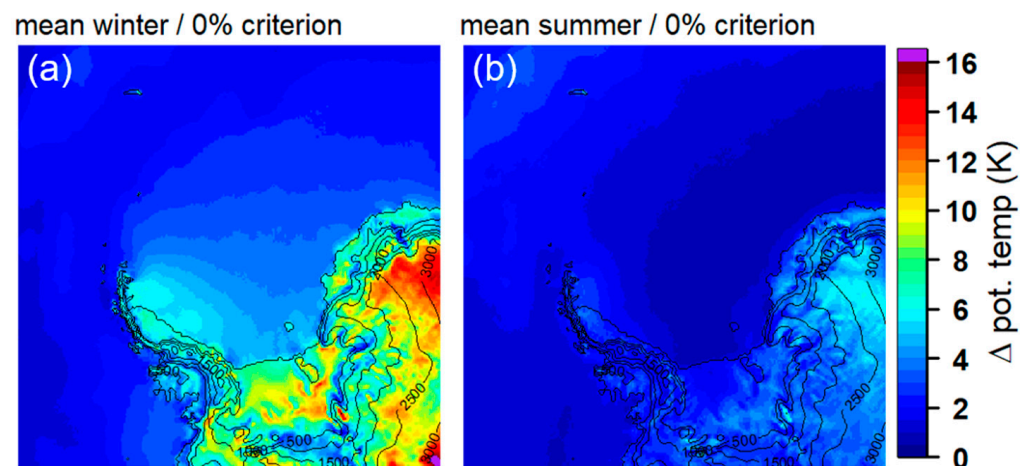


Figure 17. LLJ stability (difference between the potential temperature at the jet height and the surface for LLJ cases) for 2002–2016 for the winter (a), the summer (b).

4. Discussion

This study presents the first RCM-based climatology of LLJs for the Antarctic. It uses a similar approach as the model-based study of [44], who used reanalysis data with 30 km resolution for 11 years for the Arctic. Some findings of [44] are qualitatively similar to our results: highest frequencies of LLJs in katabatic wind regions (Greenland) and low frequency of LLJs over the sea ice of the central Arctic. Other findings associated with, e.g., tip jets at Greenland and topographic effects over Siberia cannot be compared to the Antarctic conditions.

The results of the present study have shown that the SSO parameterization has a distinct effect on the wind field and LLJ statistics over the inland ice. The SSO scheme was introduced in CCLM in order to describe the momentum drag in mountain areas more realistically [41]. Ref. [51] propose a modification of the SSO scheme for the SBL by applying the scheme only for model grid cells where the boundary layer height is two times larger than the SSO standard deviation. Although the SBL height in the katabatic wind is typically smaller than 300 m (see Figure S11 in the Supplementary Materials), this modification would reduce the SSO effects over the ice sheet only for a few grid points, since the SSO standard deviation is generally smaller than 40 m. While the first published simulations of the near-surface wind over the ice sheet showed a very smooth wind field structure [52], recent simulations show a more detailed structure due to the consideration of topographic grid-scale and sub-grid scale (e.g., [30]).

Cross-sections for katabatic wind regions show similar structures as found by [30]. Due to the horizontal temperature gradient caused by the sloped inversion in the katabatic SBL, downslope winds are found only close to the surface and the wind turns to directions perpendicular to the slope within a few hundred meters. Barrier winds at the Antarctic Peninsula were mainly described for the near-surface wind in previous studies [16,24,53], in our study we can show that they are associated with a clear wind maximum at about 300 m in the winter climatology, and that they are associated with strong LLJs for more than half the time during the winter months.

The sensitivity of the results to the criteria to identify LLJs is an important issue for SBL studies in polar regions. While the absolute criterion of 2 m/s for the LLJ wind anomaly is generally used [5,6,54,55], the relative criterion of the wind speed decrease above the wind maximum introduced by [54] and used in [44] can affect the results of an LLJ climatology. We find that the value of 25% of the relative criterion used in [44,54] is too restrictive, and we propose to use only the absolute criterion for model studies. The sensitivity of the results to this criterion is different for different regions. It has larger effects for the LLJ frequency over sea ice than for the katabatic LLJs. In contrast, the length of katabatic LLJ events shows a large sensitivity with respect to the relative criterion. If the

LLJ wind anomaly gets less pronounced for some period during the LLJ development, a long LLJ will be split into two separate shorter events. This effect may explain a large part of the sensitivity.

In order to simulate SBL features as LLJs and surface inversions, adequate horizontal and vertical resolutions are necessary. Very shallow LLJs with heights below 35 m as observed at Dome C by [14] are hardly simulated with the vertical resolution used in our study, where the lowest model levels are at 5, 16 and 27 m. However, most of the LLJs shown by [14] were weak and would likely not pass the absolute criterion of LLJs. For typical katabatic winds over the ice sheet, the used vertical resolution with 10 levels below 300 m is sufficient to resolve katabatic LLJs. The horizontal resolution is important in areas with small-scale structures of the topography such as the Antarctic Peninsula. A long-term comparison (2002–2016) of CCLM simulations with 15 and 5 km resolution by [31] for the Weddell Sea region shows only small differences between these resolutions for the ice sheet and the ocean/sea ice areas. A comparison between CCLM simulations at different resolutions (15, 5 and 2 km) as well as ERA-Interim and ERA5 re-analyses (80 km and 30 km horizontal resolution, respectively) is shown in Figure 18 for the area of the Larsen Ice Shelf for July 2016 for the 10 m-wind. The re-analyses are not able to account for the topographic effects of katabatic winds and foehn in that region. With 15 km resolution, these effects are simulated but underestimated. This is in accordance with the findings of [56,57], who concluded that foehn effects over Larsen-C Ice Shelf are best represented for a model with 1.5 km resolution. However, simulations with a kilometer scale resolution are not feasible for larger domains over a long period.

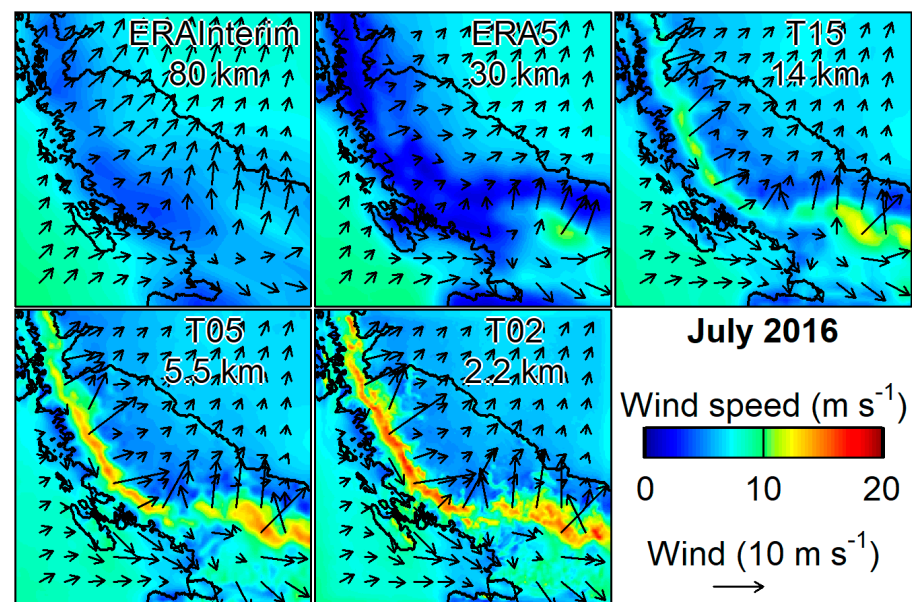


Figure 18. Mean 10 m-wind for July 2016 for the region of the Larsen-C Ice Shelf for ERA-Interim, ERA5, and CCLM with different resolutions (vectors selected on the ERA-Interim resolution).

The LLJ characteristics show only little interannual variation (see Figure S19 in the Supplementary Materials). As a future research direction, the methodology of this paper is planned to be applied to the investigation of LLJ characteristics during climate change. CCLM simulations for climate change scenarios for the whole Antarctic are currently performed and evaluated.

Supplementary Materials: The following are available online at <https://www.mdpi.com/article/10.3390/atmos12121635/s1>, Figure S1: Mean inversion height during winter (April–September) for 2002–2016 for different thresholds of the gradient of the potential temperature. Figure S2: Mean annual wind at 100 m. Figure S3: Mean annual wind at 200 m. Figure S4: Mean annual wind at 500 m. Figure S5: Mean wind at 10 m for summer. Figure S6: Mean wind at 10 m for winter. Figure S7: Mean

wind at 200 and 500 m for winter. Figure S8: Mean LLJ wind speed and LLJ height for summer and the whole year. Figure S9: Distribution of LLJ wind speed for the whole year for different regions. Figure S10: Distribution of LLJ height for the whole year for different regions. Figure S11: Height of the boundary layer for (a) winter, (b) summer and (c) the whole year. Figure S12: Inversion frequency for winter, summer and the whole year. Figure S13: Inversion height for winter, summer and the whole year. Figure S14: Inversion strength for winter, summer and the whole year. Figure S15: Frequency of surface inversions for winter, summer and the whole year. Figure S16: Height of surface inversions for winter, summer and the whole year. Figure S17: Strength of surface inversions for winter, summer and the whole year. Figure S18: Length of LLJ events for 0%, 15% and 25% relative criteria for the whole year for the points 1–6 shown in Figure 1. Figure S19. Time series of LLJ speed and frequency for annual means for 0%, 15% and 25% relative criteria for the points 1–6 shown in Figure 1.

Author Contributions: Conceptualization, G.H. and R.Z.; methodology, G.H.; software, R.Z.; formal analysis, R.Z.; data curation, R.Z.; writing—original draft preparation, G.H.; writing—review and editing, G.H. and R.Z.; visualization, R.Z.; supervision, G.H.; project administration, G.H.; funding acquisition, G.H. All authors have read and agreed to the published version of the manuscript.

Funding: This research was funded by the SPP 1158 “Antarctic research” of the DFG (Deutsche Forschungsgemeinschaft) under grant HE 2740/33. The publication was funded by the Open Access Fund of Universität Trier and the DFG within the Open Access Publishing funding programme.

Institutional Review Board Statement: Not applicable.

Informed Consent Statement: Not applicable.

Data Availability Statement: Annual and seasonal fields of LLJ frequencies, near-surface wind field and inversion statistics data will be made available on PANGAEA.

Acknowledgments: Thanks go to the CLM Community and the German Meteorological Service for providing the basic COSMO-CLM model. This work used resources of the Deutsches Klimarechenzentrum (DKRZ) granted by its Scientific Steering Committee (WLA) under project ID bb0958.

Conflicts of Interest: The authors declare no conflict of interest. The funders had no role in the design of the study; in the collection, analyses, or interpretation of data; in the writing of the manuscript, or in the decision to publish the results.

References

1. Gorodetskaya, I.V.; Tsukernik, M.; Claes, K.; Ralph, M.F.; Neff, W.D.; van Lipzig, N.P.M. The role of atmospheric rivers in anomalous snow accumulation in East Antarctica. *Geophys. Res. Lett.* **2014**, *41*, 6199–6206. [[CrossRef](#)]
2. Zentek, R.; Kohnemann, S.H.E.; Heinemann, G. Analysis of the performance of a ship-borne scanning wind lidar in the Arctic and Antarctic. *Atmos. Meas. Tech.* **2018**, *11*, 5781–5795. [[CrossRef](#)]
3. Guest, P.; Persson, P.O.G.; Wang, S.; Jordan, M.; Jin, Y.; Blomquist, B.; Fairall, C. Low-Level Baroclinic Jets Over the New Arctic Ocean. *J. Geophys. Res. Oceans* **2018**, *123*, 4074–4091. [[CrossRef](#)]
4. Jakobson, L.; Vihma, T.; Jakobson, E.; Palo, T.; Männik, A.; Jaagus, J. Low-level jet characteristics over the Arctic Ocean in spring and summer. *Atmos. Chem. Phys.* **2013**, *13*, 11089–11099. [[CrossRef](#)]
5. Heinemann, G.; Drüe, C.; Schwarz, P.; Makshtas, A. Observations of Wintertime Low-Level Jets in the Coastal Region of the Laptev Sea in the Siberian Arctic Using SODAR/RASS. *Remote Sens.* **2021**, *13*, 1421. [[CrossRef](#)]
6. Andreas, E.L.; Claffy, K.J.; Makshtas, A.P. Low-Level Atmospheric Jets and Inversions over the Western Weddell Sea. *Bound.-Layer Meteorol.* **2000**, *97*, 459–486. [[CrossRef](#)]
7. Heinemann, G.; Rose, L. Surface energy balance, parameterizations of boundary-layer heights and the application of resistance laws near an Antarctic Ice Shelf front. *Bound.-Layer Meteorol.* **1990**, *51*, 123–158. [[CrossRef](#)]
8. Heinemann, G. Aircraft-Based Measurements Of Turbulence Structures In The Katabatic Flow Over Greenland. *Bound.-Layer Meteorol.* **2002**, *103*, 49–81. [[CrossRef](#)]
9. Heinemann, G. The KABEG’97 field experiment: An aircraft-based study of katabatic wind dynamics over the Greenland ice sheet. *Bound.-Layer Meteorol.* **1999**, *93*, 75–116. [[CrossRef](#)]
10. Renfrew, I.A.; Anderson, P.S. Profiles of katabatic flow in summer and winter over Coats Land, Antarctica. *Q. J. R. Meteorol. Soc.* **2006**, *132*, 779–802. [[CrossRef](#)]
11. Wendler, G. Strong gravity flow observed along the slope of Eastern Antarctica. *Meteorol. Atmos. Phys.* **1990**, *43*, 127–135. [[CrossRef](#)]
12. Loewe, F. The land of storms. *Weather* **1972**, *27*, 110–121. [[CrossRef](#)]
13. Kodama, Y.; Wendler, G.; Ishikawa, N. The Diurnal Variation of the Boundary Layer in Summer in Adelie Land, Eastern Antarctica. *J. Appl. Meteor.* **1989**, *28*, 16–24. [[CrossRef](#)]

14. Gallée, H.; Barral, H.; Vignon, E.; Genthon, C. A case study of a low-level jet during OPALE. *Atmos. Chem. Phys.* **2015**, *15*, 6237–6246. [[CrossRef](#)]
15. Vignon, É.; Traullé, O.; Berne, A. On the fine vertical structure of the low troposphere over the coastal margins of East Antarctica. *Atmos. Chem. Phys.* **2019**, *19*, 4659–4683. [[CrossRef](#)]
16. Schwerdtfeger, W. Meteorological aspects of the drift of ice from the Weddell Sea toward the mid-latitude westerlies. *J. Geophys. Res.* **1979**, *84*, 6321. [[CrossRef](#)]
17. Nigro, M.A.; Cassano, J.J.; Lazzara, M.A.; Keller, L.M. Case Study of a Barrier Wind Corner Jet off the Coast of the Prince Olav Mountains, Antarctica. *Mon. Weather Rev.* **2012**, *140*, 2044–2063. [[CrossRef](#)]
18. O'Connor, W.P.; Bromwich, D.H.; Carrasco, J.F. Cyclonically Forced Barrier Winds along the Transantarctic Mountains near Ross Island. *Mon. Weather Rev.* **1994**, *122*, 137–150. [[CrossRef](#)]
19. Elvidge, A.D.; Renfrew, I.A.; King, J.C.; Orr, A.; Lachlan-Cope, T.A.; Weeks, M.; Gray, S.L. Foehn jets over the Larsen C Ice Shelf, Antarctica. *Q. J. R. Meteorol. Soc.* **2015**, *141*, 698–713. [[CrossRef](#)]
20. Orr, A.; Kirchgassner, A.; King, J.; Phillips, T.; Gilbert, E.; Elvidge, A.; Weeks, M.; Gadian, A.; Kuipers Munneke, P.; Broeke, M.; et al. Comparison of kilometre and sub-kilometre scale simulations of a foehn wind event over the Larsen C Ice Shelf, Antarctic Peninsula using the Met Office Unified Model (MetUM). *Q. J. R. Meteorol. Soc.* **2021**, *147*, 3472–3492. [[CrossRef](#)]
21. KING, J.C.; Lachlan-Cope, T.A.; Ladkin, R.S.; Weiss, A. Airborne Measurements in the Stable Boundary Layer over the Larsen Ice Shelf, Antarctica. *Bound.-Layer Meteorol.* **2008**, *127*, 413–428. [[CrossRef](#)]
22. Seefeldt, M.W.; Cassano, J.J. An Analysis of Low-Level Jets in the Greater Ross Ice Shelf Region Based on Numerical Simulations. *Mon. Weather Rev.* **2008**, *136*, 4188–4205. [[CrossRef](#)]
23. Parish, T.R.; Bromwich, D.H. Reexamination of the Near-Surface Airflow over the Antarctic Continent and Implications on Atmospheric Circulations at High Southern Latitudes. *Mon. Weather Rev.* **2007**, *135*, 1961–1973. [[CrossRef](#)]
24. Ebner, L.; Heinemann, G.; Haid, V.; Timmermann, R. Katabatic winds and polynya dynamics at Coats Land, Antarctica. *Antarct. Sci.* **2014**, *26*, 309–326. [[CrossRef](#)]
25. Tastula, E.-M.; Vihma, T.; Andreas, E.L. Evaluation of Polar WRF from Modeling the Atmospheric Boundary Layer over Antarctic Sea Ice in Autumn and Winter. *Mon. Weather Rev.* **2012**, *140*, 3919–3935. [[CrossRef](#)]
26. Van Lipzig, N.P.M.; Turner, J.; Colwell, S.R.; van den Broeke, M.R. The near-surface wind field over the Antarctic continent. *Int. J. Climatol.* **2004**, *24*, 1973–1982. [[CrossRef](#)]
27. Souverijns, N.; Gossart, A.; Demuzere, M.; Lenaerts, J.T.M.; Medley, B.; Gorodetskaya, I.V.; Vanden Broucke, S.; van Lipzig, N.P.M. A New Regional Climate Model for POLAR-CORDEX: Evaluation of a 30-Year Hindcast with COSMO-CLM 2 over Antarctica. *J. Geophys. Res.* **2019**, *124*, 1405–1427. [[CrossRef](#)]
28. Van Wessem, J.M.; van de Berg, W.J.; Noël, B.P.Y.; van Meijgaard, E.; Amory, C.; Birnbaum, G.; Jakobs, C.L.; Krüger, K.; Lenaerts, J.T.M.; Lhermitte, S.; et al. Modelling the climate and surface mass balance of polar ice sheets using RACMO2—Part 2: Antarctica (1979–2016). *Cryosphere* **2018**, *12*, 1479–1498. [[CrossRef](#)]
29. Lenaerts, J.T.M.; Vizcaino, M.; Fyke, J.; van Kampenhout, L.; van den Broeke, M.R. Present-day and future Antarctic ice sheet climate and surface mass balance in the Community Earth System Model. *Clim. Dyn.* **2016**, *47*, 1367–1381. [[CrossRef](#)]
30. Van de Berg, W.J.; van den Broeke, M.R.; van Meijgaard, E. Heat budget of the East Antarctic lower atmosphere derived from a regional atmospheric climate model. *J. Geophys. Res.* **2007**, *112*. [[CrossRef](#)]
31. Zentek, R.; Heinemann, G. Verification of the regional atmospheric model CCLM v5.0 with conventional data and lidar measurements in Antarctica. *Geosci. Model Dev.* **2020**, *13*, 1809–1825. [[CrossRef](#)]
32. Kohnemann, S.H.E.; Heinemann, G.; Bromwich, D.H.; Gutjahr, O. Extreme Warming in the Kara Sea and Barents Sea during the Winter Period 2000–16. *J. Clim.* **2017**, *30*, 8913–8927. [[CrossRef](#)]
33. Kohnemann, S.H.; Heinemann, G. A climatology of wintertime low-level jets in Nares Strait. *POLAR* **2021**, *40*. [[CrossRef](#)]
34. Heinemann, G. Assessment of Regional Climate Model Simulations of the Katabatic Boundary Layer Structure over Greenland. *Atmosphere* **2020**, *11*, 571. [[CrossRef](#)]
35. Gutjahr, O.; Heinemann, G.; Preußner, A.; Willmes, S.; Drüe, C. Quantification of ice production in Laptev Sea polynyas and its sensitivity to thin-ice parameterizations in a regional climate model. *Cryosphere* **2016**, *10*, 2999–3019. [[CrossRef](#)]
36. Dee, D.P.; Uppala, S.M.; Simmons, A.J.; Berrisford, P.; Poli, P.; Kobayashi, S.; Andrae, U.; Balmaseda, M.A.; Balsamo, G.; Bauer, P.; et al. The ERA-Interim reanalysis: Configuration and performance of the data assimilation system. *Q. J. R. Meteorol. Soc.* **2011**, *137*, 553–597. [[CrossRef](#)]
37. Schröder, D.; Heinemann, G.; Willmes, S. The impact of a thermodynamic sea-ice module in the COSMO numerical weather prediction model on simulations for the Laptev Sea, Siberian Arctic. *Polar Res.* **2011**, *30*, 6334. [[CrossRef](#)]
38. Spreen, G.; Kaleschke, L.; Heygster, G. Sea ice remote sensing using AMSR-E 89-GHz channels. *J. Geophys. Res.* **2008**, *113*, 14485. [[CrossRef](#)]
39. Kurtz, N.T.; Markus, T. Satellite observations of Antarctic sea ice thickness and volume. *J. Geophys. Res.* **2012**, *117*. [[CrossRef](#)]
40. Schaffer, J.; Timmermann, R.; Arndt, J.E.; Kristensen, S.S.; Mayer, C.; Morlighem, M.; Steinhage, D. A global, high-resolution data set of ice sheet topography, cavity geometry, and ocean bathymetry. *Earth Syst. Sci. Data* **2016**, *8*, 543–557. [[CrossRef](#)]
41. Doms, G.; Förstner, J.; Heise, H.; Herzog, H.-J.; Mironov, D.; Raschendorfer, M.; Reinhardt, T.; Ritter, B.; Schrodin, R.; Schulz, J.-P.; et al. *A Description of the Nonhydrostatic Regional COSMO-Model. Part II. Physical Parameterizations*; Deutscher Wetterdienst: Offenbach, Germany, 2013.

42. Lott, F.; Miller, M.J. A new subgrid-scale orographic drag parametrization: Its formulation and testing. *Q. J. R. Meteorol. Soc.* **1997**, *123*, 101–127. [[CrossRef](#)]
43. Zentek, R. COSMO Documentation (Archived Version from 2019, Uploaded with Permission of the DWD). 2019. Available online: <https://zenodo.org/record/3339384> (accessed on 7 May 2021).
44. Tuononen, M.; Sinclair, V.A.; Vihma, T. A climatology of low-level jets in the mid-latitudes and polar regions of the Northern Hemisphere. *Atmos. Sci. Lett.* **2015**, *16*, 492–499. [[CrossRef](#)]
45. Wetzell, P.J. Toward Parameterization of the Stable Boundary Layer. *J. Appl. Meteor.* **1982**, *21*, 7–13. [[CrossRef](#)]
46. Vogelesang, D.H.P.; Holtslag, A.A.M. Evaluation and model impacts of alternative boundary-layer height formulations. *Bound.-Layer Meteorol.* **1996**, *81*, 245–269. [[CrossRef](#)]
47. Heinemann, G. An Aircraft-Based Study of Strong Gap Flows in Nares Strait, Greenland. *Mon. Weather Rev.* **2018**, *146*, 3589–3604. [[CrossRef](#)]
48. Heinemann, G.; Klein, T. Modelling and observations of the katabatic flow dynamics over Greenland. *Tellus A* **2002**, *54*, 542–554. [[CrossRef](#)]
49. Dirksen, R.J.; Sommer, M.; Immler, F.J.; Hurst, D.F.; Kivi, R.; Vömel, H. Reference quality upper-air measurements: GRUAN data processing for the Vaisala RS92 radiosonde. *Atmos. Meas. Tech.* **2014**, *7*, 4463–4490. [[CrossRef](#)]
50. Heinemann, G. Mesoscale Vortices in the Weddell Sea Region (Antarctica). *Mon. Weather Rev.* **1990**, *118*, 779–793. [[CrossRef](#)]
51. Tsiringakis, A.; Steeneveld, G.J.; Holtslag, A.A.M. Small-scale orographic gravity wave drag in stable boundary layers and its impact on synoptic systems and near-surface meteorology. *Q. J. R. Meteorol. Soc.* **2017**, *143*, 1504–1516. [[CrossRef](#)]
52. Parish, T.R.; Bromwich, D.H. Continental-Scale Simulation of the Antarctic Katabatic Wind Regime. *J. Clim.* **1991**, *4*, 135–146. [[CrossRef](#)]
53. Van Wessem, J.M.; Reijmer, C.H.; van de Berg, W.J.; van den Broeke, M.R.; Cook, A.J.; van Uft, L.H.; van Meijgaard, E. Temperature and Wind Climate of the Antarctic Peninsula as Simulated by a High-Resolution Regional Atmospheric Climate Model. *J. Clim.* **2015**, *28*, 7306–7326. [[CrossRef](#)]
54. Baas, P.; Bosveld, F.C.; Klein Baltink, H.; Holtslag, A.A.M. A Climatology of Nocturnal Low-Level Jets at Cabauw. *J. Appl. Meteor. Climatol.* **2009**, *48*, 1627–1642. [[CrossRef](#)]
55. Karipot, A.; Leclerc, M.Y.; Zhang, G. Characteristics of Nocturnal Low-Level Jets Observed in the North Florida Area. *Mon. Weather Rev.* **2009**, *137*, 2605–2621. [[CrossRef](#)]
56. Elvidge, A.D.; Renfrew, I.A.; King, J.C.; Orr, A.; Lachlan-Cope, T.A. Foehn warming distributions in nonlinear and linear flow regimes: A focus on the Antarctic Peninsula. *Q. J. R. Meteorol. Soc.* **2016**, *142*, 618–631. [[CrossRef](#)]
57. Turton, J.V.; Kirchgässner, A.; Ross, A.N.; King, J.C. Does high-resolution modelling improve the spatial analysis of föhn flow over the Larsen C Ice Shelf? *Weather* **2017**, *72*, 192–196. [[CrossRef](#)]

Acknowledgements

First and foremost, I want to thank my supervisor Günther Heinemann. His guidance and knowledge helped me along the whole way and his ongoing support allowed me see it through.

Secondly, I appreciate all the helpful contact, discussions and insights with my local, national and international colleagues - especially Lukas Schefczyk and Svenja Kohnemann, who worked with me for hours, weeks, months and years.

At last but not least, a thanks goes to all the people that could be considered causally responsible for me sitting here as the person I am today (and also to everyone who helped with the proofreading).

This research was funded by the SPP 1158 “Antarctic research” of the DFG (Deutsche Forschungsgemeinschaft) under grant HE 2740/19 and 2740/33. The publications were funded by the Open Access Fund of Universität Trier and the DFG within the Open Access Publishing funding programme. The Polarstern cruise PS96 was funded by the Alfred-Wegener-Institut under Polarstern grant AWI_PS96_03. This work used resources of the Deutsches Klimarechenzentrum (DKRZ) granted by its Scientific Steering Committee (WLA) under project ID bb0958. The basic COSMO-CLM model was provided by the CLM Community and the German Meteorological Service. Hersbach et al. [2019] was downloaded from the Copernicus Climate Change Service (C3S) Climate Data Store. The results contain modified Copernicus Climate Change Service information 2023. Neither the European Commission nor ECMWF is responsible for any use that may be made of the Copernicus information or data it contains.

Bibliography

- B. J. Abiodun, J. M. Prusa, and W. J. Gutowski. Implementation of a non-hydrostatic, adaptive-grid dynamics core in CAM3. Part I: comparison of dynamics cores in aqua-planet simulations. *Climate Dynamics*, 31(7-8):795–810, 2008. doi: 10.1007/s00382-008-0381-y.
- P. Achtert, I. M. Brooks, B. J. Brooks, B. I. Moat, J. Prytherch, P. O. G. Persson, and M. Tjernström. Measurement of wind profiles by motion-stabilised ship-borne Doppler lidar. *Atmospheric Measurement Techniques*, 8(11):4993–5007, 2015. doi: 10.5194/amt-8-4993-2015.
- C. Agosta, C. Amory, C. Kittel, A. Orsi, V. Favier, H. Gallée, M. R. van den Broeke, J. T. M. Lenaerts, J. M. van Wessem, W. J. van de Berg, and X. Fettweis. Estimation of the Antarctic surface mass balance using the regional climate model MAR (1979–2015) and identification of dominant processes. *The Cryosphere*, 13(1):281–296, 2019. doi: 10.5194/tc-13-281-2019.
- C. Alexander. *Die Endurance*. 2007. Berliner Taschenbuch Verlag.
- E. L. Andreas, K. J. Claffy, and A. P. Makshtas. Low-level atmospheric jets and inversions over the western Weddell Sea. *Boundary-Layer Meteorology*, 97(3):459–486, 2000. doi: 10.1023/a:1002793831076.
- P. Baas, F. C. Bosveld, H. K. Baltink, and A. A. M. Holtslag. A climatology of nocturnal low-level jets at Cabauw. *Journal of Applied Meteorology and Climatology*, 48(8):1627–1642, 2009. doi: 10.1175/2009jamc1965.1.
- F. K. Ball. The katabatic winds of Adélie Land and King George V Land. *Tellus*, 9(2): 201–208, 1957. doi: 10.1111/j.2153-3490.1957.tb01874.x.
- R. Banta, R. K. Newsom, J. K. Lundquist, Y. L. Pichugina, R. L. Coulter, and L. Mahrt. Nocturnal low-level jet characteristics over Kansas during Cases-99. *Boundary-Layer Meteorology*, 105(2):221–252, 2002. doi: 10.1023/a:1019992330866.
- D. Bozkurt, D. H. Bromwich, J. Carrasco, K. M. Hines, J. C. Maureira, and R. Rondanelli. Recent near-surface temperature trends in the Antarctic Peninsula from observed, reanalysis and regional climate model data. *Advances in Atmospheric Sciences*, 37(5):477–493, 2020. doi: 10.1007/s00376-020-9183-x.
- D. H. Bromwich, F. O. Otieno, K. M. Hines, K. W. Manning, and E. Shilo. Comprehensive evaluation of polar weather research and forecasting model performance in the Antarctic.

- Journal of Geophysical Research: Atmospheres*, 118(2):274–292, 2013. doi: 10.1029/2012jd018139.
- D. H. Bromwich, K. Werner, B. Casati, J. G. Powers, I. V. Gorodetskaya, F. Massonnet, V. Vitale, V. J. Heinrich, D. Liggett, S. Arndt, B. Barja, E. Bazile, S. Carpentier, J. F. Carrasco, T. Choi, Y. Choi, S. R. Colwell, R. R. Cordero, M. Gervasi, T. Haiden, N. Hirasawa, J. Inoue, T. Jung, H. Kalesse, S.-J. Kim, M. A. Lazzara, K. W. Manning, K. Norris, S.-J. Park, P. Reid, I. Rigor, P. M. Rowe, H. Schmithüsen, P. Seifert, Q. Sun, T. Uttal, M. Zannoni, and X. Zou. The year of polar prediction in the southern hemisphere (YOPP-SH). *Bulletin of the American Meteorological Society*, 101(10):E1653–E1676, 2020. doi: 10.1175/bams-d-19-0255.1.
- D. H. Bromwich, M. A. Lazzara, A. M. Cayette, J. G. Powers, K. Werner, J. J. Cassano, S. R. Colwell, S. Carpentier, and X. Zou. The 16th workshop on Antarctic meteorology and climate and 6th year of polar prediction in the southern hemisphere meeting. *Advances in Atmospheric Sciences*, 39(3):536–542, 2022. doi: 10.1007/s00376-021-1384-4.
- E. Buchignani and P. Mercogliano. Performance evaluation of high-resolution simulations with COSMO over south Italy. *Atmosphere*, 12(1):45, dec 2020. doi: 10.3390/atmos12010045.
- R. Calhoun, R. Heap, M. Princevac, R. Newsom, H. Fernando, and D. Ligon. Virtual towers using coherent doppler lidar during the joint urban 2003 dispersion experiment. *Journal of Applied Meteorology and Climatology*, 45(8):1116–1126, 2006. doi: 10.1175/jam2391.1.
- J. Carter, A. Leeson, A. Orr, C. Kittel, and J. M. van Wessem. Variability in Antarctic surface climatology across regional climate models and reanalysis datasets. *The Cryosphere*, 16(9):3815–3841, 2022. doi: 10.5194/tc-16-3815-2022.
- Y. Chen, K. Simon, and J. Behrens. Extending legacy climate models by adaptive mesh refinement for single-component tracer transport: a case study with ECHAM6-HAMMOZ (ECHAM6.3-HAM2.3-MOZ1.0). *Geoscientific Model Development*, 14(5):2289–2316, 2021. doi: 10.5194/gmd-14-2289-2021.
- T. Damian, A. Wieser, K. Träumner, U. Corsmeier, and C. Kottmeier. Nocturnal low-level jet evolution in a broad valley observed by dual Doppler lidar. *Meteorologische Zeitschrift*, 23(3):305–313, 2014. doi: 10.1127/0941-2948/2014/0543.
- R. T. Datta, M. Tedesco, X. Fettweis, C. Agosta, S. Lhermitte, J. T. M. Lenaerts, and N. Wever. The effect of foehn-induced surface melt on firn evolution over the northeast Antarctic Peninsula. *Geophysical Research Letters*, 46(7):3822–3831, 2019. doi: 10.1029/2018gl080845.
- H. C. Davies and R. E. Turner. Updating prediction models by dynamical relaxation: an examination of the technique. *Quarterly Journal of the Royal Meteorological Society*, 103(436):225–245, 1977. doi: 10.1002/qj.49710343602.

- P. Deb, A. Orr, D. H. Bromwich, J. P. Nicolas, J. Turner, and J. S. Hosking. Summer drivers of atmospheric variability affecting ice shelf thinning in the Amundsen Sea embayment, West Antarctica. *Geophysical Research Letters*, 45(9):4124–4133, 2018. doi: 10.1029/2018gl077092.
- D. P. Dee, S. M. Uppala, A. J. Simmons, P. Berrisford, P. Poli, S. Kobayashi, U. Andrae, M. A. Balmaseda, G. Balsamo, P. Bauer, P. Bechtold, A. C. M. Beljaars, L. van de Berg, J. Bidlot, N. Bormann, C. Delsol, R. Dragani, M. Fuentes, A. J. Geer, L. Haimberger, S. B. Healy, H. Hersbach, E. V. Hólm, L. Isaksen, P. Kållberg, M. Köhler, M. Matricardi, A. P. McNally, B. M. Monge-Sanz, J.-J. Morcrette, B.-K. Park, C. Peubey, P. de Rosnay, C. Tavolato, J.-N. Thépaut, and F. Vitart. The ERA-interim reanalysis: configuration and performance of the data assimilation system. *Quarterly Journal of the Royal Meteorological Society*, 137(656):553–597, 2011. doi: 10.1002/qj.828.
- G. Doms, J. Förstner, E. Heise, H.-J. Herzog, D. Mironov, M. Raschendorfer, T. Reinhardt, B. Ritter, R. Schrodin, J.-P. Schulz, and G. Vogel. COSMO-model version 6.00: A description of the nonhydrostatic regional COSMO-model - Part II: Physical parametrizations. 2021. doi: 10.5676/DWD_PUB/NWV/COSMO-DOC_6.00.II.
- A. D. Elvidge, I. A. Renfrew, J. C. King, A. Orr, T. A. Lachlan-Cope, M. Weeks, and S. L. Gray. Foehn jets over the Larsen C ice shelf, Antarctica. *Quarterly Journal of the Royal Meteorological Society*, 141(688):698–713, 2014. doi: 10.1002/qj.2382.
- R. Ezraty, F. Girard Arduin, J. Piollé, L. Kaleschke, and G. Heygster. Arctic and Antarctic sea ice concentration and Arctic sea ice drift estimated from SSIM. User's manual, version 2.1. Technical report, Available at Ifremer/CERSAT, Feb 2007. URL <ftp://ftp.ifremer.fr/ifremer/cersat/products/gridded/psi-drift/documentation/ssmi.pdf>.
- V. Favier, C. Agosta, S. Parouty, G. Durand, G. Delaygue, H. Gallée, A.-S. Drouet, A. Trouvilliez, and G. Krinner. An updated and quality controlled surface mass balance dataset for Antarctica. *The Cryosphere*, 7(2):583–597, 2013. doi: 10.5194/tc-7-583-2013.
- G. Fotso-Kamga, T. C. Fotso-Nguemo, I. Diallo, Z. D. Yepdo, W. M. Pokam, D. A. Vondou, and A. Lenouo. An evaluation of COSMO-CLM regional climate model in simulating precipitation over Central Africa. *International Journal of Climatology*, 40(5):2891–2912, apr 2020. doi: 10.1002/joc.6372.
- H. Gallée, S. Preunkert, S. Argentini, M. M. Frey, C. Genthon, B. Jourdain, I. Pietroni, G. Casasanta, H. Barral, E. Vignon, C. Amory, and M. Legrand. Characterization of the boundary layer at Dome C (East Antarctica) during the OPAL summer campaign. *Atmospheric Chemistry and Physics*, 15(11):6225–6236, 2015. doi: 10.5194/acp-15-6225-2015.
- E. Gilbert, A. Orr, J. C. King, I. A. Renfrew, T. Lachlan-Cope, P. F. Field, and I. A. Boutle. Summertime cloud phase strongly influences surface melting on the Larsen C ice shelf, Antarctica. *Quarterly Journal of the Royal Meteorological Society*, 146(729):1575–1589, 2020. doi: 10.1002/qj.3753.

- F. Giorgi. Thirty years of regional climate modeling: Where are we and where are we going next? *Journal of Geophysical Research: Atmospheres*, jun 2019. doi: 10.1029/2018jd030094.
- I. V. Gorodetskaya, M. Tsukernik, K. Claes, M. F. Ralph, W. D. Neff, and N. P. M. V. Lipzig. The role of atmospheric rivers in anomalous snow accumulation in East Antarctica. *Geophysical Research Letters*, 41(17):6199–6206, 2014. doi: 10.1002/2014gl060881.
- O. Gutjahr, G. Heinemann, A. Preußer, S. Willmes, and C. Drüe. Quantification of ice production in Laptev Sea polynyas and its sensitivity to thin-ice parameterizations in a regional climate model. *The Cryosphere*, 10(6):2999–3019, 2016. doi: 10.5194/tc-10-2999-2016.
- G. Heinemann, S. Willmes, L. Schefczyk, A. Makshtas, V. Kustov, and I. Makhotina. Observations and simulations of meteorological conditions over Arctic thick sea ice in late winter during the transarktika 2019 expedition. *Atmosphere*, 12(2):174, 2021. doi: 10.3390/atmos12020174.
- G. Heinemann, L. Schefczyk, S. Willmes, and M. D. Shupe. Evaluation of simulations of near-surface variables using the regional climate model CCLM for the MOSAiC winter period. *Elementa: Science of the Anthropocene*, 10(1), 2022. doi:10.1525/elementa.2022.00033.
- G. Heinemann, A. Preußer, R. Zentek, and I. M. Brooks. HALO wind lidar (level 1) data of the University of Trier for MOSAiC, 2023. PANGAEA.
- H. Hersbach, B. Bell, P. Berrisford, G. Biavati, A. Horányi, J. Muñoz Sabater, J. Nicolas, C. Peubey, R. Radu, I. Rozum, D. Schepers, A. Simmons, C. Soci, D. Dee, and J.-N. Thépaut. ERA5 monthly averaged data on single levels from 1979 to present. Copernicus Climate Change Service (C3S) Climate Data Store (CDS). (accessed on 28-02-2023), 2019.
- R. J. Hill, W. A. Brewer, and S. C. Tucker. Platform-motion correction of velocity measured by Doppler lidar. *Journal of Atmospheric and Oceanic Technology*, 25(8):1369–1382, 2008. doi: 10.1175/2007jtecha972.1.
- Y. Hu, K. Stamnes, M. Vaughan, J. Pelon, C. Weimer, D. Wu, M. Cisewski, W. Sun, P. Yang, B. Lin, A. Omar, D. Flittner, C. Hostetler, C. Trepte, D. Winker, G. Gibson, and M. Santa-Maria. Sea surface wind speed estimation from space-based lidar measurements. *Atmospheric Chemistry and Physics*, 8(13):3593–3601, 2008. doi: 10.5194/acp-8-3593-2008.
- C. Jablonowski, M. Herzog, J. Penner, R. Oehmke, Q. Stout, and B. van Leer. *Adaptive grids for weather and climate models*. PhD thesis, 2004.
- L. Jakobson, T. Vihma, E. Jakobson, T. Palo, A. Männik, and J. Jaagus. Low-level jet characteristics over the Arctic Ocean in spring and summer. *Atmospheric Chemistry and Physics*, 13(21):11089–11099, 2013. doi: 10.5194/acp-13-11089-2013.

- T. Jung, N. D. Gordon, P. Bauer, D. H. Bromwich, M. Chevallier, J. J. Day, J. Dawson, F. Doblas-Reyes, C. Fairall, H. F. Goessling, M. Holland, J. Inoue, T. Iversen, S. Klebe, P. Lemke, M. Losch, A. Makshtas, B. Mills, P. Nurmi, D. Perovich, P. Reid, I. A. Renfrew, G. Smith, G. Svensson, M. Tolstykh, and Q. Yang. Advancing polar prediction capabilities on daily to seasonal time scales. *Bulletin of the American Meteorological Society*, 97(9): 1631–1647, 2016. doi: 10.1175/bams-d-14-00246.1.
- J. H. Jungclaus, S. J. Lorenz, H. Schmidt, V. Brovkin, N. Brüggemann, F. Chegini, T. Crüger, P. De-Vrese, V. Gayler, M. A. Giorgetta, O. Gutjahr, H. Haak, S. Hagemann, M. Hanke, T. Ilyina, P. Korn, J. Kröger, L. Linardakis, C. Mehlmann, U. Mikolajewicz, W. A. Müller, J. E. M. S. Nabel, D. Notz, H. Pohlmann, D. A. Putrasahan, T. Raddatz, L. Ramme, R. Redler, C. H. Reick, T. Riddick, T. Sam, R. Schneck, R. Schnur, M. Schupfner, J.-S. Storch, F. Wachsmann, K.-H. Wieners, F. Ziemann, B. Stevens, J. Marotzke, and M. Claussen. The ICON earth system model version 1.0. *Journal of Advances in Modeling Earth Systems*, 14(4), 2022. doi: 10.1029/2021ms002813.
- C. Kittel, C. Amory, C. Agosta, N. C. Jourdain, S. Hofer, A. Delhasse, S. Doutreloup, P.-V. Huot, C. Lang, T. Fichet, and X. Fettweis. Diverging future surface mass balance between the Antarctic ice shelves and grounded ice sheet. *The Cryosphere*, 15(3):1215–1236, 2021. doi: 10.5194/tc-15-1215-2021.
- N. T. Kurtz and T. Markus. Satellite observations of Antarctic sea ice thickness and volume. *Journal of Geophysical Research: Oceans*, 117(C8):n/a–n/a, 2012. doi: 10.1029/2012jc008141.
- M. K. Laffin, C. S. Zender, M. van Wessem, and S. Marinsek. The role of föhn winds in eastern Antarctic Peninsula rapid ice shelf collapse. *The Cryosphere*, 16(4):1369–1381, 2022. doi: 10.5194/tc-16-1369-2022.
- M. A. Lazzara, G. A. Weidner, L. M. Keller, J. E. Thom, and J. J. Cassano. Antarctic automatic weather station program: 30 years of polar observation. *Bulletin of the American Meteorological Society*, 93(10):1519–1537, 2012. doi: 10.1175/bams-d-11-00015.1.
- F. Loewe. THE LAND OF STORMS. *Weather*, 27(3):110–121, 1972. doi: 10.1002/j.1477-8696.1972.tb04272.x.
- V. López-García, R. R. Neely, S. Dahlke, and I. M. Brooks. Low-level jets over the Arctic Ocean during MOSAiC. *Elementa: Science of the Anthropocene*, 10(1), 2022. doi: 10.1525/elementa.2022.00063.
- M. L. Maclennan, J. T. M. Lenaerts, C. Shields, and J. D. Wille. Contribution of atmospheric rivers to Antarctic precipitation. *Geophysical Research Letters*, 49(18), 2022. doi: 10.1029/2022gl100585.
- G. J. Marshall. Trends in the southern annular mode from observations and reanalyses. *Journal of Climate*, 16(24):4134–4143, 2003. doi: 10.1175/1520-0442(2003)016<4134:titsam>2.0.co;2.

- A. J. Monaghan, M. Barlage, J. Boehnert, C. L. Phillips, and O. V. Wilhelmi. Overlapping interests: The impact of geographic coordinate assumptions on limited-area atmospheric model simulations. *Monthly Weather Review*, 141(6):2120–2127, 2013. doi: 10.1175/mwr-d-12-00351.1.
- R. Mottram, N. Hansen, C. Kittel, J. M. van Wessem, C. Agosta, C. Amory, F. Boberg, W. J. van de Berg, X. Fettweis, A. Gossart, N. P. M. van Lipzig, E. van Meijgaard, A. Orr, T. Phillips, S. Webster, S. B. Simonsen, and N. Souverijns. What is the surface mass balance of Antarctica? An intercomparison of regional climate model estimates. *The Cryosphere*, 15(8):3751–3784, 2021. doi: 10.5194/tc-15-3751-2021.
- A. Orr, A. Kirchgaessner, J. King, T. Phillips, E. Gilbert, A. Elvidge, M. Weeks, A. Gadian, P. K. Munneke, M. Broeke, S. Webster, and D. McGrath. Comparison of kilometre and sub-kilometre scale simulations of a foehn wind event over the Larsen C ice shelf, Antarctic Peninsula using the met office unified model (MetUM). *Quarterly Journal of the Royal Meteorological Society*, 147(739):3472–3492, 2021. doi: 10.1002/qj.4138.
- C. L. Parkinson and D. J. Cavalieri. Antarctic sea ice variability and trends, 1979–2010. *The Cryosphere*, 6(4):871–880, 2012. doi: 10.5194/tc-6-871-2012.
- S. Paul, S. Willmes, and G. Heinemann. Long-term coastal-polynya dynamics in the southern Weddell Sea from MODIS thermal-infrared imagery. *The Cryosphere*, 9(6):2027–2041, 2015. doi: 10.5194/tc-9-2027-2015.
- C. Pelletier, T. Fichefet, H. Goosse, K. Haubner, S. Helsen, P.-V. Huot, C. Kittel, F. Klein, S. L. clec'h, N. P. M. van Lipzig, S. Marchi, F. Massonnet, P. Mathiot, E. Moravveji, E. Moreno-Chamarro, P. Ortega, F. Pattyn, N. Souverijns, G. V. Achter, S. V. Broucke, A. Vanhulle, D. Verfaillie, and L. Zipf. PARASO, a circum-antarctic fully coupled ice-sheet–ocean–sea-ice–atmosphere–land model involving f.ETISh1.7, NEMO3.6, LIM3.6, COSMO5.0 and CLM4.5. *Geoscientific Model Development*, 15(2):553–594, 2022. doi: 10.5194/gmd-15-553-2022.
- T. V. Pham, C. Steger, B. Rockel, K. Keuler, I. Kirchner, M. Mertens, D. Rieger, G. Zängl, and B. Früh. ICON in climate limited-area mode (ICON release version 2.6.1): a new regional climate model. *Geoscientific Model Development*, 14(2):985–1005, feb 2021. doi: 10.5194/gmd-14-985-2021.
- V. Platonov and M. Varentsov. Introducing a new detailed long-term COSMO-CLM hindcast for the Russian Arctic and the first results of its evaluation. *Atmosphere*, 12(3):350, mar 2021. doi: 10.3390/atmos12030350.
- E. Päsche, R. Leinweber, and V. Lehmann. An assessment of the performance of a 1.5 μm Doppler lidar for operational vertical wind profiling based on a 1-year trial. *Atmospheric Measurement Techniques*, 8(6):2251–2266, 2015. doi: 10.5194/amt-8-2251-2015.

- F. Reiser, S. Willmes, U. Hausmann, and G. Heinemann. Predominant sea ice fracture zones around Antarctica and their relation to bathymetric features. *Geophysical Research Letters*, 46(21):12117–12124, 2019. doi: 10.1029/2019gl084624.
- S. R. Rintoul, C. W. Hughes, and D. Olbers. Chapter 4.6 the antarctic circumpolar current system. In G. Siedler, J. Church, and J. Gould, editors, *Ocean Circulation and Climate*, volume 77 of *International Geophysics*, pages 271–XXXVI. Academic Press, 2001. doi: 10.1016/S0074-6142(01)80124-8.
- B. Rockel, A. Will, and A. Hense. The regional climate model COSMO-CLM (CCLM). *Meteorologische Zeitschrift*, 17(4):347–348, aug 2008. doi: 10.1127/0941-2948/2008/0309.
- A. Salcedo-Bosch, F. Rocadenbosch, and J. Sospedra. A robust adaptive unscented kalman filter for floating Doppler wind-LiDAR motion correction. *Remote Sensing*, 13(20):4167, 2021. doi: 10.3390/rs13204167.
- J. Schaffer, R. Timmermann, J. E. Arndt, S. S. Kristensen, C. Mayer, M. Morlighem, and D. Steinhage. A global, high-resolution data set of ice sheet topography, cavity geometry, and ocean bathymetry. *Earth System Science Data*, 8(2):543–557, oct 2016. doi: 10.5194/essd-8-543-2016.
- D. Schröder, G. Heinemann, and S. Willmes. The impact of a thermodynamic sea-ice module in the COSMO numerical weather prediction model on simulations for the Laptev Sea, Siberian Arctic. *Polar Research*, 30(1):6334, 2011. doi: 10.3402/polar.v30i0.6334.
- W. Schwerdtfeger. The effect of the Antarctic Peninsula on the temperature regime of the Weddell Sea. *Monthly Weather Review*, 103(1):45–51, 1975. doi: 10.1175/1520-0493(1975)103<0045:teotap>2.0.co;2.
- T. Semmler, S. Danilov, P. Gierz, H. F. Goessling, J. Hegewald, C. Hinrichs, N. Koldunov, N. Khosravi, L. Mu, T. Rackow, D. V. Sein, D. Sidorenko, Q. Wang, and T. Jung. Simulations for CMIP6 with the AWI climate model AWI-CM-1-1. *Journal of Advances in Modeling Earth Systems*, 12(9), 2020. doi: 10.1029/2019ms002009.
- M. D. Shupe, M. Rex, B. Blomquist, P. O. G. Persson, J. Schmale, T. Uttal, D. Althausen, H. Angot, S. Archer, L. Bariteau, I. Beck, J. Bilberry, S. Bucci, C. Buck, M. Boyer, Z. Brasseur, I. M. Brooks, R. Calmer, J. Cassano, V. Castro, D. Chu, D. Costa, C. J. Cox, J. Creamean, S. Crewell, S. Dahlke, E. Damm, G. de Boer, H. Deckelmann, K. Dethloff, M. Dütsch, K. Ebell, A. Ehrlich, J. Ellis, R. Engelmann, A. A. Fong, M. M. Frey, M. R. Gallagher, L. Ganzeveld, R. Gradinger, J. Graeser, V. Greenamyre, H. Griesche, S. Griffiths, J. Hamilton, G. Heinemann, D. Helmig, A. Herber, C. Heuzé, J. Hofer, T. Houchens, D. Howard, J. Inoue, H.-W. Jacobi, R. Jaiser, T. Jokinen, O. Jourdan, G. Jozef, W. King, A. Kirchgassner, M. Klingebiel, M. Krassovski, T. Krumpfen, A. Lampert, W. Landing, T. Laurila, D. Lawrence, M. Lonardi, B. Loose, C. Lüpkes, M. Maahn, A. Macke, W. Maslowski, C. Marsay, M. Maturilli, M. Mech, S. Morris, M. Moser, M. Nicolaus, P. Ortega, J. Osborn, F. Pätzold, D. K. Perovich, T. Petäjä, C. Pilz, R. Pirazzini, K. Posman,

- H. Powers, K. A. Pratt, A. Preußner, L. Quéléver, M. Radenz, B. Rabe, A. Rinke, T. Sachs, A. Schulz, H. Siebert, T. Silva, A. Solomon, A. Sommerfeld, G. Spreen, M. Stephens, A. Stohl, G. Svensson, J. Uin, J. Viegas, C. Voigt, P. von der Gathen, B. Wehner, J. M. Welker, M. Wendisch, M. Werner, Z. Xie, and F. Yue. Overview of the MO-SAiC expedition: Atmosphere. *Elementa: Science of the Anthropocene*, 10(1), 2022. doi: 10.1525/elementa.2021.00060.
- S. L. Sørland, R. Brogli, P. K. Pothapakula, E. Russo, J. V. de Walle, B. Ahrens, I. Anders, E. Bucchignani, E. L. Davin, M.-E. Demory, A. Dosio, H. Feldmann, B. Früh, B. Geyer, K. Keuler, D. Lee, D. Li, N. P. M. van Lipzig, S.-K. Min, H.-J. Panitz, B. Rockel, C. Schär, C. Steger, and W. Thiery. COSMO-CLM regional climate simulations in the coordinated regional climate downscaling experiment (CORDEX) framework: a review. *Geoscientific Model Development*, 14(8):5125–5154, aug 2021. doi: 10.5194/gmd-14-5125-2021.
- N. Souverijns, A. Gossart, M. Demuzere, J. T. M. Lenaerts, B. Medley, I. V. Gorodetskaya, S. V. Broucke, and N. P. M. van Lipzig. A new regional climate model for POLAR-CORDEX: Evaluation of a 30-year hindcast with COSMO-CLM2 over Antarctica. *Journal of Geophysical Research: Atmospheres*, 124(3):1405–1427, 2019. doi: 10.1029/2018jd028862.
- G. Spreen, L. Kaleschke, and G. Heygster. Sea ice remote sensing using AMSR-e 89-GHz channels. *Journal of Geophysical Research*, 113(C2), jan 2008. doi: 10.1029/2005jc003384.
- C. Steger and E. Bucchignani. Regional climate modelling with COSMO-CLM: History and perspectives. *Atmosphere*, 11(11):1250, nov 2020. doi: 10.3390/atmos11111250.
- L. Štulić, R. Timmermann, S. Paul, R. Zentek, G. Heinemann, and T. Kanzow. Southern Weddell Sea surface freshwater flux modulated by icescape and atmospheric forcing. *EGUsphere [preprint]*, 2023. doi: 10.5194/egusphere-2023-690.
- T. Tamura, K. I. Ohshima, and S. Nihashi. Mapping of sea ice production for Antarctic coastal polynyas. *Geophysical Research Letters*, 35(7):n/a–n/a, 2008. doi: 10.1029/2007gl032903.
- E.-M. Tastula, T. Vihma, and E. L. Andreas. Evaluation of polar WRF from modeling the atmospheric boundary layer over Antarctic sea ice in autumn and winter. *Monthly Weather Review*, 140(12):3919–3935, 2012. doi: 10.1175/mwr-d-12-00016.1.
- M. Tuononen, V. A. Sinclair, and T. Vihma. A climatology of low-level jets in the mid-latitudes and polar regions of the northern hemisphere. *Atmospheric Science Letters*, 16(4):492–499, 2015. doi: 10.1002/asl.587.
- M. van Dooren, D. Trabucchi, and M. Kühn. A methodology for the reconstruction of 2d horizontal wind fields of wind turbine wakes based on dual-Doppler lidar measurements. *Remote Sensing*, 8(10):809, 2016. doi: 10.3390/rs8100809.

- J. A. van Hooft, S. Popinet, C. C. van Heerwaarden, S. J. A. van der Linden, S. R. de Roode, and B. J. H. van de Wiel. Towards adaptive grids for atmospheric boundary-layer simulations. *Boundary-Layer Meteorology*, 167(3):421–443, 2018. doi: 10.1007/s10546-018-0335-9.
- N. P. M. van Lipzig, J. Turner, S. R. Colwell, and M. R. van Den Broeke. The near-surface wind field over the Antarctic continent. *International Journal of Climatology*, 24(15): 1973–1982, 2004. doi: 10.1002/joc.1090.
- J. M. van Wessem, W. J. van de Berg, B. P. Y. Noël, E. van Meijgaard, C. Amory, G. Birnbaum, C. L. Jakobs, K. Krüger, J. T. M. Lenaerts, S. Lhermitte, S. R. M. Ligtenberg, B. Medley, C. H. Reijmer, K. van Tricht, L. D. Trusel, L. H. van Ulf, B. Wouters, J. Wuite, and M. R. van den Broeke. Modelling the climate and surface mass balance of polar ice sheets using RACMO2 – part 2: Antarctica (1979–2016). *The Cryosphere*, 12(4):1479–1498, 2018. doi: 10.5194/tc-12-1479-2018.
- M. Vernet, W. Geibert, M. Hoppema, P. J. Brown, C. Haas, H. H. Hellmer, W. Jokat, L. Jullion, M. Mazloff, D. C. E. Bakker, J. A. Brearley, P. Croot, T. Hattermann, J. Hauck, C.-D. Hillenbrand, C. J. M. Hoppe, O. Huhn, B. P. Koch, O. J. Lechtenfeld, M. P. Meredith, A. C. N. Garabato, E.-M. Nöthig, I. Peeken, M. M. R. van der Loeff, S. Schmidtko, M. Schröder, V. H. Strass, S. Torres-Valdés, and A. Verdy. The Weddell Gyre, southern ocean: Present knowledge and future challenges. *Reviews of Geophysics*, 57(3):623–708, 2019. doi: 10.1029/2018rg000604.
- D. Walters, I. Boutle, M. Brooks, T. Melvin, R. Stratton, S. Vosper, H. Wells, K. Williams, N. Wood, T. Allen, A. Bushell, D. Copsey, P. Earnshaw, J. Edwards, M. Gross, S. Hardiman, C. Harris, J. Heming, N. Klingaman, R. Levine, J. Manners, G. Martin, S. Milton, M. Mittermaier, C. Morcrette, T. Riddick, M. Roberts, C. Sanchez, P. Selwood, A. Stirling, C. Smith, D. Suri, W. Tennant, P. L. Vidale, J. Wilkinson, M. Willett, S. Woolnough, and P. Xavier. The met office unified model global atmosphere 6.0/6.1 and JULES global land 6.0/6.1 configurations. *Geoscientific Model Development*, 10(4):1487–1520, 2017. doi: 10.5194/gmd-10-1487-2017.
- C. Weitkamp. *Lidar*. Springer-Verlag GmbH, 2006. ISBN 9780387251011. URL <https://www.ebook.de/de/product/24984089/lidar.html>.
- C. Wesche and W. Dierking. Iceberg signatures and detection in SAR images in two test regions of the Weddell Sea, Antarctica. *Journal of Glaciology*, 58(208):325–339, 2012. doi: 10.3189/2012jog11j020.
- B. Witschas, S. Rahm, A. Dörnbrack, J. Wagner, and M. Rapp. Airborne wind lidar measurements of vertical and horizontal winds for the investigation of orographically induced gravity waves. *Journal of Atmospheric and Oceanic Technology*, 34(6):1371–1386, 2017. doi: 10.1175/jtech-d-17-0021.1.
- B. Witschas, C. Lemmerz, A. Geiß, O. Lux, U. Marksteiner, S. Rahm, O. Reitebuch, and F. Weiler. First validation of Aeolus wind observations by airborne Doppler wind lidar

- measurements. *Atmospheric Measurement Techniques*, 13(5):2381–2396, 2020. doi: 10.5194/amt-13-2381-2020.
- A. P. Worby, C. A. Geiger, M. J. Paget, M. L. V. Woert, S. F. Ackley, and T. L. DeLiberty. Thickness distribution of Antarctic sea ice. *Journal of Geophysical Research*, 113(C5), 2008. doi: 10.1029/2007jc004254.
- Y. Yu and X.-M. Cai. Structure and dynamics of katabatic flow jumps: Idealised simulations. *Boundary-Layer Meteorology*, 118(3):527–555, 2006. doi: 10.1007/s10546-005-6433-5.
- G. Zängl, D. Reinert, P. Rípodas, and M. Baldauf. The ICON (ICOsahedral non-hydrostatic) modelling framework of DWD and MPI-m: Description of the non-hydrostatic dynamical core. *Quarterly Journal of the Royal Meteorological Society*, 141(687):563–579, 2014. doi: 10.1002/qj.2378.
- R. Zentek and G. Heinemann. Wind and backscatter profiles measured by a wind lidar during POLARSTERN cruise PS96 (ANT-XXXI/2 FROSN), 2019. URL <https://doi.org/10.1594/PANGAEA.902794>. PANGAEA.
- R. Zentek and G. Heinemann. Low-Level-Jet and Inversion statistics for Weddell Sea region of Antarctica, 2022. URL <https://doi.org/10.1594/PANGAEA.940364>. PANGAEA.
- R. Zentek and G. Heinemann. Weddell Sea Projekt - Uni Trier - All Simulation - Monthly Mean, 2022a. URL https://www.wdc-climate.de/ui/entry?acronym=DKRZ_LTA_958_ds00005. DOKU at DKRZ.
- R. Zentek and G. Heinemann. Weddell Sea Projekt - Uni Trier - Simulation C05, 2022b. URL https://www.wdc-climate.de/ui/entry?acronym=DKRZ_LTA_958_ds00003. DOKU at DKRZ.
- R. Zentek and G. Heinemann. Weddell Sea Projekt - Uni Trier - Simulation T15, 2022c. URL https://www.wdc-climate.de/ui/entry?acronym=DKRZ_LTA_958_ds00002. DOKU at DKRZ.
- R. Zentek and G. Heinemann. Weddell Sea Projekt - Uni Trier - Simulation C15, 2022d. URL https://www.wdc-climate.de/ui/entry?acronym=DKRZ_LTA_958_ds00001. DOKU at DKRZ.
- R. Zentek and G. Heinemann. Weddell Sea Projekt - Uni Trier - Low Level Jet Data, 2022e. URL https://www.wdc-climate.de/ui/entry?acronym=DKRZ_LTA_958_ds00006. DOKU at DKRZ.
- R. Zentek, S. H. E. Kohnemann, and G. Heinemann. Wind and backscatter profiles measured by a wind lidar during POLARSTERN cruise PS85 (ark-xxviii/2), 2019a. URL 10.1594/PANGAEA.902790. PANGAEA.

- R. Zetek, S. H. E. Kohnemann, and G. Heinemann. Wind and backscatter profiles measured by a wind lidar during POLARSTERN cruise PS106/1 (ark-xxxi/1.1), 2019b. URL 10.1594/PANGAEA.902799. PANGAEA.
- R. Zetek, S. H. E. Kohnemann, and G. Heinemann. Wind and backscatter profiles measured by a wind lidar during POLARSTERN cruise PS106/2 (ark-xxxi/1.2), 2019c. URL 10.1594/PANGAEA.902804. PANGAEA.
- R. Zetek, A. Preußer, and G. Heinemann. Wind and backscatter profiles measured by a wind lidar during POLARSTERN cruise PS109 (ark-xxxi/4), 2019d. URL 10.1594/PANGAEA.902805. PANGAEA.
- R. Zetek, F. Reiser, F. Schnaase, and G. Heinemann. Wind and backscatter profiles measured by a wind lidar during POLARSTERN cruise PS111 (ant-xxxiii/2, frost), 2019e. URL 10.1594/PANGAEA.902806. PANGAEA.

Curriculum Vitae

Rolf Zentek, M.Sc.

ORCID: <https://orcid.org/0000-0003-3249-8635>

Email: zentek@uni-trier.de

Education

1997 – 2006	Abitur, Gymnasium Beverungen
2007 – 2011	Bachelor (applied mathematics), University of Trier
2011 – 2014	Master (applied mathematics), University of Trier
2014 - now	Ph.D. Candidate, University of Trier research assistant in the projects Transdrift, Weddell Ice, REDOCCA and MISLAM

Internships

2010	Department ocean dynamics, Alfred-Wegener-Institut, Bremerhaven
2011	Department research and development, Deutscher Wetterdienst, Offenbach

Field campaign

2015 - 2016	Participation on the Antarctic expedition PS96 of the RV Polarstern
-------------	---

Publications (peer reviewed)

Zentek, R.; Heinemann, G. and Sachs, E.: Climatology of Wind, Kinetic Energy, and Temperature Spectra Using a High-Resolution Climate Model for Mid-Europe, *J. Climate*, 29, 963–974, <https://doi.org/10.1175/JCLI-D-15-0540.1>, 2016

Zentek, R.; Kohnemann, S. H. E. and Heinemann, G.: Analysis of the performance of a ship-borne scanning wind lidar in the Arctic and Antarctic, *Atmos. Meas. Tech.*, 11, 5781–5795, <https://doi.org/10.5194/amt-11-5781-2018>, 2018.

Zentek, R. and Heinemann, G.: Verification of the regional atmospheric model CCLM v5.0 with conventional data and lidar measurements in Antarctica, *Geosci. Model Dev.*, 13, 1809–1825, <https://doi.org/10.5194/gmd-13-1809-2020>, 2020.

Heinemann, G.; **Zentek**, R. A Model-Based Climatology of Low-Level Jets in the Weddell Sea Region of the Antarctic, *Atmosphere*, 12, 1635. <https://doi.org/10.3390/atmos12121635>, 2021.

Posters and Talks

Heinemann, G., Jung, T., Timmermann, R., Stulic, L., **Zentek**, R.: Quantification of sea ice production in the southern Weddell Sea using a synergy of numerical simulations and remote sensing data, DFG SPP Antarktischforschung Workshop, Frankfurt, 2015.

Heinemann, G., Jung, T., Timmermann, R., Stulic, L., **Zentek**, R.: Quantification of sea ice production in the southern Weddell Sea using a synergy of numerical simulations and remote sensing data (2nd year), DFG SPP Antarktischforschung Workshop, Rostock, 2016.

Zentek, R., Heinemann, G.: Verification of simulations in the Weddell Sea region in Antarctica, COSMO / CLM / ICON / ART - User Seminar, Offenbach, 2017.

Stulic, L., Timmermann, R., **Zentek**, R., Heinemann, G.: Quantification of sea ice production at coastal polynyas in the southern Weddell Sea, European Geosciences Union (EGU), General Assembly, Vienna, 2017.

Zentek, R., Heinemann, G., Paul, S., Stulic, L. Timmermann, R.: Quantification of sea ice production in Weddell Sea polynyas, European Geosciences Union (EGU), General Assembly, Vienna, 2017.

Zentek, R., Heinemann, G., Kohnemann, S.: Ship-borne wind LIDAR measurements in the Arctic and Antarctic, European Geosciences Union (EGU), General Assembly, Vienna, 2017.

Heinemann, G., Jung, T., Timmermann, R., Stulic, L., **Zentek**, R., Paul, S., Preusser, A.: Quantification of sea ice production in the southern Weddell Sea using a synergy of numerical simulations and remote sensing data (3rd year), DFG SPP Antarktischforschung Workshop, Erlangen, 2017.

Zentek, R. and Heinemann, G.: Verification of the regional atmospheric model CCLM with measurements in the Antarctic, 27. Internationale Polartagung, Rostock, 2018.

Heinemann, G.; Semmler, T.; Timmermann, R.; Kolatschek, V. and **Zentek**, R.: RE-DOCCA – Regional high-resolution Downscaling of Climate Change in the Antarctic, DFG

SPP Antarktisforschung Workshop, online, 2020.

Heinemann, G.; Semmler, T.; Timmermann, R.; Teske, V. and **Zentek**, R.: REDOCCA – Regional high-resolution Downscaling of Climate Change in the Antarctic, DFG SPP Antarktisforschung Workshop, online, 2021.

Heinemann, G.; Semmler, T.; Timmermann, R.; Teske, V. and **Zentek**, R.: REDOCCA – Regional high-resolution Downscaling of Climate Change in the Antarctic, DFG SPP Antarktisforschung Workshop, Bielefeld, 2022.

Zentek, R. and Heinemann, G.: Climatology of Antarctic Low-Level Jets, 28. Internationale Polartagung, Potsdam, 2022.

Zentek, R. and Heinemann, G.: Climatology of Antarctic Low-Level Jets, AntClimNow Workshop, Cambridge, 2022.

Data publication

Zentek, R.; Kohnemann, S.H.E.; Heinemann, G.: Wind and backscatter profiles measured by a wind lidar during POLARSTERN cruise PS85, PANGAEA, <https://doi.org/10.1594/PANGAEA.902790>, 2019.

Zentek, R.; Heinemann, G.: Wind and backscatter profiles measured by a wind lidar during POLARSTERN cruise PS96, PANGAEA, <https://doi.org/10.1594/PANGAEA.902794>, 2019.

Zentek, R.; Kohnemann, S.H.E.; Heinemann, G.: Wind and backscatter profiles measured by a wind lidar during POLARSTERN cruise PS106.1, PANGAEA, <https://doi.org/10.1594/PANGAEA.902799>, 2019.

Zentek, R.; Kohnemann, S.H.E.; Heinemann, G.: Wind and backscatter profiles measured by a wind lidar during POLARSTERN cruise PS106.2, PANGAEA, <https://doi.org/10.1594/PANGAEA.902804>, 2019.

Zentek, R.; Preußer, A.; Heinemann, G.: Wind and backscatter profiles measured by a wind lidar during POLARSTERN cruise PS109, PANGAEA, <https://doi.org/10.1594/PANGAEA.902805>, 2019.

Zentek, R.; Reiser, F.; Schnaase, F.; Heinemann, G.: Wind and backscatter profiles measured by a wind lidar during POLARSTERN cruise PS111, PANGAEA, <https://doi.org/10.1594/PANGAEA.902806>, 2019.

Zentek, R. and Heinemann, G.: Low-Level-Jet and Inversion statistics for Weddell Sea region of Antarctica. PANGAEA, <https://doi.org/10.1594/PANGAEA.940364>, 2022.

Zentek, R.; Heinemann, G.: Weddell Sea Projekt - Uni Trier - Low Level Jet Data. DOKU at DKRZ. https://www.wdc-climate.de/ui/entry?acronym=DKRZ_LTA_958_ds00006, 2022.

Zentek, R.; Heinemann, G.: Weddell Sea Projekt - Uni Trier - All Simulation - Monthly Mean. DOKU at DKRZ. https://www.wdc-climate.de/ui/entry?acronym=DKRZ_LTA_958_ds00005, 2022.

Zentek, R.; Heinemann, G.: REDOCCA Projekt - Uni Trier - All Simulation - Monthly Mean. DOKU at DKRZ. https://www.wdc-climate.de/ui/entry?acronym=DKRZ_LTA_958_ds00004, 2022.

Zentek, R.; Heinemann, G.: Weddell Sea Projekt - Uni Trier - Simulation C05. DOKU at DKRZ. https://www.wdc-climate.de/ui/entry?acronym=DKRZ_LTA_958_ds00003, 2022.

Zentek, R.; Heinemann, G.: Weddell Sea Projekt - Uni Trier - Simulation T15. DOKU at DKRZ. https://www.wdc-climate.de/ui/entry?acronym=DKRZ_LTA_958_ds00002, 2022.

Zentek, R.; Heinemann, G.: Weddell Sea Projekt - Uni Trier - Simulation C15. DOKU at DKRZ. https://www.wdc-climate.de/ui/entry?acronym=DKRZ_LTA_958_ds00001, 2022.

Heinemann, G., Preußer, A., **Zentek**, R.; Brooks, I. M.: HALO wind lidar (level 1) data of the University of Trier for MOSAiC. PANGAEA, <https://doi.org/10.1594/PANGAEA.954826>, 2023.